HYDROTHERMAL SYNTHESIS OF TiO_2/ZnO/RGO NANO-COMPOSITE PHOTOCATALYSTS: ENHANCING PHOTOCATALYTIC ACTIVITIES FOR CONTAMINANT DEGRADATION

PHOUTTHIDETH PHOUHEUANGHONG

A THESIS SUBMITTED IN PARTIAL FULFILLMENT OF THE REQUIREMENT FOR THE DEGREE OF MASTER OF ENGINEERING

PROGRAM IN CIVIL ENGINEERING

FACULTY OF ENGINEERING

RAJAMANGALA UNIVERSITY OF TECHNOLOGY THANYABURI

ACADEMIC YEAR 2024

HYDROTHERMAL SYNTHESIS OF TiO2/ZnO/RGO NANO-COMPOSITE PHOTOCATALYSTS: ENHANCING PHOTOCATALYTIC ACTIVITIES FOR CONTAMINANT DEGRADATION

PHOUTTHIDETH PHOUHEUANGHONG

2024

วิทยานิพนธ์ฉบับนี้เป็นงานวิจัยที่เกิดจากการค้นคว้าและวิจัย ขณะที่ข้าพเจ้าศึกษาอยู่ในคณะวิศวกรรมศาสตร์ มหาวิทยาลัยเทคโนโลยีราชมงคลธัญบุรี ดังนั้นงานวิจัยในวิทยานิพนธ์ฉบับนี้ถือเป็นลิขสิทธิ์ของมหาวิทยาลัยเทคโนโลยีราชมงคลธัญบุรี และข้อความต่างๆในวิทยานิพนธ์ฉบับนี้ ข้าพเจ้าขอรับรองว่าไม่มีการคัดลอกหรือนำงานวิจัยของผู้อื่นมานำเสนอในชื่อของข้าพเจ้า

This thesis consists of research materials conducted at the Faculty of Engineering, Rajamangala University of Technology Thanyaburi and hence the copyright owner. I hereby certify that the thesis does not contain any forms of plagiarism.

.....

Phoutthideth Phouheuanghong

Thesis Title	Hydrothermal Synthesis of TiO_2/ZnO/RGO Nano-composite Photocatalysts: Enhancing Photocatalytic Activities for Contaminant Degradation
Name - Surname	Mr. Phoutthideth Phouheuanghong
Program	Civil Engineering
Thesis Advisor	Associate Professor Thammasak Rojviroon, D.Eng.
Academic Year	2024

THESIS COMMITTEE

..... Chairman
(Associate Professor Orawan Rojviroon, D.Eng.)

..... Committee
(Professor Sanya Sirivithayapakorn, Ph.D.)

..... Committee
(Assistant Professor Kullaya Saricheewin, D.Eng.)

..... Committee
(Associate Professor Thammasak Rojviroon, D.Eng.)

Approved by the Faculty of Engineering, Rajamangala University of Technology Thanyaburi in Partial Fulfillment of the Requirements for the Degree of Master of Engineering

..... Dean of Faculty of Engineering
(Associate Professor Sorapong Pavasupree, Ph.D.)
19 May 2025

Thesis Title	Hydrothermal Synthesis of TiO_2/ZnO/RGO Nano-composite Photocatalysts: Enhancing Photocatalytic Activities for Contaminant Degradation
Name - Surname	Mr. Phoutthideth Phouheuanghong
Program	Civil Engineering
Thesis Advisor	Associate Professor Thammasak Rojviroon, D. Eng.
Academic Year	2024

ABSTRACT

This study focuses on the synthesis and application of a TiO_2/ZnO/RGO (TZR) nanocomposite integrated with micro-nano bubble (MNB) technology for the effective degradation of indigo carmine (IC), reactive black 5 (RB5) dyes, and carbaryl pesticides. The combination of advanced nanomaterials with MNB aims to enhance photocatalytic efficiency, addressing limitations in conventional wastewater treatment methods.

The TZR nanocomposite was synthesized using a simple and cost-effective hydrothermal method, ensuring a well-dispersed structure with improved photocatalytic properties. Comprehensive structural, morphological, and optical characterizations, including XRD, XPS, FTIR, SEM-EDS, HR-TEM, BET, PL, and UV-DRS analyses, confirmed the successful formation of the composite with a heterogeneous distribution of its components. The photocatalytic performance of TZR was evaluated under visible light irradiation, and its efficiency was compared to other composite variations, including TZ, TR, and ZR. Additionally, the integration of MNB technology was employed to enhance the dispersion of the nanocomposite and improve oxygen transfer, facilitating more effective interaction between the photocatalyst and pollutants.

The results demonstrated that TZR achieved degradation efficiencies of 98.30%, 97.83%, and 97.17% for IC, RB5, and carbaryl, respectively, within 120 minutes. The synergistic effect of TiO_2, ZnO, and RGO contributed to enhanced electron-hole separation, increased surface area, and broader light absorption. Incorporating MNB technology significantly boosted degradation efficiency, achieving 99.08%, 98.73%, and 98.98% for IC, RB5, and carbaryl, respectively, in the same duration. These findings highlight the potential of combining advanced nanocomposite photocatalysts with MNB technology for sustainable and highly efficient wastewater treatment applications.

Keywords: nanocomposite, micro-nanobubbles, electron-hole separation, wastewater

Acknowledgments

The successful completion of this research study was made possible through the generosity and support of Assoc. Prof. Dr. Thammasak Rojviroon, Assoc. Prof. Dr. Orawan Rojviroon, Asst. Dr. Ranjith Rajenden, Dr. Rattana Muangmora, Miss Nicharee Akechatree, Miss Yuwadee Leelert, and Miss Kanjana Loytala. Their invaluable knowledge, guidance, and insightful suggestions greatly contributed to refining this work. The researcher sincerely appreciates their dedication and kindness in generously offering their time and effort, for which profound gratitude is extended.

The researcher would also like to extend their sincere gratitude and dedicate all the merit and benefits of this research to their parents and friends, who have provided unwavering support and encouragement throughout the research process. Furthermore, the successful completion of this research is largely due to the assistance and provision of analytical tools and equipment by the staff of the Department of Civil Engineering, Faculty of Engineering, Rajamangala University of Technology Thanyaburi, as well as all the faculty members who provided knowledge and guidance. Thank you for your contributions.

Lastly, the researcher earnestly anticipates that this investigation will be advantageous to those who are intrigued. The researcher sincerely apologizes for any shortcomings or imperfections in this research.

Phoutthideth Phouheuanghong

Table of Contents

Table of Contents (Continued)

List of Tables

List of Tables (Continued)

List of Tables (Continued)

List of Tables (Continued)

List of Tables (Continued)

List of Figures

List of Figures (Continued)

Page

List of Figures (Continued)

Page

List of Abbreviations of Thesis

TiO_2	Titanium dioxide
ZnO	Zinc
RGO	Reduced graphene oxide
MNB	Micro-nanobubbles
TZR	Titanium dioxide/Zinc/Reduced graphene oxide
ZR	Zinc/Reduced graphene oxide
TR	Titanium dioxide/Reduced graphene oxide
TZ	Titanium dioxide/Zinc
eV	Electric Vehicles
IC	Indigo Carmine
RB5	Reactive Black 5
CB	Conduction band
VB	Valence band
$\bullet O_2^-$	Superoxide radicals
•OH	Hydroxyl radicals
ROS	Reactive oxygen species
e^-	Electron
h^+	hole
C_0	The initial concentration of the reactant (mg. L^{-1})
C	The concentration of the reactant at time t
k	Pseudo-first-order kinetics the rate constant (min^{-1})
t	the time

CHAPTER 1
INTRODUCTION

1.1 Background and Statement of the Problem

In recent years, water pollution has emerged as a significant global problem. Wastewater contains a range of organic pollutants, including dyes and pesticides, which can potentially harm ecosystems and human health [1, 2]. Conventional methods for treating wastewater frequently face challenges in efficiently eliminating these pollutants, which can potentially endanger public health and the environment [1, 2]. Addressing these challenges requires the development of new and sustainable technologies for wastewater treatment; advanced technologies, such as nanomaterials for pollutant removal, enzymes for tackling resistant pollutants, and sustainable interventions, are critical in developing wastewater treatment processes that effectively combat water pollution [3, 4].

Traditional treatment methods for such contaminants often have limitations, such as high energy consumption, incomplete mineralization, and the formation of harmful by-products [5, 6]. The photocatalytic process has emerged as a promising green technology for degrading organic and inorganic pollutants in wastewater. This process uses light to activate photocatalysts, such as metal oxides like titanium dioxide (TiO_2) and zinc oxide (ZnO), which generate reactive oxygen species (ROS) that can effectively degrade organic pollutants [7, 8]. Among various photocatalysts, TiO_2 is favored due to its high photoactivity, chemical stability, and environmental safety; however, its wide band gap restricts light absorption primarily to the ultraviolet region, limiting its efficiency under solar illumination [9, 10], Additionally, the rapid recombination of electron-hole pairs on TiO_2 surfaces further diminishes its photocatalytic effectiveness [11, 12].

Researchers have explored various strategies to enhance the photocatalytic activity of materials such as TiO_2 and ZnO, including doping and incorporating reduced graphene oxide (RGO). The unique properties of RGO, including its high electrical conductivity and large surface area, facilitate the separation of electron-hole pairs when combined with these semiconductors, thereby improving photocatalytic efficiency unique properties such as high electrical conductivity [13, 14], a large surface area, and excellent light absorption across the solar spectrum. They can accept electrons when mixed with

TiO_2, ZnO, and RGO, which makes it easier for electron-hole pairs to separate and boosts the photocatalytic activity of the mixture [14, 15].

This research aims to photocatalyst nanocomposites using TiO_2, ZnO, and reduced graphene oxide (RGO), specifically the TiO_2/ZnO/RGO (TZR) blend, through a hydrothermal method, to enhance photocatalytic efficiency for pollutant degradation in synthetic wastewater. Photocatalysis has been recognized as a promising technology for wastewater treatment, particularly for degrading organic pollutants like dyes and pesticides under UVA irradiation, which can be further enhanced by the incorporation of micro-nanobubbles (MNB) [16, 17], the addition of MNB improves the photocatalytic process by facilitating better mass transfer and increasing the effective surface area for reactions, thus enhancing pollutant degradation rates [16, 17]. This study investigated the photocatalytic process's kinetics and mechanism for removing this synthetic wastewater.

1.2 Purpose of the study

1.2.1 To prepare and study the physical properties of the TZR photocatalyst.

1.2.2 To evaluate the degradation efficiency of the photocatalytic process in two different synthetic wastewaters with dyes and pesticides in wastewater through the photocatalytic process under UVA light source and MNB aeration.

1.2.3 To investigate the kinetics of the photocatalytic degradation process in two different synthetic wastewaters with dyes and pesticides in wastewater.

1.3 Scope

1.3.1 Synthesis of photocatalyst: TZR nanocomposites will be synthesized hydrothermal. The starting materials will be titanium dioxide, zinc oxide, and reduced graphene oxide. The molar ratio of TiO_2, ZnO, and RGO will be varied to investigate its effect on the properties of the nanocomposites.

1.3.2 Characterization: the structural, morphological, and optical properties of the nanocomposites will be characterized using various techniques, including band-gap, x-ray diffraction (XRD), Fourier Transform Infrared Spectrometer (FT-IR), spectroscopy (XPS), scanning electron microscopy (SEM), transmission electron microscopy (TEM), Brunauer-Emmett-Teller (BET), Photoluminescence (PL), and diffuse reflectance spectroscopy (UV-Vis).

1.3.3 Three types of synthetic wastewater are prepared from indigo carmine (IC), Reactive Black (RB5) dye, and carbaryl pesticide, respectively.

1.3.4 The batch reactor was exposed to UVA light generated by four 300 W bulbs, resulting in an average light intensity of 1,250 $\mu W.cm^{-2}$ and micro-nanobubble aeration in the photocatalytic process.

1.3.5 Employ molecular structure analysis to examine the degradation of the dye's molecular structure using the Gas Chromatography-Mass Spectrometry (GC-MS) apparatus.

1.4 Expected Benefits

1.4.1 Obtain photocatalysts with advantageous characteristics that support efficient photocatalytic reactions.

1.4.2 Collect data about the photocatalytic process's mechanism and efficiency for degrading dyes and pesticides in combination with UVA irradiation and adding micro/nanobubbles (MNB) in the wastewater.

CHAPTER 2
REVIEW AND LITERATURE

2.1 Pesticides

Pesticides are crucial in modern agriculture as they protect crops from pests and diseases, enhance yields, and ensure food security. However, their environmental persistence poses significant risks, including soil and water contamination and adverse effects on non-target organisms [18]. The degradation pathways of pesticides are complex, necessitating a clear distinction between degradative and non-degradative processes to mitigate their environmental impact. Consequently, emphasizing the responsible utilization of pesticides is vital to reducing adverse effects on animal health and ecosystems. Although indispensable in modern agriculture, careful consideration and monitoring of pesticide management and environmental impacts are imperative [19].

2.1.1 Types of Pesticides

Pesticides are classified into various categories, including insecticides, herbicides, fungicides, and acaricides, each serving specific agricultural purposes such as pest elimination and crop protection; the extensive application of synthetic pesticides has significantly enhanced agrarian productivity; however, it has also led to the emergence of resistance among pest populations, complicating pest management strategies [20, 21]. Moreover, the environmental impact of pesticide use is substantial, as these chemicals can contaminate water sources and harm non-target organisms, raising concerns about ecological sustainability, as shown in Table 2.1.

Table 2.1 Pesticide Classification and Impact.

Feature	Information
Impact	• Extends beyond target organisms, affecting non-target organisms and the environment, including aquatic ecosystems and human health
Toxicity	• Studies investigate acute lethal effects and potential risks to human health
Classification	• It is crucial for understanding the impact on human health and the environment
Types by Target Location	
• Inside plant cells • Outside plant cells (contact/non-systemic) • Systemic pesticides	
Types by Targeted Pest	
• Insecticides (kill insects) • Herbicides (kill weeds) • Fungicides (kill fungus) • Acaricides (kill mites)	

The many types of pesticides, including herbicides, insecticides, fungicides, and acaricides, target specific pests and plant diseases. Efficient pesticide management and environmental protection must comprehend their mechanisms of action and possible effects on non-target creatures and human health.

2.1.2 Insecticides

One kind of pesticide made expressly to destroy insects is called an insecticide. They are employed in many contexts, including households, public health, and agriculture. They are available in various forms, including liquids, sprays, dusts, and baits [22, 23]. Chemical insecticides come in a wide variety, each with a special mechanism of action [24, 25]. Typical varieties include some of the following in Table 2.2

Table 2.2 These insecticides can be divided into three group

Group	Target organisms	Mechanism of action	Symptoms of exposure
Organochlorines	Broad-spectrum insects, birds, fish	Disrupts the nervous system by interfering with sodium channels	Tremors, convulsions, nausea, vomiting
Organophosphates	Insects, but also beneficial insects to a lesser extent	Inhibits cholinesterase enzyme, leading to nerve overstimulation	Similar to organochlorines, but often shorter duration
Carbamates		It inhibits cholinesterase enzyme but is less potent than organophosphates	Similar to organochlorines, but often shorter duration

- **Carbamates**

Insecticides containing carbamates are frequently used in gardens, houses, and farming. Typical carbamate examples are carbofuran, carbaryl, and aldicarb. They inhibit cholinesterase enzymes and, therefore, share similar exposure symptoms, although carbamate poisonings tend to be of shorter duration. Carbamate exposure can be assessed by measuring cholinesterase levels in the blood, similar to organophosphate exposure. Carbamates are divided into three main groups, detailed in Table 2.3.

Table 2.3 Classification of Carbamates

Group	Name	Level of toxicity
Aryl N-methyl carbamate	Carbaryl and Propoxur	Moderately
Methyl Carbamates	Carbofuran	Extremely
Carbamylated Oximes	Methomyl	Extremely
Thiocarbamate	Cartap hydrochloride	Highly

2.1.3 Carbaryl

Carbaryl belongs to the family of carbamate pesticides, which are beneficial compounds that may be used to manage and eliminate pests obstructing plant

growth. It eliminates over a hundred kinds of pests and insects, including ladybugs, leaf-eating insects, and whiteflies. Carbaryl also aids in raising the yield to the required quality level [26]. As shown in Figure 2.1.

In agriculture, pest insects and other arthropods are controlled with a carbamate pesticide. It also regulates plant growth. The primary applications include protecting crops (fruit trees, vegetables, olives, cotton, rice, forestry, etc.) [26], Thinning apples, protecting poultry from lice, mites, fleas, and ticks, protecting domestic and farm animals from lice, fleas, ticks, and horn flies, and performing various other pest control tasks (such as cockroaches, mosquitoes, grasshoppers, and lawn care).

- **Identification of Physical and Chemical Properties Analysis**

  ISO Common names: Carbartl (E-ISO,(m)F-ISO, ANSI, BAN, BSL, ESA, and JMAF)

  Common trade names: Arilat, Arilate, Arylam, Atoxan, Bercema, Caprolin, Carbacine, Carbatox, Carbavur, Carbomate, Carpalia, Denapon, Dicarham, Dyna-carhyl, Karharyl, Karhatox, Karhosep, Menaphtam, Monsur, Mugan, Murvin, Oltitox, Panarn, Pomex, Prosevor, Ravyon, Seffein, Sevimol, and Sevin, Vioxan, (Sevin is the most widely used trade name).

  Synonyms: None

  Chemical names: IUPAC 1-naphthyl methylcarbamate

  CA 1-naphthaleyl-methylcarbamate

  Structural formula:

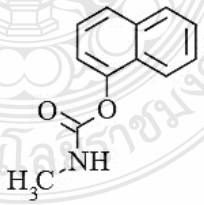

Figure 2.1 Structure of carbaryl

Table 2.4: Molecular structure of carbaryl

Specific features	Details
Type	Insecticides: Carbamate group
Chemical Group	1-Naphthyl, N-methyl carbamate
Chemical Formula	$C_{12}H_{11}NO_2$
Melting point (°C)	142
Boiling point (°C)	decomposing
Solubility in water (30°C)	40 mg/L^{-1}
Specific density (20°C)	1.23
Relative vapor density	None
Vapor pressure	1.2×10.0-3.1×10.0 mm. Hg @ 24-25 °C
Flash point	193 °C
Octanol/water partition coefficient (Log K_{ow})	1.59-2.3
Flammability limits	None
Relative molecular mass	201
Condition	White powder
Smell	None
Density	130 g/L
Surface area	The average particle size is 20 nm.
Molecular Weight	201.2 g
Exposure Routes	Skin, food, respiration
Environmental Impact	Damages soil, water, eco-systems, and food chains

Table 2.5 summarizes key points regarding the revised "List of Hazardous Substances (No. 6) B.E. 2020" issued by the Ministry of Industry in Thailand [27]. The identification of occupational carcinogens (OCs) from this list involved a systematic approach, utilizing criteria that classify agents based on their carcinogenicity and quantifying import/export data to prioritize substances for regulation [27].

Table 2.4 Regulatory update and considerations for carbaryl use.

Policy Change	Including chlorpyrifos-methyl and paraquat derivatives on the banned list necessitates the transition to alternative pest control solutions with lower toxicity and environmental impact.
Focus on Carbaryl	Carbaryl remains a permitted broad-spectrum insecticide. However, its utilization necessitates cautious evaluation due to: Persistence and environmental concerns: Low water solubility and heat/light stability contribute to the potential for ecological persistence and non-target species exposure.
	Toxicity and health risks: neurological impacts on insects translate to potential harm to other organisms if exposure pathways exist.
Recommendations	Integrated pest management (IPM) strategies: emphasize non-chemical control methods and prioritize safer alternatives to minimize reliance on carbaryl.
	Adhere to strict application guidelines: Implement safety protocols and follow expert recommendations to minimize environmental and human health risks associated with carbaryl use
	Research and development of safer solutions: foster continued research and development efforts to discover more sustainable and environmentally friendly pest control solutions with reduced toxicity profiles.

Although secondary sources can be found throughout the world, the majority of technical products are produced in the USA, created with less than 0.05% of the 2-naphthyl carbamate isomer (also known as "Beta-carbaryl") and a minimum purity of 99% w/w carbaryl. FAO requires a minimum of 98% w/w carbaryl with a 2-naphthyl carbamate isomer concentration of less than 0.05% w/w. Details of toxicology information on carbaryl are shown in Table 2.6.

Table 2.5 Toxicology information on carbaryl

Property characteristics	Details
Half-life	21 days in the water
LD_{50} in laboratory animals (rats)	250-850 mg/kg
LD_{50} in humans	250 mg
TLV from breathing	5 $mg.m^{-3}$

Note:

- The response threshold that results in half of the population dying is known as the 50% lethal dose (LD_{50}).
- The concentration of contaminants in the air that employees may safely be exposed to during working hours is known as the Threshold Limit Value (TLV) (8 hours).

2.2 Dye

The dyeing industry is experiencing significant growth, projected to reach USD 37 billion by 2023, with an annual growth rate of 5.46% [28, 29], However, this expansion raises environmental concerns due to the discharge of approximately 1,000 tons of non-biodegradable synthetic dyes into water bodies annually [28, 29], the prevalent use of hydrocarbons like naphthalene and benzene in dye production contributes to the environmental burden, as these compounds are often resistant to biodegradation.

The dyeing process employs various chemicals, categorized into auxiliary dyes, basic chemicals, and finishing agents, each playing a crucial role in achieving the desired color and properties. The environmental impact of these processes necessitates the development of sustainable alternatives, such as natural dyes, which are biodegradable and less toxic.

2.2.1 Types of dye

The classification of dyes in the industrial sector is primarily based on their intended application, encompassing eleven distinct types: acid, basic, direct, dispersion, reactive, azoic, vat, solvent, food, hair, and sulfur dyes [30], as shown in Table 2.8. Each type of dye exhibits distinct properties, application techniques, and chemical structures, which are crucial for their effectiveness in the dyeing process [30]. The chromophore type within the dye molecule plays a significant role in determining these characteristics, influencing factors such as colorfastness and affinity for substrates [31]. As shown in Table 2.7.

Table 2.6 Chromophore type of dyes.

Class	Chromophore	Example
Azo dye		Methyl Orange, Congo Red, Sudan dyes
Anthraquinone dye	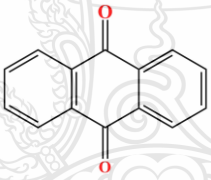	Alizarin, Indanthrene Blue
Nitro dye		Picric acid, Martius Yellow, Fast Red A
Nitroso dye	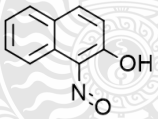	Martins Yellow, Naphthol green, Palatine orange
Indigo dye	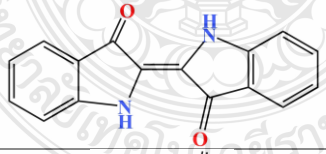	Indigo sol Violet
Phthalein dye	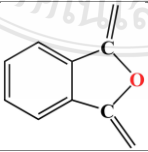	Phenolphthalein and Thymolphthalein
Trimethyl methane dye	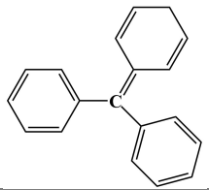	Crystal Violet, Malachite Green, Rhodamine B

Table 2.7 Classification of synthetic dyes

Type of dye	Feature
Acid dyes	Acidic or neutral conditions
Basic Dyes	Dyeing of jute, cut flowers, dried flowers, coir, etc.
Direct Dyes	Such as cotton, jute, viscose, or paper, without employing other mordants.
Disperse Dyes	Synthetic fibers like polyester and acetate require low-temperature dyeing, below 100°C
Reactive Dyes	Natural fibers like cotton & rayon: dye with reactive dyes for wash-fast results
Azoic Dyes	Textile, printing, paper manufacturing, etc.
Solvent Dyes	Solvent dyes, color fuels, plastics, and more.
Food Dyes	Specifically designed for coloring food products.
Hair Dyes	There are various hair dyes, including temporary, semi-permanent, and permanent dyes.
Vat Dyes	These dyes are suitable for cellulose fibers and are often used for dyeing denim.
Sulfur Dyes	Used for dyeing cellulose fibers.

❖ **Difference between dyes and pigments**

Dyes and pigments are distinguished primarily by their application methods and chemical compositions. Dyes are typically soluble substances that impart color to materials through chemical interactions, often forming covalent bonds with the substrate [32]. This process is essential for achieving the desired colorfastness and durability, as the dye molecules chemically interact with the fibers of the material being colored [32]. In contrast, pigments are insoluble particles that are finely ground and suspended in a medium, providing color through light absorption and reflection without forming chemical bonds with the substrate [33]. As shown in Table 2.9.

Table 2.8 The difference between dyes and pigments.

Character	Dye	Pigment
Dissolution	Ability to dissolve, especially in water	Insoluble in other solvents
Use	Use the dye in a water-based dye bath	Disperse in the medium and then merge into the object
Chemical elements	Only organic matter	inorganic compounds
Shades	Give all the Shades	Give white and other colors according to the type of metal that is the element
Application	Used for the textile, paper, and leather industries	Used as house paint, ink in document printers, and as an additive in plastics

2.2.2 Toxicity of dyes

The toxicity of synthetic dyes poses significant risks to both human health and the environment, necessitating effective remediation strategies. Industrial dye effluents are particularly concerning due to their carcinogenic properties and high visibility, which can lead to severe ecological consequences even at low concentrations [34], many synthetic dyes, such as azo dyes, are known for their persistence in the environment and potential to bioaccumulate, resulting in food chain contamination that adversely affects both human and animal health [35]. As shown in Table 2.10.

Table 2.9 Toxicology information on type dyes

Dyes type	Toxicity
Acid	Cancer & DNA damage
Basic	Gut & lung woes
Direct	Super toxic
Disperse	Toxic chemicals in clothes
Reactive	Half are toxic & cancer-causing
Vat/industrial	Dye waste harms health & environment
Azo	Stable but potentially harmful
Solvent	Pollutes water & might harm you
Food	Colorful waste, potential toxins & cancer risks
Hair	Mercury lurking in some dyes

2.2.3 Indigo Carmine Dye (IC)

The molecular formula of indigo carmine dye, commonly referred to as Indigotindisulfonate, Indigota, or acid blue 74, is ($C_{16}H_8N_2Na_2O_8S_2$), and its LD_{50} is greater than 2,000 mg/kg. This kind of dye is made up of sodium salts in an organic manner. The IC dye's structure [36]. As shown in Figure 2.2.

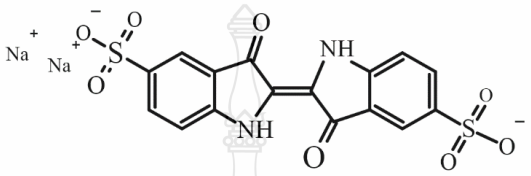

Figure 2.2 Structure of IC dye.

2.2.4 Reactive Black 5 Dye (RB5)

The molecular formula of Reactive Black 5 Dye (RB5) dye, molecular formula of Reactive Black 5 (RB5) dye is $C_{26}H_{21}N_5Na_4O_{19}S_6C_{26}H_{21}N_5Na_4O_{19}S_6$. The LD_{50} (lethal dose for 50% of the population) of Reactive Black 5 (RB5) dye varies depending on the organism and the route of exposure [37]. For mice, the reported LD_{50} values are Oral (mice) 2,000 mg/kg and Intraperitoneal (mice) 750 mg/kg. The RB5 dye's structure. As shown in Figure 2.3

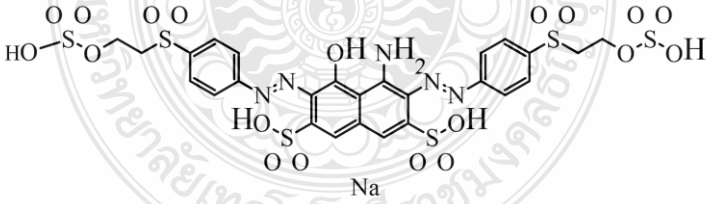

Figure 2.3 Structure of RB5 dye.

2.3 The photocatalytic process principle

The photocatalytic process is inextricably linked to the band structure of semiconductors, which is defined by a vacant conduction band (CB) and a filled valence band (VB) that are separated by a band gap [38]. This configuration enables the excitation of electrons from the VB to the CB upon light absorption, resulting in the generation of electron-hole pairs (e^-) and (h^+) that are crucial for photocatalytic reactions. To improve efficiency,

semiconductor surface or bulk (e^-) and (h+) coupling recombination must be reduced [38]. Doping with conductive graphene reduces recombination and prolongs charge carriers to increase photocatalytic activity, that electron donors and acceptors enable redox processes to boost photocatalytic efficiency [38]. As shown in Figure 2.4.

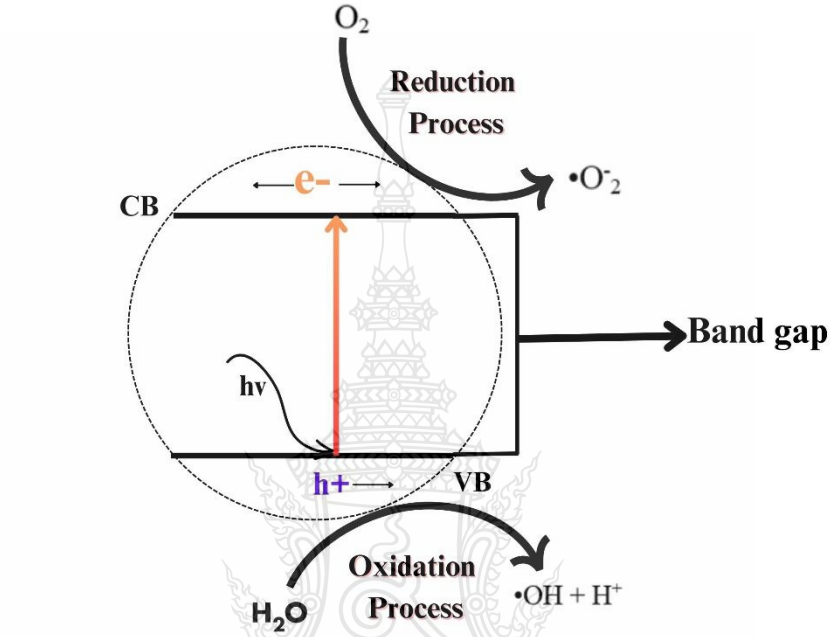

Figure 2.4 Mechanism of photodegradation in the photocatalytic process

- **Mechanisms in the Photocatalytic process**

The photocatalytic process comprises complex oxidation and reduction reactions assisted by semiconductors like TiO_2. Light activates the photocatalyst, which adsorbs water during oxidation. Photogenerated holes (h^+) in the valence band oxidize water to produce extremely reactive hydroxyl radicals (•OH). Hydroxyl radicals degrade organic contaminants into CO_2 and H_2O [39]. photocatalysts holes immediately oxidize organic pollutants [39].

Excited electrons (e^-) and dissolved oxygen form superoxide radicals ($•O_2^-$) in the reduction side conduction band. Following light absorption, superoxide radicals can transform into hydroperoxyl radicals (•HO) and hydrogen peroxide (H_2O_2), contributing to oxidation by generating hydroxyl radicals [40, 41]. These radical species destroy pollutants and create ROS; thus, photocatalytic efficiency depends on their balance [40, 41]. The aforementioned response is presented in Equations (2.3)– (2.11).

$$h^{+}_{VB} + H_2O \longrightarrow \bullet OH + H^{+} \quad (2.3)$$

$$h^{+}_{VB} + OH^{-} \longrightarrow \bullet OH \quad (2.4)$$

$$e^{-}_{CB} + O_2 \longrightarrow \bullet O^{-}_2 \quad (2.5)$$

$$H^{+} + \bullet O^{-}_2 \longrightarrow \bullet OH_2 \quad (2.6)$$

$$2H_2O + \bullet O^{-}_2 \longrightarrow 2H_2O_2 \quad (2.7)$$

$$H_2O_2 \longrightarrow 2\bullet OH_2 \quad (2.8)$$

$$H_2O_2 + \bullet O^{-}_2 \longrightarrow \bullet OH^{-} + \bullet OH + O_2 \quad (2.9)$$

$$e^{-}_{CB} + H_2O_2 \longrightarrow OH^{-} + \bullet OH \quad (2.10)$$

$$\bullet OH + R \longrightarrow CO_2 + H_2O \quad (2.11)$$

e^{-}_{CB} = Electrons in the conduction band (CB)

h^{+}_{VB} = Hold at Valence Band (VB)

•OH = Hydroxyl radicals

$\bullet O^{-}_2$ = Superoxide radicals

H_2O_2 = hydrogen peroxide

- **Catalyst type**

Through light energy, a material known as a photocatalyst can improve a chemical process. Among many other uses, energy conversion and environmental remediation depend critically on the photocatalytic process. Usually, semiconductors, photocatalysts capture photons or light particles using that energy to start chemical reactions. The several kinds of photocatalysts.

Usually available, durable, and reasonably priced, metal oxides are the main photocatalysts used in this regard. These are a few examples:

- **Titanium dioxide (TiO_2)**

Essential components that enable chemical reactions by light absorption are photocatalysts; metal oxides are most common because of their stability, availability, and low cost. One well-known example that exists in three crystal phases: anatase, rutile, and brookite, is titanium dioxide (TiO_2). Because of its favorable light absorption characteristics and stability, anatase, with a band gap of about 3.2 eV, showcases the highest photocatalytic activity [42]**.** Although more stable and with a somewhat smaller band gap of around 3.0 eV, rutile is often less photoactive than anatase [42]**.** Rarely used in photocatalytic applications,

Brookite-characterized by a band gap of around 3.3 eV, has restricted availability and smaller activity [42]. As shown in Figure 2.5.

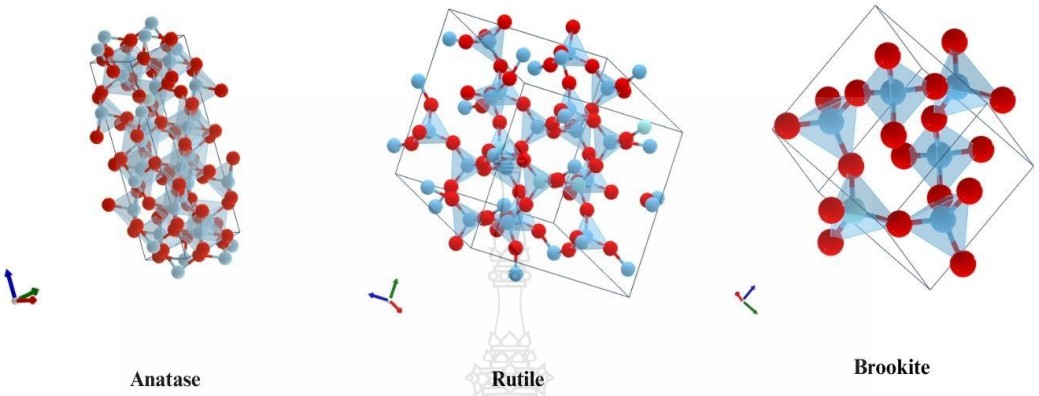

Figure 2.5 Basic crystal structure of titanium dioxide

- **Zinc oxide**

Zinc oxide nanoparticles (ZnO NPs) find applications in photoprotection, antimicrobial therapies, and photocatalysis, contributing to their widespread popularity. ZnO nanoparticles effectively absorb UV radiation in sunscreens, providing protection and facilitating wound repair [43]. The capacity to absorb UV radiation while preserving transparency positions them as a remarkable option for cosmetic formulations. The fact that these nanoparticles can penetrate the skin and release toxic zinc ions is one reason why their safety is a source of concern [43]. Because of its enhanced mechanical and antimicrobial characteristics, ZnO composites are well-suited for use in orthodontics.[43]. As shown in Figure 2.6.

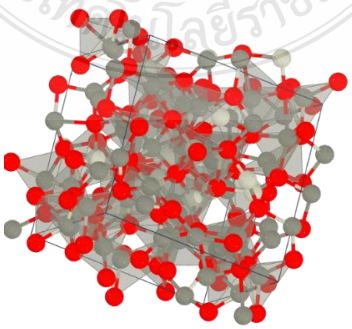

Figure 2.6 Crystal structure of Zinc Oxide

Non-metal oxides: These offer advantages like tunability and band gap engineering, but can be more expensive or less stable:

- **Graphene Oxide and Reduced Graphene Oxide (RGO)**

Graphene oxide, or GO, is a form of graphene that has several functional groups attached to it, such as hydroxyl, epoxy, and carboxyl, and a very high specific surface area. Because of these characteristics, GO has a wide range of potential uses in the fields of materials science, physics, and medicine [44]. Graphene oxide (GO) and reduced graphene oxide (RGO) are ideal materials for environmental cleaning due to their unique features that aid in photocatalysis and heavy metal removal. Their large surface area allows them to possibly absorb more contaminants, so they are more helpful in particular contexts [45]. As Figure 2.7 shows, functional groups like hydroxyl and carboxyl in GO make GO reactive and able to interact with many kinds of pollutants. RGO is therefore more valuable in environmental uses as some of these groups remain even after reduction [45].

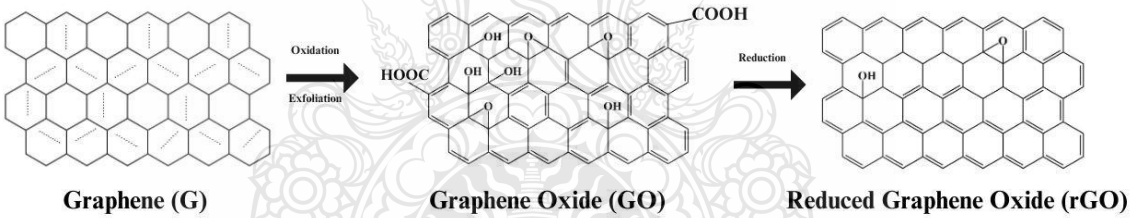

Figure 2.7 introduces the GO and RGO production processes and chemical structures.

Additional catalysts are being researched and produced in an effort to increase photocatalytic processes. Such materials as $BaTiO_3$, WO_3, $SiTiO_3$, TiO_2, ZnO, ZnS, CdS, CdSe, and RGO are continuously used in industry and the environment, as shown in Table 2.10.

Table 2.10 Energy band gap sizes of various catalysts

Photocatalyst	Energy band gap size (eV)
$BaTiO_3$	3.30
WO_3	2.70
$SiTiO_3$	3.40
TiO_2	3.20
ZnO	3.20
ZnS	3.20
CdS	2.50
CdSe	1.70
RGO	2.20

Titanium dioxide (TiO_2) is one of the most well-known photocatalysts, although there are other substances as well, such as zinc oxide (ZnO), reduced graphene oxide (RGO), and Graphite carbon nitride gC3N4 shown in Table 2.11.

Table 2.11 Details on the differences in photocatalysts

Parameter	Unit	Metal oxides			Non-metal oxides	
		TiO_2	ZnO	WO_3	gC_3N_4	RGO
Molecular Weight	$g.mol^{-1}$	79.87	81.40	231.84	Variable	10,000 –100,000
Appearance, Existence	N/A	White powder	White powder, Zincite	Yellow solid	Yellow to pale beige powder	Black powder or flakes
Solubility	N/A	Insoluble in H_2O and alcohol		Insoluble in most solvents		
Energy gap	eV	3.20	3.37	~2.7	~2.7	2.2
Thermal conductivity	$W.mK^{-1}$	11.7	50 (R, T)	0.9	Low	Up to 5,000

- **Preparation of the catalyst**

Catalyst preparation is crucial for various chemical processes, from large-scale manufacturing to environmental remediation and organic synthesis. Important factors to consider: stability, environmental impact, and practical application. shown in Table 2.13.

Table 2.12 Details of catalyst preparation methods

Method	Description	Advantages	Disadvantages
Sol-gel process	Creates catalysts with high surface area and controlled pores.	Simple, versatile, wide range of catalysts.	Can be difficult to control properties.
Hydrothermal solvothermal synthesis	Creates catalysts with unique morphologies and controlled crystal structures.	Versatile, various properties, zeolite catalysts.	High pressure and temperature requirements.
Co-precipitation	Produces catalysts with multiple active components.	Control interaction between components affects activity and selectivity.	Difficult to optimize the co-precipitation process.
Direct oxidation	Prepares metal oxide catalysts.	Simple, and efficient for metal oxide catalysts.	Limited control over morphology and crystallinity.
Microwave irradiation	Fast and energy-efficient catalyst synthesis.	High purity and crystallinity.	Scalability can be challenging for large-scale production.

2.3.5 Light source

The sun is the principal source of natural light, generating a range of electromagnetic waves, including visible light, vital for life on Earth. Celestial bodies and other natural occurrences, such as bioluminescence and lightning, enhance the natural illumination of the surroundings [46, 47]. Other natural sources encompass the phenomenon of lightning. Artificial light sources, such as light-emitting diodes (LEDs) and incandescent bulbs, are designed to provide illumination for certain purposes and are frequently adapted to replicate the qualities of natural light. Ultraviolet light is essential in photocatalytic processes, since it activates photocatalysts that promote the breakdown of contaminants. Table 2.14 demonstrates that UV radiation, invisible to the human eye, may be classified into three specific categories according to wavelength: ultraviolet A, ultraviolet B, and ultraviolet C. The varying ranges impose a particular impact on photocatalytic efficiency.

Table 2.13 Wavelengths in various ranges

UV Range	Wavelength (nm)	Description	Effect on Photocatalysis
UVA	320-400	Long wavelength, low energy	Minimal or no influence
UVB	280-320	Shorter wavelength, higher energy	Moderate influence can excite some photocatalysts
UVC	100-280	Shortest wavelength, highest energy	Strong influence, most effective for photocatalysis

Note:

UV rays must be used wisely. This is especially true in photocatalytic industrial and wastewater treatment operations, as UV radiation may still harm skin and eyes. When working with UV light sources, safety is paramount.

2.4 Hydrothermal synthesis

Hydrothermal methods are a group of techniques used to crystallize materials from high-temperature and high-pressure aqueous solutions. As shown in Table 2.15, these methods are commonly used in the synthesis of nanomaterials, such as nanoparticles, nanowires, and nanotubes.

Table 2.14 Synthesis Technique

Synthesis Technique	Temperature Range	Pressure Range	Advantages	Disadvantages
Hydrothermal	100°C - 1000°C	1 - 100 MPa	High control over crystal structure, good for growing large crystals	High cost, requires specialized equipment
Solvothermal	50°C - 300°C	1 - 20 MPa	A wider range of solvents can be used for sensitive materials	Lower control over crystal structure
Solid-state	Room temperature - 1500°C	0.1 atm - 100 atm	Simple to set up, can be used for a variety of materials	Difficult to control crystal growth

- **Hydrothermal synthesis process**

The advantages of hydrothermal methods include their ability to produce monodispersed and crystalline materials and the potential for tailoring the properties of the synthesized nanomaterials through careful manipulation of synthesis parameters [77]. can show Table 2.16

Table 2.15 Advantages and Disadvantages of Hydrothermal Synthesis.

Advantages	Disadvantages
Precise control of material properties	High capital cost
A wide range of materials synthesized	Limited scalability
Relatively mild reaction conditions compared to solid-state synthesis	Safety concerns
Environmentally friendly	Difficult process optimization
Scalability potential	Limited in-situ monitoring

2.5 Micro/Nano Bubble

Micro-nanobubble technology leverages the unique characteristics of bubbles that vary in size from the micrometer to the nanometer scale. These properties together lead to a marked improvement in gas dissolution and extended stability in liquid settings. The extensive surface area enables the dissolution of significantly greater concentrations of gases, like oxygen and carbon dioxide, into water when compared to traditional methods. Additionally, their restricted buoyancy guarantees a slower ascent rate, allowing sufficient time for engagement with the liquid phase, a crucial feature for their use in water treatment and biomedical applications [49]. Moreover, the existence of a minor negative charge on their surface inhibits particle aggregation, thus preserving their stability for extended periods [49]. The classification is based on size-nanobubbles (under 1 μm), microbubbles (1–100 μm), and macrobubbles (100 μm to 2 mm). highlights their wide-ranging applications, from supporting plant growth to improving oxygen delivery in low-oxygen environments [49], as shown in Figure 2.17.

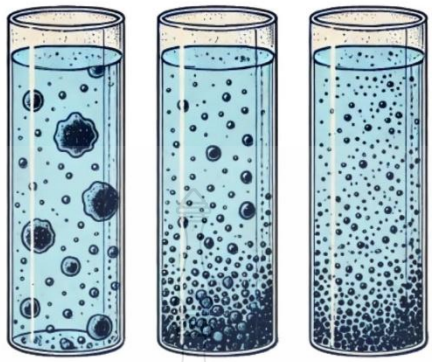

(A) macro bubbles (B) microbubbles (C) Nano bubbles

Figure 2.8 Bubbles of different sizes

Table 2.16 Application of each type of micro and nanobubbles

Type	Applications
Macro Bubble	- Limited applications in photocatalysis - Used in flotation and aeration processes
Micro Bubble	- Enhanced gas transfer efficiency - Wastewater treatment - Drug delivery - Photocatalytic reactions
Nano Bubble	- Photocatalysis with enhanced reaction rates - Medical imaging - Cancer treatment - Water purification

2.6 Characterization techniques

The unique characteristics of nanoparticles ranging from 1 to 100 nanometers make them appealing for applications in medicine, electronics, and catalysis. To enhance the potential of nanoparticles, examine their physicochemical properties. This article provides an overview of XRD, XPS, FTIR, FESEM-EDS, TEM, and UV-visible spectroscopy. These works demonstrate the necessity of utilizing various methods to comprehend the nanoparticle phase, morphology, surface chemistry, specific surface area, and optical properties.

2.6.1 X-ray diffraction (XRD)

The distinct scattering of X-rays by the orderly arrangement of atoms in a crystal lattice establishes XRD as an essential technique for analyzing crystalline materials. X-rays engage with crystalline structures, producing patterns of constructive and destructive interference, which are governed by Bragg's rule to ascertain the crystalline phase and structural characteristics of the material [50]. Since reactants and solvents absorb microwave energy well, traditional and microwave heating methods improve XRD analysis by ensuring uniform energy distribution and accurately assessing crystalline phases.

Studies showing that XRD can analyze metals and ceramics show its crystallinity-revealing capabilities. XRD peak narrowing with temperature coincides with bigger crystallite sizes, indicating enhanced crystallinity; the technique's non-destructiveness makes it useful for studying delicate materials' structural features [50]. XRD is a key tool in materials research for understanding crystalline structures. For the tangential surface, the sample is subjected to an X-ray beam with a wavelength (λ) and angle (θ). As per the equation (2.12), the pattern appears at an angle 2θ during diffraction.

$$n\lambda = 2d_{hkl}\sin\theta \qquad (2.12)$$

In the equation, n indicates the diffraction order, λ is the incident beam wavelength in nanometers, dhkl is the diffracting hkl plane lattice spacing, and θ is the scattering angle.

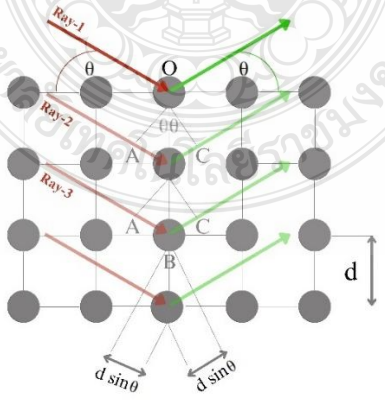

Figure 2.9 The geometry of wave interference between two planes separated by a distance, d.

2.6.2 X-ray photoelectron spectroscopy (XPS)

X-ray photoelectron spectroscopy (XPS) is a crucial analytical technique for investigating the surface composition of materials across various chemical environments. This provides empirical measurements of elemental composition, demonstrating how the formula, chemical, and electronic state influence the surface and interface properties of nanostructured materials [51]. In XPS, particular energy photons interact with electrons in atoms to expel them from the solid surface. By use of the kinetic energy of the released electrons, this method helps to identify the component materials [51]. As Figure 2.18 shows, the representation of the X-ray photoelectron process emphasizes the fundamental interactions underlying this analytical method.

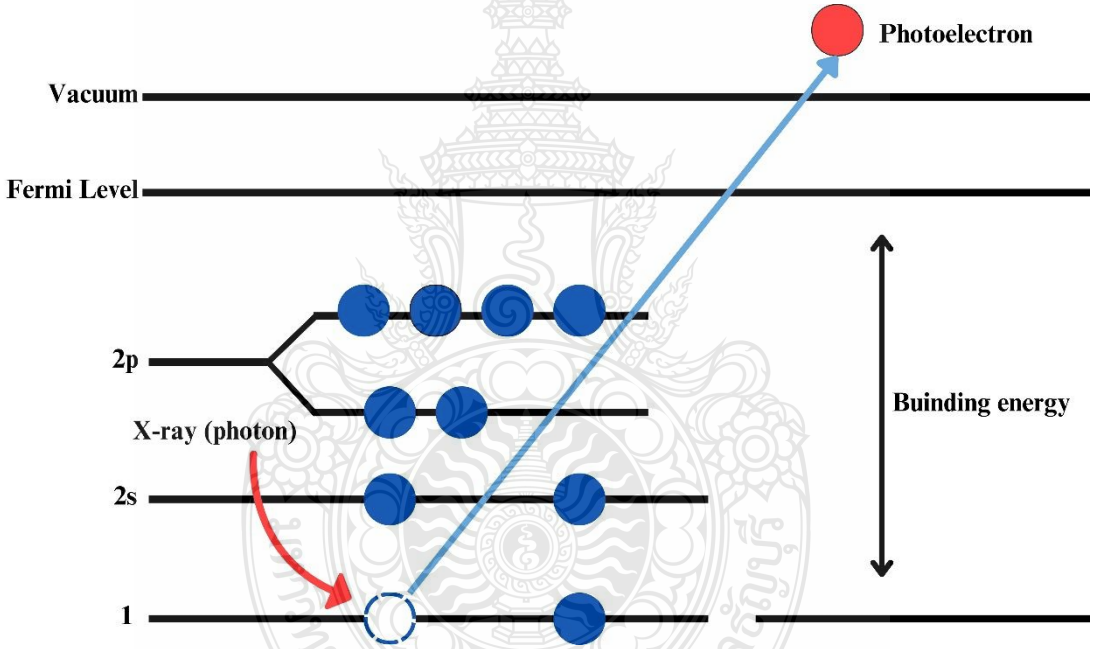

Figure 2.10 Schematic representation of the X-ray photoelectron process

Powerful analytical method for investigating material surfaces, X-ray photoelectron spectroscopy (XPS) offers useful data on elemental composition, chemical states, and surface features. The references underline the broad uses of XPS in many disciplines, including materials science, chemistry, and surface analysis, thus stressing its importance in expanding knowledge of the characteristics of different materials and so supporting research.

2.6.3 Fourier transform infrared spectroscopy (FT-IR)

Fourier transform infrared spectroscopy (FT-IR) detects molecular vibrations at specific wavelengths for chemical process study. The stretching, contraction, and bending vibrational modes of chemical bonds are prevalent in the 4000 to 400 cm^{-1} region of the intermediate infrared spectrum [52]. The infrared spectra of molecules may be used to identify functional groups [52]. This is because molecules absorb light differently in this region.

One of the most flexible methods for analyzing chemical composition is called Fourier transform infrared spectroscopy, or FT-IR for short. Its ability to provide quantitative and qualitative data on functional groups, molecular structures, and sample compositions makes it a vital instrument for a broad spectrum of uses, including environmental investigation, study in materials science, cancer detection, and other fields.

2.6.4 Electron microscopy

TEM and SEM are essential microstructure analysis methods with different benefits. SEM scans sample surfaces to provide comprehensive topographical pictures of tissue, macromolecular aggregation, and material surfaces [53].TEM provides high-resolution imaging of interior structures for atomic-level material analysis [53]. Both methods use an electron gun, electromagnetic lenses, and other light microscope components to make pictures [53]. As shown in Figure 2.19 and Table 2.18.

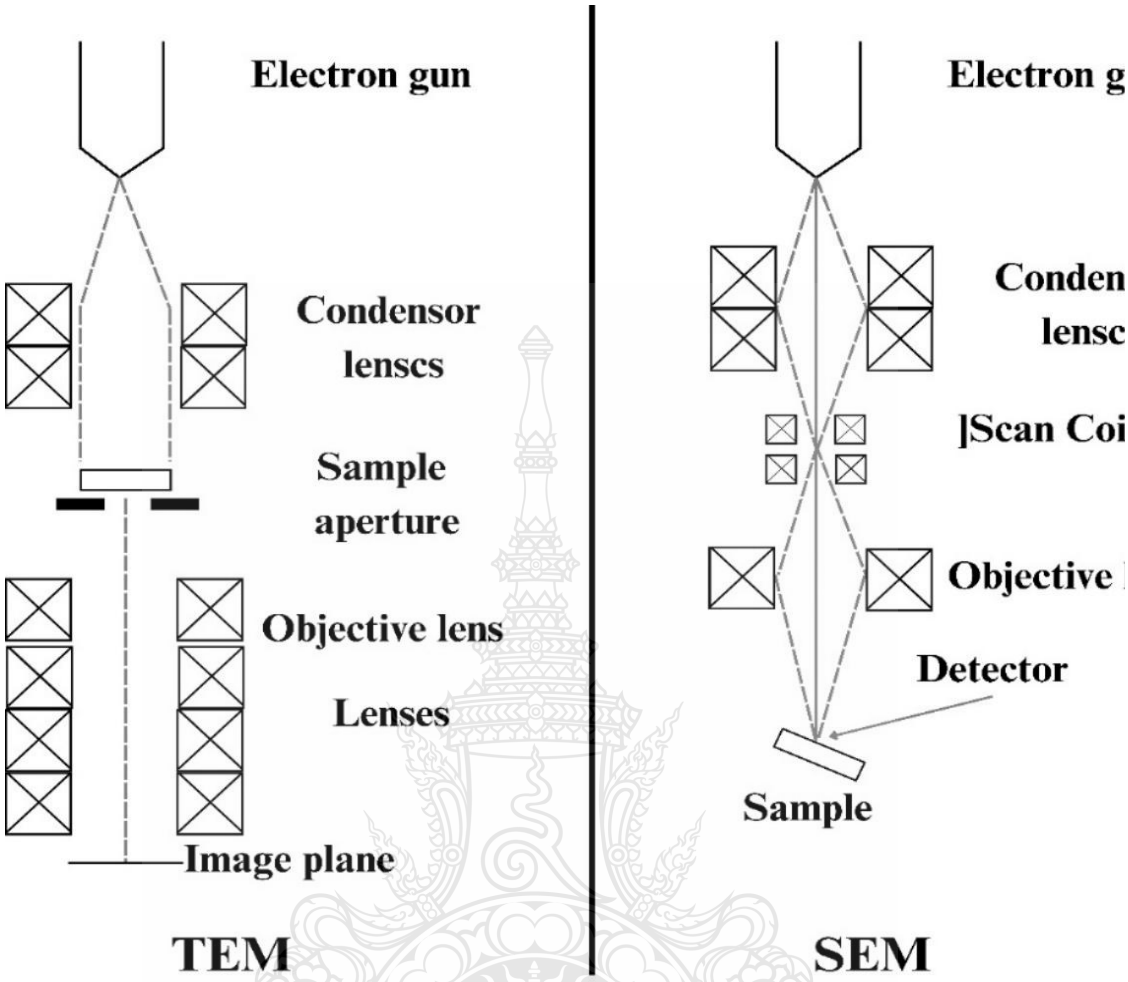

Figure 2.11 The diagram illustrates the configuration of an electron microscope operating in both transmission (TEM) and scanning (SEM) modes

Table 2.17 The fundamental concept underlying both transmission electron microscopy (TEM) and scanning electron microscopy (SEM) techniques

Aspect	(TEM)	(SEM)
Basic Principle	Uses transmitted electrons to form an image.	Uses scattered electrons to form an image.
Electron Source	An electron gun emits electrons that pass through the sample.	An electron gun emits electrons that scan the sample surface.
Sample Interaction	Electrons transmit through a very thin sample.	Electrons interact with the surface of the sample.
Image Formation	The image is formed from transmitted electrons.	The image is formed from secondary or backscattered electrons.
Resolution	Higher resolution (up to atomic level).	It has a lower resolution compared to TEM.
Sample Preparation	Requires ultra-thin samples (typically <100 nm).	Requires conductive samples or coating with conductive material.
Depth of Field	Limited depth of field.	Greater depth of field.
Applications	Detailed internal structure and crystallography analysis.	Surface morphology and composition analysis.
Magnification Range	Very high magnification (up to millions of times).	It has a lower magnification compared to TEM (up to hundreds of thousands of times).
Operational Mode	Typically operates in a vacuum.	Operates in a high vacuum, but environmental SEM (ESEM) can operate under variable pressures.

2.6.4 UV-visible spectroscopy (UV-vis)

Ultraviolet-visible (UV-Vis) spectroscopy is a fundamental analytical technique utilized to measure the absorption, transmission, and emission of UV and visible light by solutions. This method is particularly valuable for examining molecules' electronic structures and chemical environments, facilitating reaction monitoring and quantitative analysis [54]. When a molecule or ion absorbs UV or visible light, it triggers an electronic transition, causing electrons to move from lower to higher energy levels. This phenomenon provides critical insights into changes in electronic energy levels, which can indicate various chemical processes shown in Table 2.19.

Table 2.18 The details and components of UV-visible spectroscopy as described

Aspect	Description
Measurement	• Absorption, transmission, and emission of ultraviolet and visible light by a solution
Applications	• Electronic structure analysis, chemical environment examination, reaction monitoring, quantitative analysis
Principle	• Molecule or ion absorbs UV or visible light, triggering electronic transitions
Information Provided	• Changes in electronic energy levels due to electron transfer
Components	• Light source, sample holder, diffraction grating, container, photoelectric detector, signal processor, printout
Sample Containers	• Made from optical materials like glass, plastic, and silica; glass and plastic are common but limited to visible wavelengths due to UV absorption
Light Sources	• Tungsten-halogen, deuterium, and xenon arc lamps
Monochromator	• Entry slit, collimating lens, dispersion device, focusing lens, exit slit; produces monochromatic light
Spectrometer Types	• Single-beam and double-beam
Single Beam Device	• Analyze one wavelength at a time using a monochromator between the source and sample
Double Beam Instrument	• Uses a single source, monochromator, splitter, and mirrors to connect the beam to the reference sample and the sample to be analyzed
Detector	• Diode array detector to detect absorbance at all wavelengths simultaneously
Operation	• Passes light of a certain wavelength through a sample solution and onto a photoelectric cell, converting radiant energy into electrical energy measured by a galvanometer

2.6.5 Gas Chromatography-Mass Spectrometry (GC-MS)

GC-MS is recognized as a primary tool for determining volatile compounds, particularly in scenarios requiring precise identification of volatile substances. The technique is commonly employed to analyze various substances within liquid or volatile samples, with headspace-solid-phase microextraction (HS-SPME) frequently utilized for the rapid and efficient extraction and isolation of volatile compounds [55]. For instance, studies have demonstrated the effectiveness of GC-MS in characterizing volatile profiles in food products,

such as the identification of key aroma-active compounds in teas and the analysis of flavor compounds in various food matrices [56], as shown in Figure 2.20.

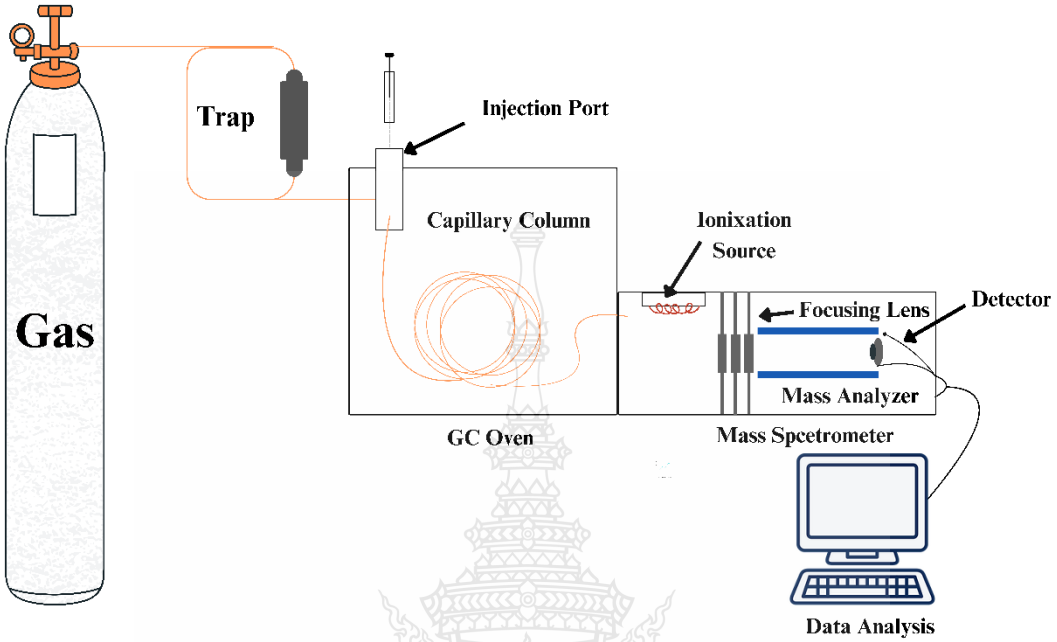

Figure 2.12 GC-MS Systems.

The versatility and sensitivity of GC-MS make it an indispensable tool in food science, environmental analysis, and chemical research **[57]**. This method plays a crucial role in the qualitative and quantitative determination of volatile compounds, making it a valuable tool in various fields such as food science, medicine, and biology, as shown in table 2.20.

Table 2.19 Gas Chromatography-Mass Spectrometry (GC-MS) Applications, Advantages, and Limitations.

Category	Details
Applications	• Environmental analysis, forensic science, food industry, detection of pollutants, drugs, and flavors
Advantages	• High sensitivity and specificity, capable of identifying compounds in complex mixtures, quantitative analysis with high accuracy
Limitations	• Limited to volatile and semi-volatile compounds; sample preparation can be time-consuming and requires extensive method development and optimization.

GC-MS stands out as a versatile and indispensable analytical tool for the identification and quantification of volatile compounds in diverse samples. It offers high accuracy and sensitivity in compound analysis across various scientific disciplines.

2.7 Kinetics of photocatalytic reactions

Fundamental Chemical Reactions: Examine a typical second-order reaction that exhibits the following features:

$$A+B \rightarrow products$$

It is assumed that the reaction rate is influenced by both A and B concentrations, characterizing it as a second-order reaction.

$$r=-\frac{d[A]}{dt}=k[A][B] \qquad (2.1.3)$$

Here:

- k = reaction rate constant
- $[A]$ and $[B]$ = reactant concentrations A and B

Pseudo-first-order reaction assumption To simplify calculations, it is assumed that the concentration of one reactant (B) is sufficiently high that it remains effectively constant throughout the reaction. Consequently, the equation for the reaction rate is modified to equations (2.1.4):

$$r=-\frac{d[A]}{dt}=k[A][B]\approx k'[A] \quad (2.1.4)$$

Solving differential equations derived from velocity equations (2.1.5):

$$-\frac{d[A]}{dt}=k'[A] \quad (2.1.5)$$

To isolate the variable, multiply both sides of the equation (2.1.6) by 1/[a].

$$-\frac{d[A]}{[A]}=k'dt \quad (2.1.6)$$

Performing the integration of Equation (2.1.7) The subsequent phase involves integrating this equation, considering the time frame (from *t=0* to *t=t)* and the concentration of *A (*from *[A]=C₀* to *[A]=C)*:

$$-\int_{C_0}^{C}\frac{d[A]}{[A]}=k'\int_{0}^{t}dt \quad (2.1.7)$$

Integration to get the result:

$$In\frac{C}{C_0}=-k't \quad (2.1.8)$$

The final formula obtained by considering the pseudo-first-order reaction is:

$$In\frac{C}{C_0}=k't \quad (2.1.9)$$

This formula can be used to calculate the change in concentration of substance A concerning time when the rate constant k' and the initial concentrations C_0 of the reactants are known.

2.8 Related research

The photocatalytic degradation of pesticides and dyes using TiO_2 is of significant interest for environmental remediation. This review summarizes 10 research papers on TiO_2's role in degrading chemical pesticides and dyes. Topics include the photocatalytic degradation of organic dyes, parameters affecting the process, synthesis and characterization of TiO_2 nanocomposites, and applications in treating textile dyeing wastewater. The review addresses challenges and prospects in TiO_2-based photocatalytic degradation [58-63].

Table 2.20 Applications in Photocatalytic Degradation

Main Focus	Key Findings	Potential	Challenges
Wide applications of TiO_2 nanoparticles	Emphasizes wastewater treatment and space applications	Significant potential for various fields	Not specified
TiO_2 nanocomposites for environmental remediation	The potential of TiO_2 in water splitting and UV radiation	Promising environmental cleanup	Long-term stability and cost-effectiveness
Orange dyes and carbamazepine removal	Enzymatic and photocatalytic treatment methods	Effective for specific pollutants	Optimization of the treatment process
Organic dye degradation using N-doped TiO_2	Visible light photocatalysis	Efficient degradation under sunlight	Regeneration and reusability of photocatalyst
Ag-doped ZnO nanorods/RGO nanocomposites	Enhanced photocurrent generation and photocatalysis	Improved efficiency for photo-electrochemical applications	e^- and h^+ separation efficiency and stability
ZnO/graphene composites for organic dye degradation	One-step electrodeposition	Challenges in electron-hole separation efficiency	Overcoming limitations for improved performance
Hybrid RGO@TiO_2/CN nanocomposites	Enhanced photocatalytic activity	The potential of nanocomposites for efficient degradation	Scalability and cost-effective synthesis
Photocatalytic disinfection and purification of water	RGO/TiO_2 composites	RGO enhances TiO_2 efficiency in water processing	Long-term stability and potential environmental impacts

CHAPTER 3
RESEARCH METHODOLOGY

3.1 Chemicals and Instruments

3.1.1 Chemicals

1) Titanium dioxide photocatalyst Nanopowder (TiO_2, >95%, SRL)
2) Zinc Oxide (ZnO, 99%, SRL)
3) Methyl Alcohol, HPLC Grade (CH_3OH, ≥98% MACRON),
4) Reduced Graphene Oxide (rGO, ≥99.5%, Nanografi)
5) Carbaryl ($C_{12}H_{11}NO_2$, 99%, 1-naphthyl methyl carbamate, Dr. Ehrenstorfer)
6) Indigo carmine ($C_{16}H_8N_2Na_2O_8S_2$, HIMEDIA)
7) Reactive Black 5 ($C_{26}H_{21}N_5Na_4O_{19}S_6$, HIMEDIA)

3.1.2 Instruments

1) Beakers 25, 50, 125, 600 mL and 1,000 mL
2) Erlenmeyer flask 250 mL
3) Glass funnel, and Gloves
4) Laboratory Coat
5) Respiratory mask
6) Stirring rod
7) Burette
8) Micropipette
9) Weighing bottle
10) pH paper test strips
11) Syringe (5 mL)
12) Nylon Syringe filter, 0.2 µm, FILTREX
13) Measuring cylinder 100 mL
14) Volumetric flasks 10, 25, 50, 100, 500 and 1,000 mL
15) 50 mL plastic sampling bottle
16) Magnetic Stirrer and Magnetic Bar
17) Elma Elmasonic E30H 2.75 Liter Heated Ultrasonic Cleaner

18) Wash bottle

19) Electromagnetic scale

20) Hydrothermal Autoclave Reactor Model w/PTFE Lined 250 mL

21) Hot air Oven Model OV-9123A

22) Photoreactor (Figure.3.1)

23) Micro-nano bubble aerator Model RMUTT-MNB

24) Nano Sight NS300 (Malvern Panalytical)

25) Color measurement device MERCK Prove 100 ADMI spectrometer

26) UV Spectrophotometer Single Monochrome Type U-3900

27) X-Ray Diffractometer (XRD) Model Smart Lab

28) Scanning Electron Microscope and Energy Dispersive X-ray Spectrometer – SEM-EDS (7610F) Model AXIS Ultra DLD

29) X-ray photoelectron spectroscopy (XPS) Model AXIS Ultra DLD

30) Transmission electron microscope (TEM) Philips Model TECNAI 20

31) Fourier Transform Infrared Spectrometer (FT-IR) RFT-6000 FT Raman Spectrometer

32) Brunauer-Emmett-Teller (BET) BELSORP-max Bel Japan Inc

33) UV Spectrometer model Tensor27, Microscope model Hyperion 3000

34) Gas Chromatography-Mass Spectrometry (GC-MS) Model GC6890N-MS5973N

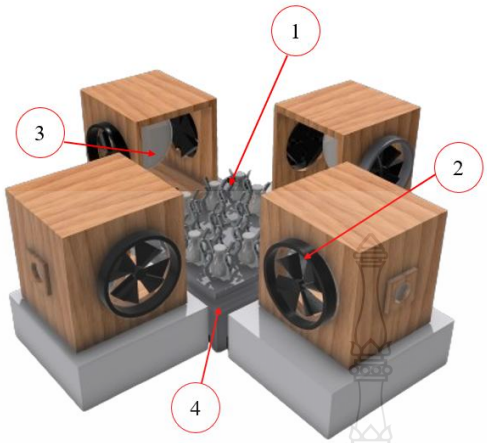

1) Erlenmeyer flask
2) Ventilation fan
3) UVA light source
4) Shaker

Figure 3.1 Photoreactor

3.2 Preparation of Photocatalyst

3.2.1 Preparation of TiO_2/ZnO/rGO photocatalyst (TZR)

The preparation of four types of photocatalysts, including TiO_2/ZnO (TZ), TiO_2/RGO (TR), ZnO/RGO (ZR), and TiO_2/ZnO/RGO (TZR) nanocomposites, was carried out as follows:

To create the TZ photocatalyst, 4 g of TiO_2 and 4 g of ZnO were mixed and then stirred for 30 minutes in 120 mL of deionized (DI) water. The TR photocatalyst was prepared by combining 4 g of TiO_2 with 0.05 g of reduced graphene oxide (rGO) in 120 mL of DI water, followed by 30 minutes of stirring and ultrasonication. Similarly, the ZR photocatalyst was synthesized using 4 g of ZnO and 0.05 g of rGO in 120 mL of DI water, undergoing the same stirring and ultrasonication process for 30 minutes. The TZR photocatalyst was synthesized by combining 4 g of TiO_2, 4 g of ZnO, and 0.05 g of rGO in 120 mL of DI water and was subsequently subjected to the same stirring and ultrasonication procedure. Following the initial dispersion, all suspensions underwent an additional 60 minutes of continuous magnetic stirring to improve uniformity. Afterward, the prepared suspensions were placed into autoclaves and subjected to hydrothermal treatment at 180°C for 24 hours to promote controlled crystallization and composite formation. Once the process was completed, the autoclaves were allowed to cool down to room temperature. The resulting suspensions were then subjected to centrifugation at

4,000 rpm for 7 minutes to isolate the solid photocatalyst phase, after which the supernatant was removed. The precipitate was thoroughly washed with DI water through repeated stirring and centrifugation steps to effectively eliminate residual impurities. The purified photocatalyst was then dried at 70°C for 12 hours to remove moisture and ensure structural stability, as shown in Figure 3.2.

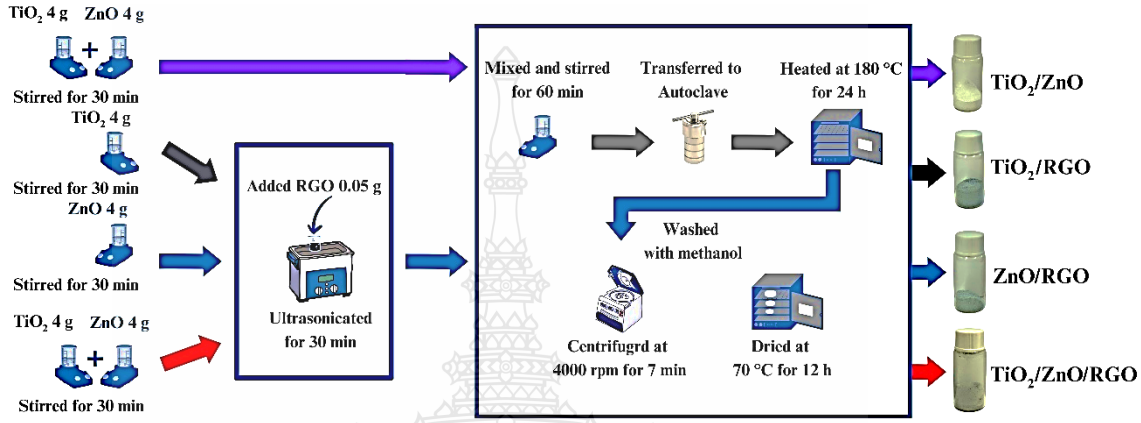

Figure 3.2 Preparation of all photocatalysts

3.3 Physical property characterization of TZR catalysts

Perform performance physical property analysis with the device using XRD, FTIR, XPS, SEM-EDS, TEM, and UV.

Table 3.1 The techniques for analysis of physical properties of catalysts

Physical properties	Analysis techniques	Instrument
Face structure and identify types of compounds.	XRD	PHI5000 model
Functional Group	FTIR	Brucker RFS27 spectrophotometer
Binding energy	XPS	Model AXIS Ultra DLD
Surface more metrology and Energy Dispersive	SEM-EDS	JEOL JSM-7610F, Oxford X-Max 20
Particle size and morphology	HR-TEM	JEOL JEM 2100
Surface area of solids and powders	BET	(BELSORP-max Bel Japan Inc).
Band gap	UV-vis DRS	Perkin Elmer Lambda 25 spectrometer
Analyze charge carrier recombination, detect defects, and gap	PL	(HORIBA Scientific, model: FLUOROMAX PLUS)

❖ **Evaluation of the efficiency of wastewater with contaminants by the photocatalytic process.**

Three distinct experimental setups were implemented to evaluate the photocatalytic degradation of dyes and pesticides, focusing on the role of micro-nanobubbles (MNB) in enhancing degradation efficiency.

The first setup (Experiment condition1-4) utilized an RMUTT-MNB generator to introduce dissolved oxygen (DO) into synthetic wastewater via MNB, achieving DO levels of 10-15 mg. L^{-1} after 15 minutes of aeration. A Malvern model NS300 nanoparticle tracking analyzer measured the size, distribution, and concentration of MNB to ensure consistency in experimental conditions.

The second setup (Experiment condition 5-8) investigated the photocatalytic process without MNB oxygenation, allowing for a comparative analysis of its impact on degradation efficiency.

The control setup (Experiment condition 9-10) served as a control, where degradation occurred under natural conditions without MNB or photocatalysts, providing a baseline for performance assessment. A detailed summary of experimental conditions,

selections of experiments to determine the most effective wastewater treatment method for maximum synthetic waste removal. Various concentrations of the Photocatalyst were analyzed and compared under different experimental conditions, as detailed in Table 3.2

Table 3.2 The experimental conditions of this research

Experiment condition	Photocatalyst	UVA	MNBs
1	TZR	✓	✓
2	TZ	✓	✓
3	TR	✓	✓
4	ZR	✓	✓
5	TZR	✓	×
6	TZ	✓	×
7	TR	✓	×
8	ZR	✓	×
9	×	✓	×
10	×	✓	✓

❖ **Photocatalytic activities test**

1) The Photocatalytic activities test of the synthesized photocatalysts was assessed by evaluating the degradation efficiency of the target pollutants, which included two dyes, IC and RB5, each introduced at an initial concentration of 100 $mg.L^{-1}$ (100 ppm), along with the carbaryl pesticide at a higher concentration of 10 $mg.L^{-1}$ (10 ppm) due to its persistence in water treatment. The experimental setup consisted of the addition of 100 mL of dye-contaminated wastewater, containing 0.1 g of the photocatalyst, into a 250 mL Erlenmeyer flask. The photocatalytic process was initiated by exposing the photoreactor to UVA light (300 W, Osram) at a consistent intensity of 1,150 $\mu W.cm^{-1}$. To ensure uniform irradiation throughout the experiment, the light intensity within the photoreactor was measured using a UV light meter (UV-340 model).

2) Throughout the experiment, variations in dye concentration within the synthetic wastewater were monitored over a 120-minute reaction period. Treated wastewater samples were collected by filtering through a syringe filter at experimental times of 0, 15, 30, 45, 60, 90, and 120 minutes, respectively.

3) Samples were collected at regular time intervals and analyzed using a UV-Spectrophotometer Single Monochrome Type U-3900 to quantify the extent of dye degradation. The absorbance values were recorded to determine the photocatalytic efficiency of each experiment.

4) In addition to spectrophotometric analysis, gas chromatography-mass spectrometry (GC-MS; model GC 6890 N, Agilent) was employed to monitor and identify molecular structural changes in the dyes during the photooxidation process. This analysis helped detect intermediate product formation, which provided insights into the degradation pathways. The GC-MS system included an Agilent HP-5ms capillary column, an Agilent G1888 blank sampler, and an MSD 5973 N Ion Source EI Single Quint, which facilitated the precise identification of degradation byproducts.

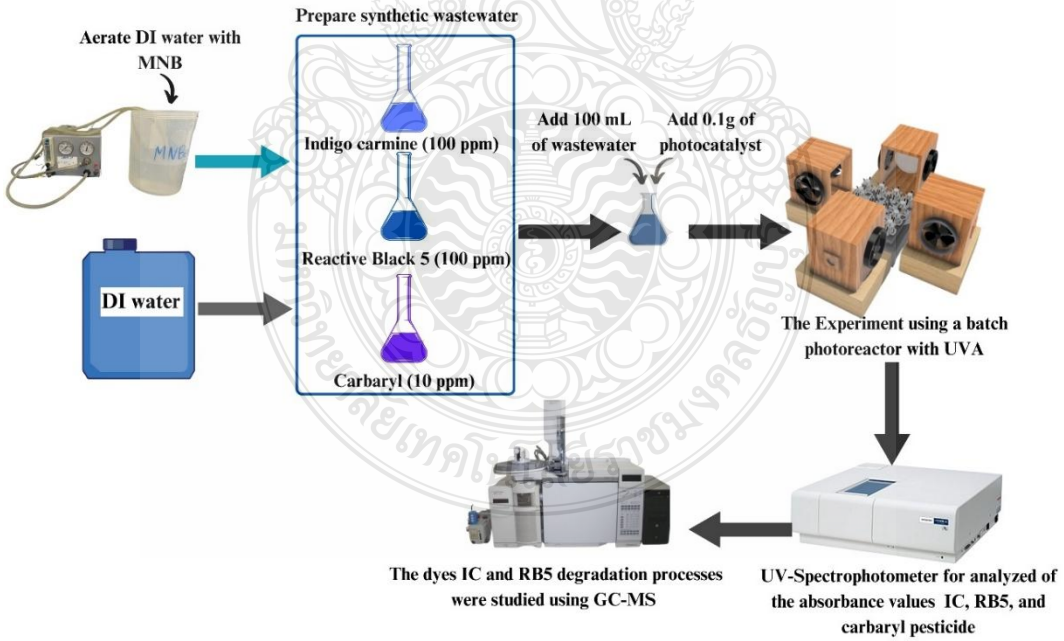

Figure 3.3 Assessment of photocatalytic activity

3.4 Photocatalytic reaction kinetics

The kinetics of contaminants in synthetic wastewater were studied using three types of pollutants, IC, RB5, and carbaryl, through a photocatalytic process with a photocatalyst. A first-order kinetic equation described the photocatalytic reaction mechanism and provided a suitable kinetic model.

CHAPTER 4
RESULTS AND DISCUSSION

4.1 Physical properties of photocatalyst

This chapter details the findings on the photocatalyst's physical properties, utilizing XRD, FT-IR, XPS, BET, SEM/EDS, TEM, PL, and UV-Vis/DRS techniques to thoroughly understand its structural, chemical, morphological, and optical attributes.

4.1.1 XRD results

Figure 4.1 shows the X-ray diffraction (XRD) patterns that reveal the crystal structures of four photocatalysts: TZ, TR, ZR, and TZR. The XRD analysis identifies distinct peaks corresponding to the crystallographic planes of ZnO and TiO_2, showcasing their structural characteristics. The TiO_2 anatase phase (JCPDS#21-1272) and ZnO (JCPDS#89-1379) references accurately correlate the peak intensities with the diffraction angles.

The TZ sample (green curve) XRD pattern shows its crystalline structure. Diffraction peaks of TiO_2 and ZnO indicate that the TZ sample is a composite material with these two phases. The TiO_2 peaks are located at certain crystallographic planes (101, 004, 200, 105, and 204), matching the anatase phase reference pattern (JCPDS# 21-1272) [59]. Peaks corresponding to planes (100), (002), (101), (102), (110), (103), (200), and (112) coincide with JCPDS# 89-1397, proving ZnO existence [60].

The TR sample (black curve) exhibits peaks matching the anatase phase of TiO_2 (JCPDS#21-1272), with diffraction peaks at 2θ values corresponding to the (101), (004), (200), (105), and (204) planes [61]. The absence of distinct RGO peaks, similar to ZR, indicates minimal or amorphous RGO presence. The TZ pattern (green curve) reveals characteristic peaks for ZnO and TiO_2 [61], demonstrating their coexistence in the composite. The absence of RGO peaks suggests a low concentration or amorphous nature, typical in such nanocomposites.

The XRD pattern of the ZR sample (blue curve) displays distinct peaks aligning with the standard ZnO diffraction pattern (JCPDS#89-1379). Peaks at 2θ values corresponding to the (100), (002), (101), (102), (110), (103), (200), and (112) planes indicate high crystallinity and purity of ZnO in the nanocomposite [62]. The absence of

notable RGO peaks suggests either an amorphous structure of RGO or a concentration below the XRD detection limit.

The XRD pattern of the TZR sample confirms the presence of both TiO_2 and ZnO crystalline phases, as evidenced by distinct peaks at specific 2θ values. The peaks at 25.3°, 37.8°, 48.0°, 53.9°, and 55.1° correspond to the (101), (004), (200), (105), and (204) planes of the anatase phase of TiO_2 (JCPDS#21-1272). Additionally, peaks observed at 31.8°, 34.4°, 36.3°, 47.5°, 56.6°, 62.8°, 66.3°, and 68.0° correspond to the (100), (002), (101), (102), (110), (103), (200), and (112) planes of ZnO (JCPDS#89-1379) [59]. This comprehensive peak analysis confirms the effective integration of ZnO within the TZR nanocomposite, highlighting its potential for enhanced photocatalytic applications due to the synergistic effects of the two materials.

In conclusion, XRD analysis confirms the successful synthesis of the four photocatalysts, displaying the expected crystalline phases of TiO_2 and ZnO [60]. The observed diffraction peaks align with the characteristic planes of both materials, indicating their effective integration within the composites. Notably, the absence of significant RGO peaks across all samples suggests a low concentration or amorphous state of RGO, expected in nanocomposites where the RGO crystalline phase is not predominant [63].

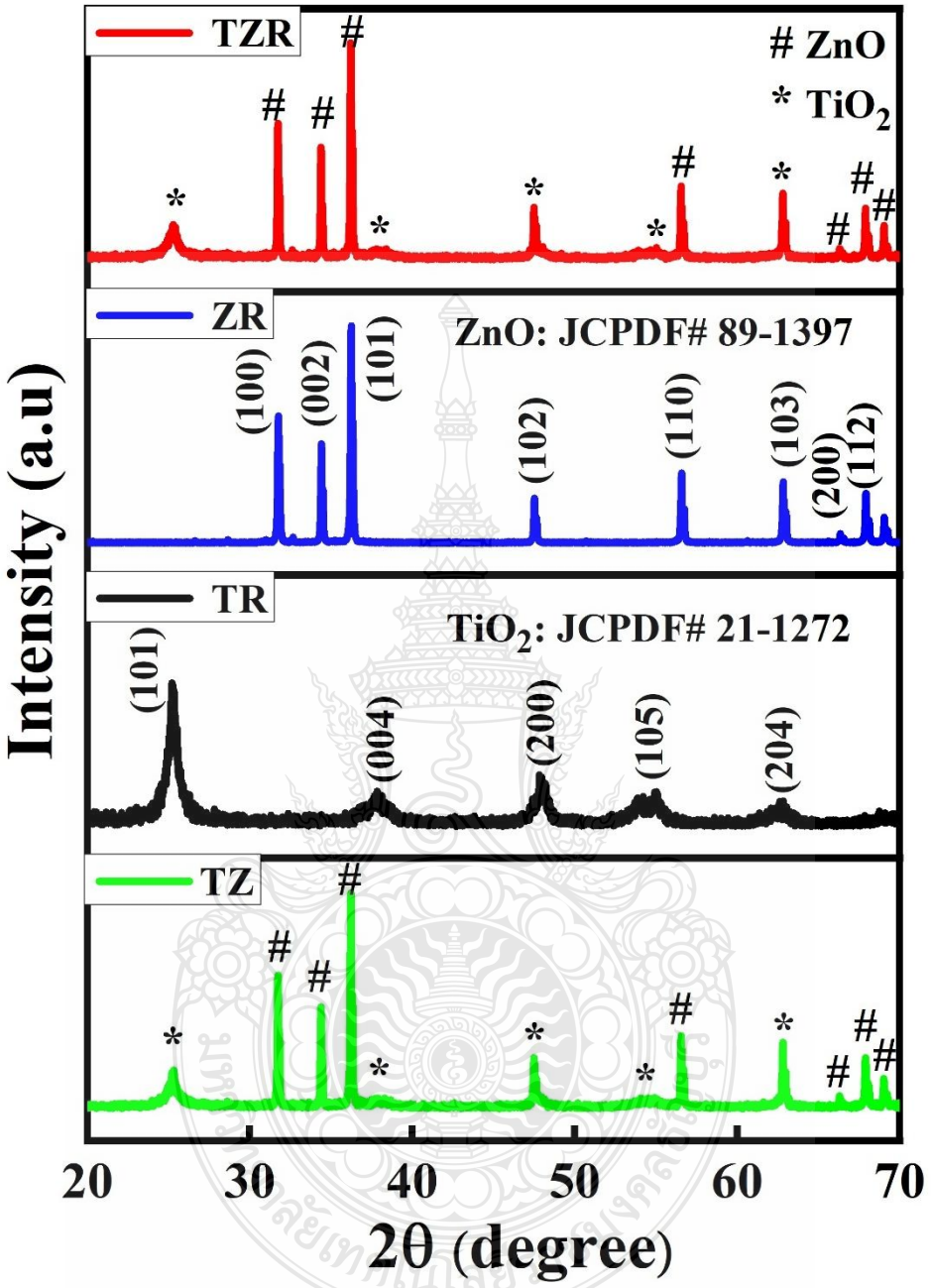

Figure 4.1 X-ray diffraction (XRD) patterns of photocatalysts

4.1.2 FTIR results

The FTIR spectra of TZ, TR, ZR, and TZR display unique absorption bands, which offer valuable information about their chemical structures and the interactions between their components, as shown in Figure 4.2.

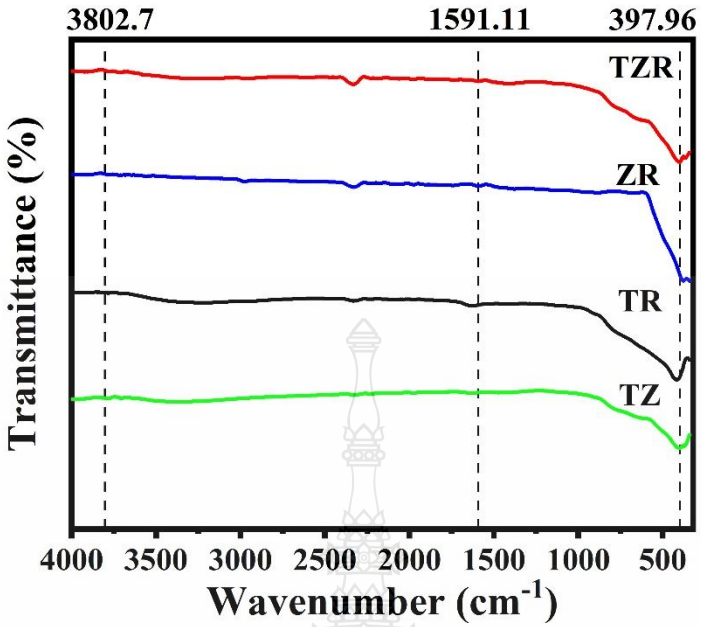

Figure 4.2 The FTIR spectra of (a) TZ, (b) TR, (c) ZR, and (d) TZR.

Figure 4.2, the FTIR spectra of several samples (TZ, TR, ZR, TZR) indicated distinctive absorption bands at 3802.7 cm^{-1}, 1591.11 cm^{-1}, and 397.96 cm^{-1}. The presence of large absorption bands at 3802.7 cm^{-1} and 397.96 cm^{-1} points to the presence of hydroxyl groups or adsorbed water, as well as the metal-oxygen stretching vibrations of Ti-O and Zn-O [64], verifying the presence of these components in all of the samples. The existence of RGO is confirmed by a unique peak at 1,591.11 cm^{-1} in samples obtained from TR, ZR, and TZR [64]. According to the findings of the investigation, TiO_2, ZnO, and RGO are all essential components of the nanocomposites that were investigated, as shown in Table 4.1

Table 4.1 Functional Group from FTIR Spectra.

Wavenumber (cm^{-1})	Functional Group
3,802.70	(O-H Stretching)
1,591.11	(C=C Stretching)
397.96	(Ti-O and Zn-O Stretching)

4.1.3 XPS results

X-ray photoelectron spectroscopy (XPS) allows one to investigate a material's oxidation states and surface chemical composition. XPS allows one to examine the elemental makeup and surface composition. For instance, the survey scan XPS spectrum of the TZR nanocomposite (Figure. 4.3 (a) exhibits distinct peaks corresponding to Zn 2p, Ti 2p, O 1s, and C 1s, confirmed the incorporation of titanium, zinc, oxygen, and carbon within the composite, displayed high-resolution spectra for every element in the XPS spectra, and showed Zn 2p, O 1s, Ti 2p, and C 1s on the surface of the nanocomposites [65].

These findings are consistent with previous studies, highlighting the reliability of the XPS results obtained for the TZR nanocomposites; XPS is a well-established method for characterizing solid-state materials, offering valuable information on elemental composition, chemical states, and surface properties. By analyzing the XPS spectra of Ti, Zn, O, and C in the nanocomposites, researchers can gain insights into the materials' surface chemistry and structural characteristics, which are crucial for optimizing their properties and performance [65].

X-ray photoelectron spectroscopy (XPS) revealed Zn, Ti, O, and C on the surface of the materials. The Zn 2p spectrum exhibited two spin-orbit coupling peaks, one at 1022.05 eV for Zn $2p_{3/2}$ and the other at 1045.01 eV for Zn $2p_{1/2}$, confirming the presence of ZnO and TiO_2 with two coupling peaks, 458.80 eV (Ti $2p_{3/2}$) and 464.50 eV (Ti $2p_{1/2}$), while O 1s had three coupling peaks. The signal at 529.80 eV indicated the presence of oxygen in the TiO_2 lattice. In comparison, the coupling peak at 531.60 eV stated the presence of surface defects, such as oxygen vacancies or titanium-bound hydroxyl groups. The C 1s spectrum consists of three peaks. The C-C bonds spike at 284.60 eV due to coincident carbon. The C-O spike at 286.40 eV, while the O=C-O

spike at 288.80 eV [66]. XPS analysis revealed defects on the surface of ZnO and TiO_2 and carbon-containing molecules. The oxygen–surface O-H interactions and the carbon peaks may indicate the functionalities of organic compounds on the altered or contaminated surfaces. As shown in Figure 4.3.

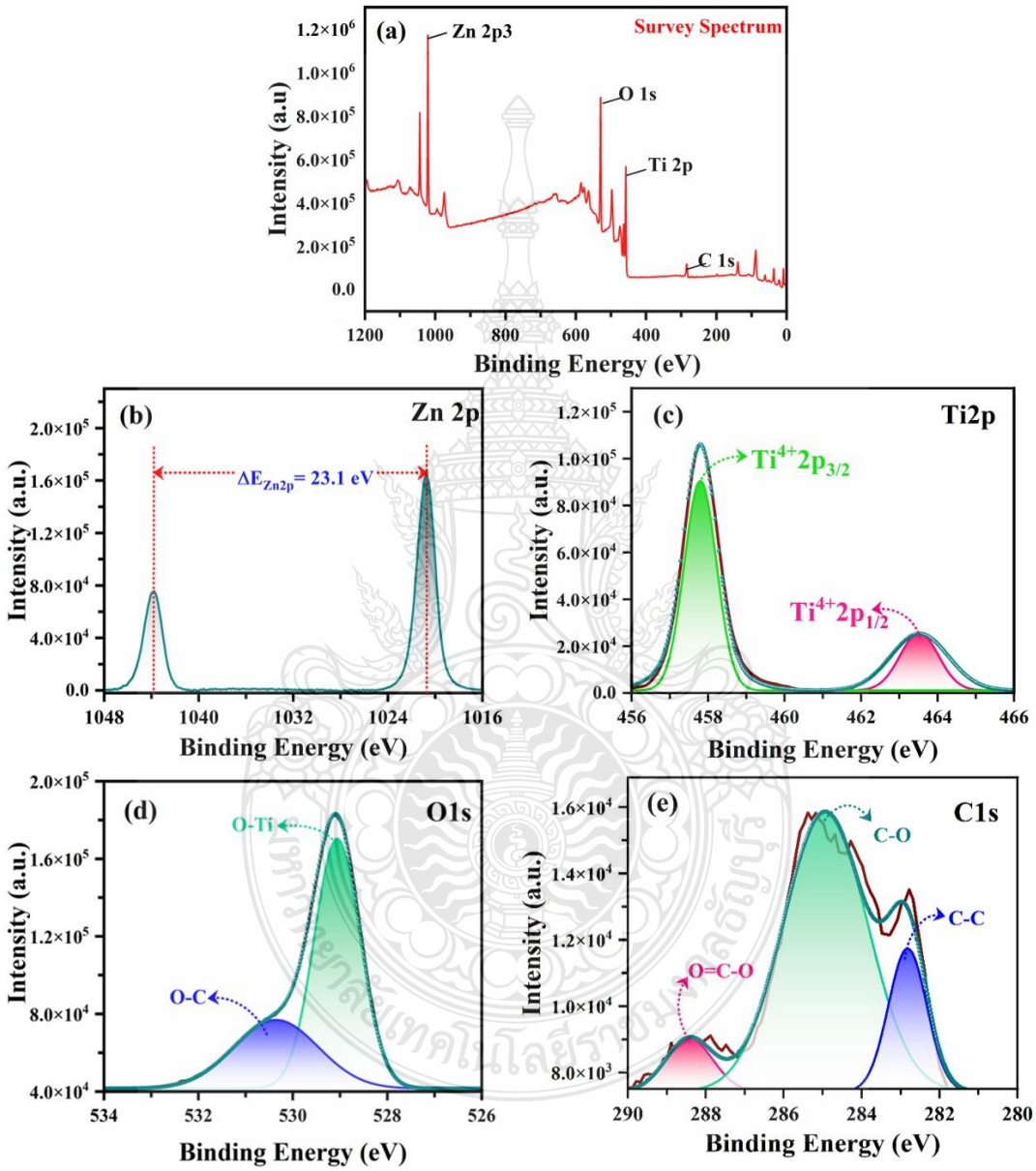

Figure 4.3 The XPS spectra of TZR: (a) fully scanned image, (b) spectra of Zn2p, (c) Ti2p, (d) O1s, and (e) C1s

4.1.4 BET results

TZR nanocomposite surface area BET analysis was done at 77 K using nitrogen adsorption isotherms. Due to its construction, the TZR composite increases specific surface area by absorbing more nitrogen than its components. The TZR nanocomposite has a particular surface area of 69.522 $m^2.g^{-1}$, and this value exceeds that of the individual components, demonstrating that TiO_2, ZnO, and RGO form a more complex structure that improves active site accessibility. A larger specific surface area in photocatalysis allows more interaction between the photocatalyst and reactants, boosting reaction efficiency. The TZR composite has a pore volume of 0.1264 $cm^3.g^{-1}$ and an average pore diameter of 7.2740 nm. These findings show that the composite is mostly mesopores, which let reactants and products diffuse during photocatalysis. Mesopores accelerate mass transfer to photocatalyst-active locations. TiO_2, ZnO, and RGO increase surface area and porosity, creating more photocatalytic active sites. This synergistic impact boosts reactant adsorption and photocatalytic efficacy. Such composites degrade contaminants better than their components under UV and solar light, as shown in Figure 4.4.

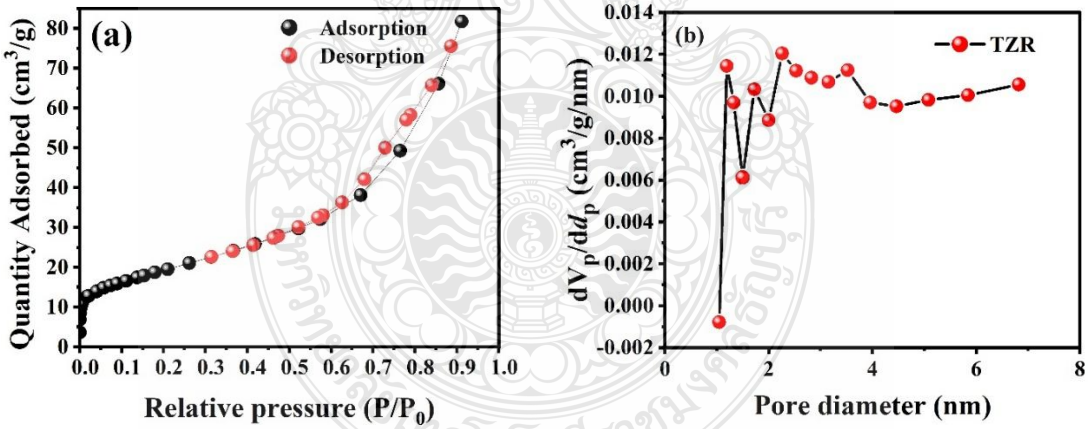

Figure 4.4 BET surface area measurements of TZR

4.1.5 SEM/EDS results

Analyzing the TZR nanocomposite using SEM and examining the SEM micrographs allows for valuable observations regarding the surface morphology of the synthesized TZR nanocomposite and its components:

The SEM study of the TZR nanocomposite made using the hydrothermal method shows important shape features that improve its photocatalytic abilities. Figure 4.5 (a, b) presents the TZR nanocomposite at 10,000x magnification, showing a porous and agglomerated structure. This shape is typical for nanocomposites made by heating them together, where ZnO, TiO_2, and RGO cluster together tightly. The high surface area due to porosity increases the number of active sites for photocatalytic reactions, enhancing performance. Also, how the particles stick together suggests that ZnO, TiO_2, and RGO have solid interactions at the interfaces. These interactions improve the charge transfer efficiency and lower the chance of electron-hole recombination, which is important for photocatalysis.

Figure 4.5 (c) presents such high-resolution energy dispersive EDS, which confirms the elemental composition of the TZR nanocomposite. It identifies the presence of carbon, oxygen, titanium, and zinc at atomic percentages of 16.65%, 28.54%, 36.84%, and 17.97%, respectively, with titanium being the most abundant.

Oxygen and carbon's major atomic percentage compositions emphasize their structural significance in the nanocomposite. However, titanium and zinc have higher atomic masses, which explains their more significant weight percentage discrepancies. This comprehensive elemental analysis supports the material's classification as a TZR nanocomposite photocatalyst, in which the synergistic interaction of the various components significantly improves the photocatalytic characteristics, as shown in Table 4.2.

Table 4.2 Elemental composition by weight of TZR

Element	Wt. %	Atomic %
C	16.65	32.89
O	28.54	42.33
Ti	36.84	18.25
Zn	17.97	6.52
Total	100	100

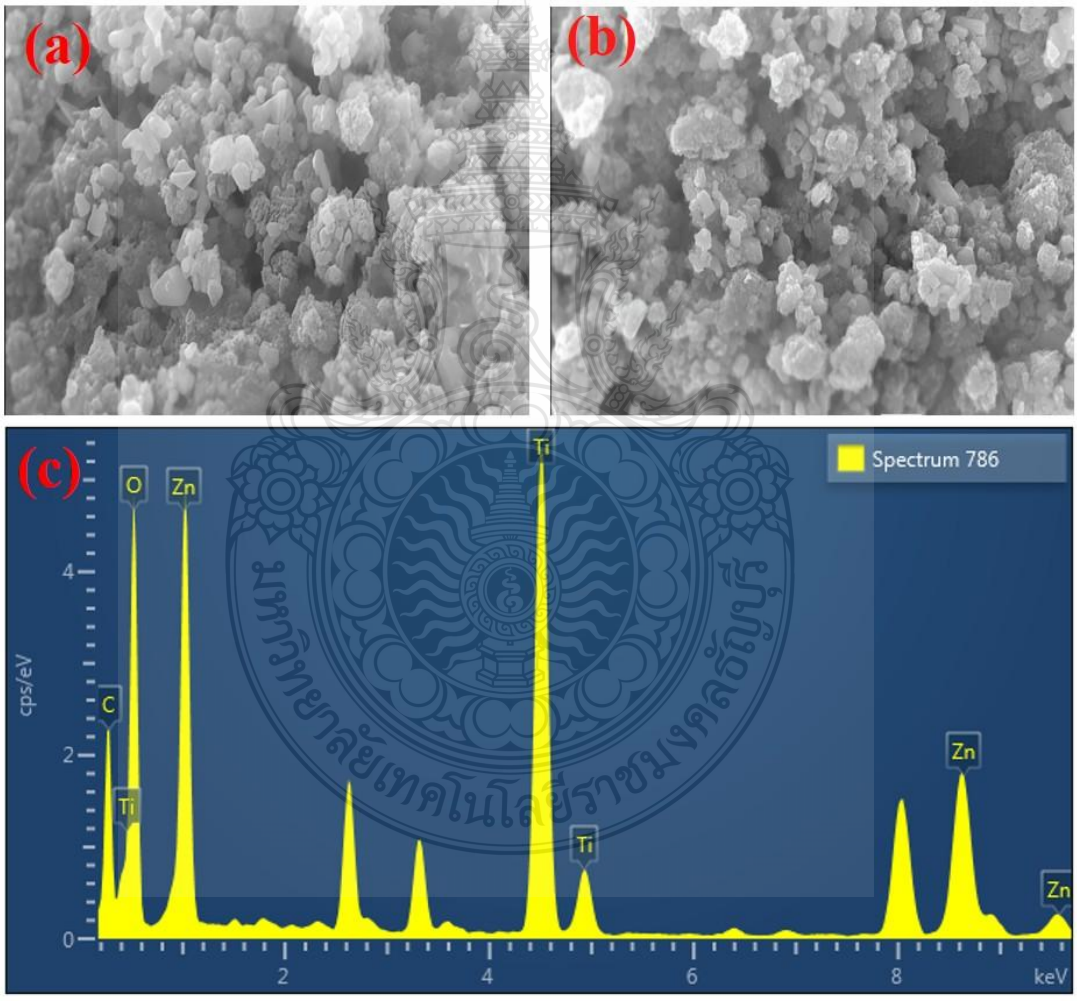

Figure 4.5 SEM images for (a, b) TZR and (c) EDS spectrum of TZR

As a result of the SEM analysis, the TZR nanocomposite has a structure that is both porous and aggregated, with TiO_2 and ZnO parts having different shapes. Just like a physical chemist, the porosity of the material and the unique granular TiO_2 and rod-like ZnO structures make it useful for many photocatalytic and sensor-related uses. These include improved light absorption, enhanced charge transport, and increased material stability. In addition, the EDS spectrum confirms that ZnO, TiO_2, and RGO have been successfully incorporated into the composite. This further validates the integrity and purity of the synthesized material. The TiO_2-ZnO-RGO nanocomposite has a unique mix of structural and compositional features that make it very promising for improving photocatalytic performance and making it easier to use in many different ways.

4.1.6 TEM result

The TEM analysis significantly illuminated the structural and morphological characteristics of the synthesized TZR nanocomposites at the nanoscale. As per the TEM observations, the nanocomposites were uniformly disseminated with TiO_2 and ZnO particles, with average particle diameters of approximately 5 nm and 10 nm. It's important to note that spherical agglomerations of TiO_2, ZnO, and RGO were seen. This suggests that a composite material was formed with a uniform distribution and strong interactions between the parts, especially between the RGO sheets and the TiO_2 and ZnO particles. Follow in Figure 4.6. (a).

ZnO particles were elongated, with an average size of 50 nm, whereas TiO_2 exhibited a spherical morphology, as revealed by additional analysis of the nanoparticles. Because the heterostructures are close to TiO_2 and ZnO particles, these semiconductor materials may work better together in the nanocomposites. Follow in Figure 4.6. (b).

Figure 4.6. (c) Crystalline TiO_2 and ZnO phases in the composite were confirmed by clear diffraction spots in the Selected Area Electron Diffraction (SAED) patterns. This shows that the composite still had distinct crystalline phases. Nanoscale, randomly arranged TiO_2 and ZnO particles were evenly spread out in the RGO matrix. This was demonstrated by the clear diffraction rings, which emphasized the material's polycrystalline nature. TiO_2 and ZnO are considered separate nanocrystals embedded in the RGO matrix rather than a solid solution since no rings or patches overlap. The goal of this structure design is to take advantage of the photocatalytic properties of TiO_2 and ZnO, as well

as the fact that RGO makes the structure more stable and increases its surface area and electron transport.

The TEM analysis of the synthesized TZR nanocomposites provides compelling evidence of their highly dispersed and uniformly distributed nanoscale structure, which is vital for advanced applications such as photocatalysis and energy storage. The TEM images reveal a transparent, sheet-like morphology of the RGO component, indicating the successful formation of few-layered RGO thin films. This morphology is consistent with previous findings of core-shell heterostructures, where a ZnO core, TiO_2 shell, and RGO sheets synergistically extend absorption into the visible light spectrum.

The TEM results confirm the unique structure and morphology of the TZR nanocomposites, emphasizing the potential for enhanced performance across various applications. The well-dispersed TiO_2, ZnO, and RGO particles, along with their interactions within the nanocomposites, provide critical insights into the composite material's behavior, underscoring the importance of nanoscale analysis for further characterization and application studies.

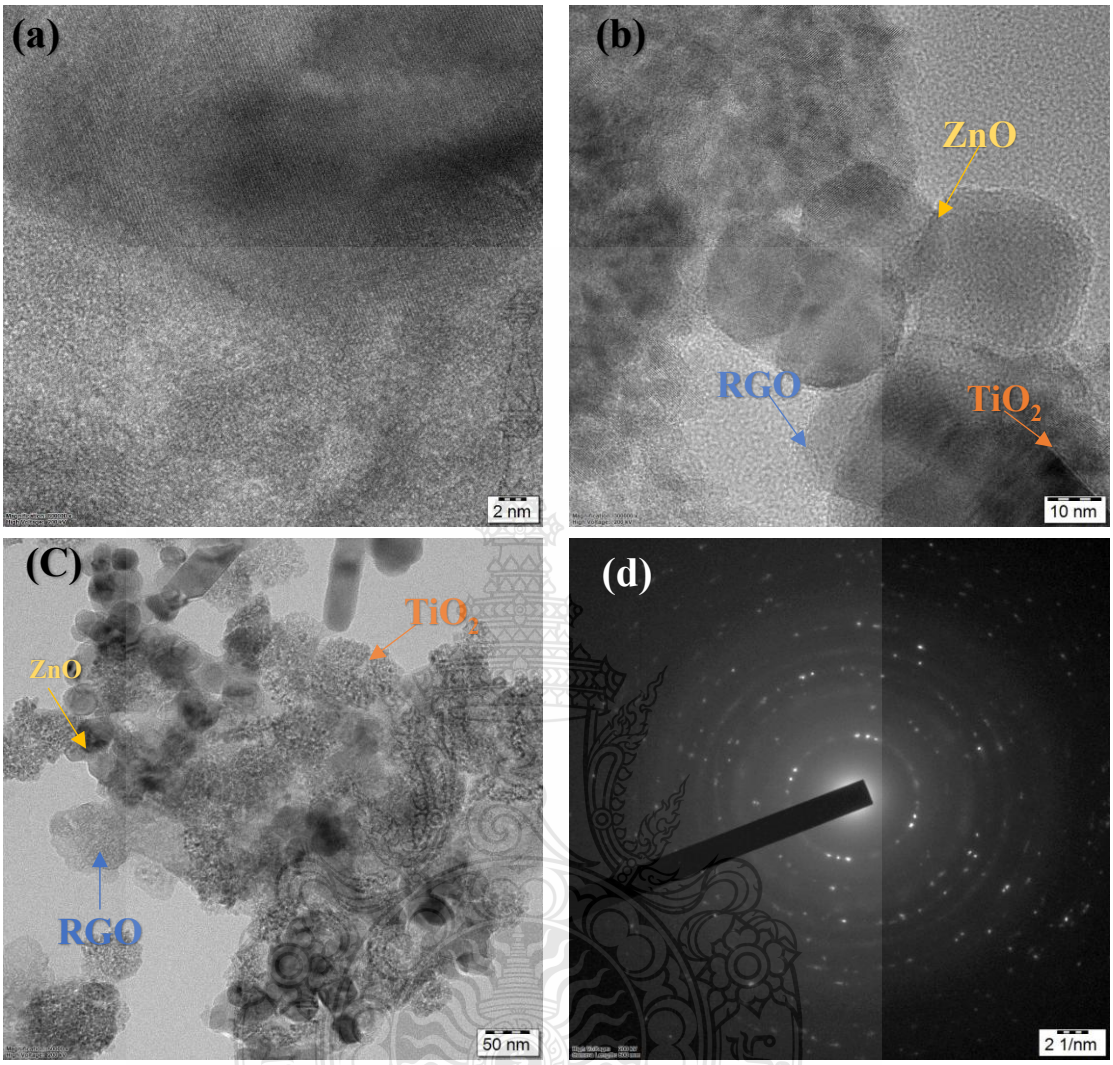

Figure 4.6 TEM image of TZR photocatalyst.

4.1.7 UV-Vis-DRS analysis

The UV-Vis-DRS and optical bandgap analysis of the as-prepared nanocomposite samples provide critical insights into their optical properties and potential applications. The UV-Vis absorption spectra reveal distinct absorption peaks for the four samples in Figure 4.7 (a), with TZ, TR, ZR, and TZR exhibiting peaks at 402.43 nm, 458.58 nm, 450.12 nm, and 477.75 nm, respectively [65], all within the UV region. These peaks are notably closer to the absorption edge, suggesting variations in the bandgap energy of the synthesized nanocomposites. Such shifts indicate changes in the electronic structure and can significantly influence the material's optical and electronic applications. The Tauc plot

method, utilized to estimate the optical bandgap (Eg), further supports these findings by providing a quantitative measure of the bandgap energies, which are crucial for understanding the semiconducting behavior of these materials, as shown in Figure 4.7 (a).

The Tauc plot is a graphical approach to estimating semiconductors or insulators' optical band gap (Eg). The following equation serves as the foundation for this technique, which is as follows [65]:

$$(\alpha hv)^n = A(hv - E_g) \quad (4.1)$$

Where:

α = the absorption coefficient

hv = the photon energy

A = a constant

Eg = The band gap energy

n = depends on the type of electronic transition (direct allowed, indirect allowed), For indirect allowed transitions, $n = 2$, and for direct allowed transitions, $n = 1/2$

Figure. 4.7 (b) shows the UV-DRS analysis shows that the bandgap energies of TZ, TR, ZR, and TZR nanocomposites vary greatly, with values of 3.10, 3.07, 3.03, and 2.93 eV, respectively, on their Tauc curves. These changes suggest that adding ZnO and RGO to TiO_2 matrices changes the electronic structure in a big way. This creates oxygen vacancies inside the nanocrystals, which makes it easier for charges to move around [65]. It is important to note that the TZR-reduced bandgap indicates improved electron interaction and enhanced light absorption, which is beneficial for photocatalytic efficiency. The tunable bandgap energy and the effective shift in the absorption edge make these nanocomposites very promising for advanced photocatalytic uses; the photocatalytic properties of TiO_2 and ZnO, along with the excellent conductivity and biocompatibility of RGO, make these nanocomposites the best for a wide range of uses in the photocatalytic process.

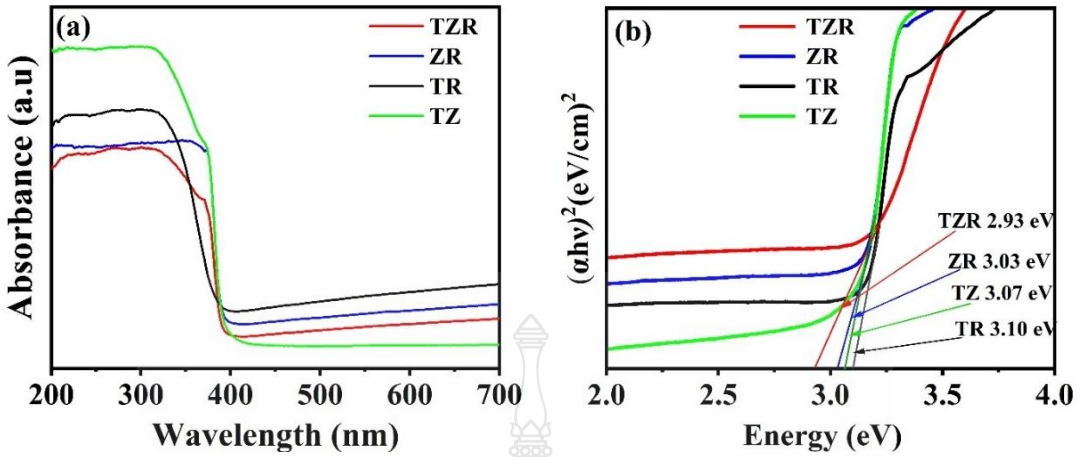

Figure 4.7 (a) UV-vis diffuse reflectance spectra of various samples and (b) the plot of Tauc versus light energy.

4.1.8 PL Spectroscopy

The photoluminescence (PL) spectra were employed to investigate the dynamics of photogenerated electron-hole pairs in the TR, ZR, and TZR samples. The spectra provide essential insights into carrier dynamics, encompassing trapping, migration, and interfacial charge transfer, all of which are critical for enhancing photocatalytic performance. Figure 4.8 illustrates that the photoluminescence (PL) spectra of TR, ZR, and TZR NCs exhibit an emission peak around 625 nm, indicative of the recombination of photogenerated electron-hole pairs [67]. The PL intensity offers valuable information regarding the recombination rate, with a lower intensity suggesting better charge separation and enhanced photocatalytic performance. Among the samples, TZR exhibits the lowest PL intensity, indicating that the integration of reduced graphene oxide (rGO) effectively mitigates electron-hole recombination by promoting charge transfer. In comparison, TR and ZR NCs exhibit elevated PL intensities, suggesting a comparatively higher recombination rate, which could result in diminished photocatalytic efficiency. The maximum PL intensity noted in TR indicates that this composition exhibits the least efficient charge separation. The reduced PL intensity of TZR highlights its enhanced potential as a photocatalyst, attributed to the synergistic interaction among TiO_2, ZnO, and rGO. This interaction facilitates charge carrier dynamics and leads to improved photocatalytic performance in the degradation of dyes and pesticides [68].

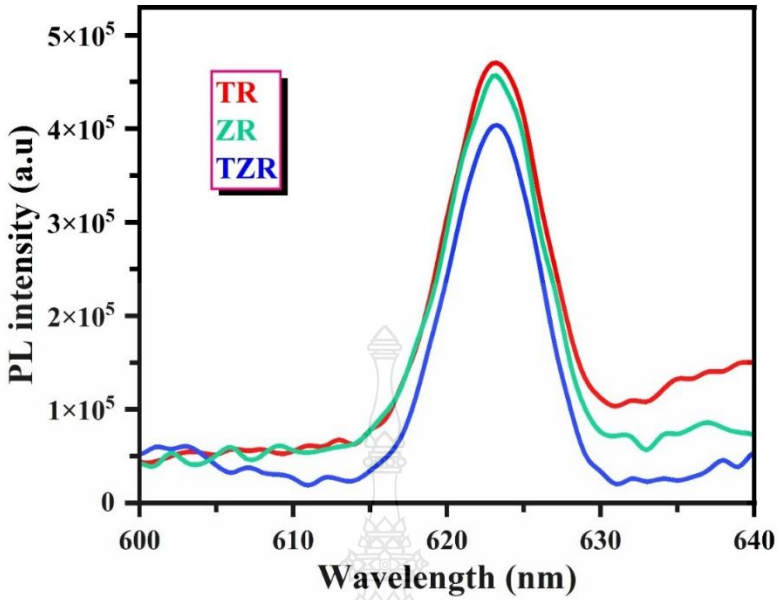

Figure 4.8 Photoluminescence spectra of TR, ZR, and TZR nanocomposites.

4.2 Photocatalytic degradation of organic pollutants in water

The two types of synthetic wastewater for IC, RB5 dyes, and carbaryl degradation were tested using photocatalytic processes with TZR, ZR, TR, and TZ photocatalysts, UVA light sources 1,250 $\mu W.cm^{-2}$, and MNB aeration: IC, RB5 dyes, and carbaryl. The concentrations were periodically measured at 0, 15, 30, 45, 60, 90, and 120 minutes. All of the experiment results are shown in Table 4.3.

MNB size distribution in the samples was evaluated using the Malvern Panalytical nano-sight, nano-tracking analysis (NTA). After the hydrodynamic principles were implemented to ascertain particle size, the Stokes-Einstein equation was implemented to evaluate these entities in the liquid phase. The presence of MNB in water. MNB were generated by circulating water in the RMUTT-MNB generator in this investigation. The average length of MNB spheres was 100 nm, ranging from 53 to 731 nm. Based on a physical investigation, the average bubble size of MNB was 102.1 ± 1.0 nm. Using air droplets of comparable size, this apparatus aerates MNB. The dissolved oxygen (DO) levels were proportionally elevated due to aeration by MNB. As a result, the average concentration of dissolved oxygen was 15.14 mg. L^{-1} after 15 minutes. Smaller MNB are preferred due to their stability and water duration, as shown in Figure 4.9.

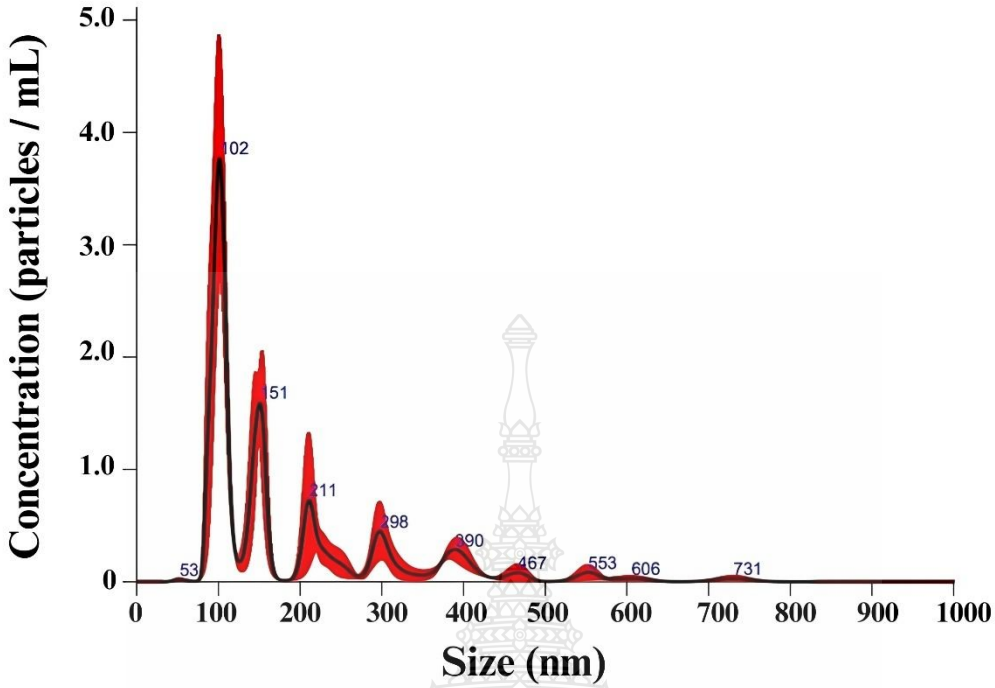

Figure 4.9 MNB concentration, particle size, and size distribution.

The results of the photocatalytic degradation of IC, RB5 dyes, and carbaryl were in experiment conditions 9 (UVA only) and 10 (UVA + MNB), and the degradation efficiency of the pollutants (IC, RB5, and Carbaryl) was >2%. These experimental conditions lacked a photocatalyst, which is crucial for initiating photocatalytic reactions. UVA light alone is insufficient to generate the reactive species, such as hydroxyl radicals, required to degrade the pollutants. While MNB are included in condition 10, their primary role is to enhance mass transfer, which does not directly contribute to generating reactive species without a catalyst. Thus, degradation under these conditions remains minimal.

Experiment conditions 6,7, and 8 (without MNB) showed up to 80% degradation, while conditions 2, 3, and 4 (with MNB) demonstrated degradation rates of >92%. The improvement in degradation under these conditions can be attributed to using photocatalysts (TZ, TR, ZR), which generate electron-hole pairs when exposed to UVA light. These pairs interact with H_2O and O_2 to form reactive oxygen species (ROS) like •OH that degrade the pollutants. However, the performance of experiment conditions 6-8 is limited by the availability of dissolved oxygen and the relatively lower mass transfer efficiency. However,

experiment conditions 2-4, although improved by MNB, are still restricted by the photocatalysts' ability to absorb UVA light and produce ROS.

Table 4.3 Degradation efficiency of synthetic wastewater with various contaminants

Experiment condition		Degradation efficiency (%)		
		IC	RB5	Carbaryl
1	TZR+ UVA+MNB	99.08	98.73	98.98
2	TZ+ UVA+MNB	92.28	79.32	92.68
3	TR+ UVA+MNB	78.23	40.06	77.02
4	ZR+ UVA+MNB	88.16	65.89	80.59
5	TZR+UVA	98.30	97.83	97.17
6	TZ+UVA	80.94	79.32	61.34
7	TR+UVA	64.47	23.58	43.34
8	ZR+UVA	59.53	44.03	71.75
9	UVA	1.00	1.00	0.59
10	UVA+MNB	2.00	1.00	1.00

In contrast, experiment conditions 1 (TZR + UVA + MNB) and 5 (TZR + UVA) exhibited near-complete degradation, with < 99% efficiencies. This high performance is likely due to using TZR, a composite photocatalyst that provides superior light absorption, charge separation, and ROS generation compared to individual photocatalysts. In experiment condition 1, adding MNB further enhances degradation by improving oxygen availability and mass transfer, resulting in more frequent interactions between pollutants and reactive species. Even without MNB, experiment condition 5 performed excellently, highlighting the superior photocatalytic properties of TZR over the other catalysts tested.

As shown in Figure 4.10, a controlled experiment with a specified set of experiments was performed to evaluate the efficiency of the three types of synthetic wastewater for IC, RB5 dyes, and carbaryl.

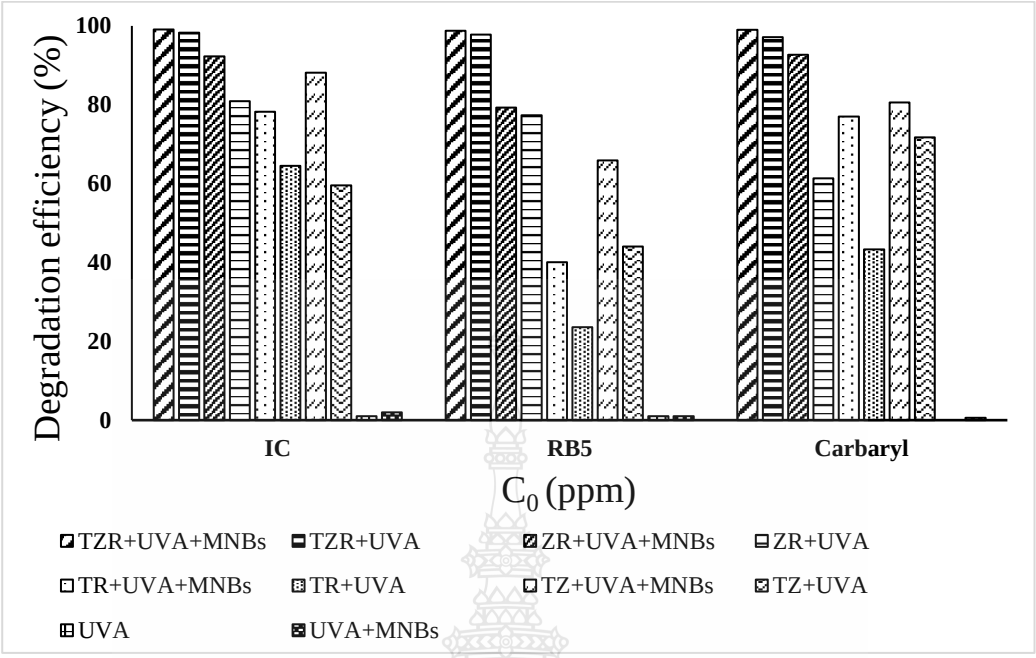

Figure 4.10 Comparison of degradation efficiency of synthetic wastewater under different experimental conditions and initial concentrations of various contaminants (C_0)

These results emphasize the significance of MNB in increasing photocatalytic activity by maintaining high levels of oxygen and ROS generation. This is consistent with previous studies that emphasize the role of nanobubbles in enhancing Oxygen transfer and photocatalytic efficiency. The study's results indicate that the effectiveness of the combination of TZR, UVA, and MNB for dye degradation depends on the dye concentration. Additionally, the photocatalytic degradations of MNB promote interaction between pollutants and photocatalysts due to their larger surface area. Droplets enhance the mixing and diffusion of pollutants toward the TZR catalyst. Higher mass transfer rates result in more exposure of pollutant molecules to the catalyst, therefore enhancing the breakdown process. MNB also boosts solution-dissolved oxygen. It is crucial because photocatalyst processes involving ambient oxygen can generate reactive oxygen species (ROS) such as •OH and $\bullet O_2^-$. ROS is essential for the degradation of organic pollutants into more benign molecules. Oxygen availability accelerates the degradation and production of reactive oxygen species (ROS). Matrix nanofibers enhance the interaction between contaminants and catalytic surfaces. The breakdown efficiency rises

as additional contaminating molecules adhere to the RGO surface. More pronounced reductions in IC dye, RB5 dye, and carbaryl absorption are observed with MNB, particularly after 60 minutes. Experiment condition 5 (TZR + UVA) evaluated the experiment's efficacy, excluding MNB. The photocatalytic degradation process of Condition 5 was less effective than that of Experiment condition 1, yet it nonetheless rapidly disintegrated pollutants. The reason why TiO_2 and ZnO are widely used as photocatalysts is their ability to absorb UVA light and generate electron-hole pairs. The valence band electrons in TiO_2 and ZnO transition to the conduction band and generate holes when exposed to UVA light. These electrons and holes produce ROS, which dissolve pollutants. This basic photocatalytic process effectively decreases contaminants for 120 minutes, as seen by the consistent decrease in absorbance, even in the absence of MNB. RGO enhances electron transport and decreases charge recombination, therefore enhancing the properties of TiO_2 and ZnO in experiment condition 5. Reduced graphene oxide's high conductivity displaces electrons from the photocatalyst, restricting hole recombination. However, a higher concentration of ROS leads to effective degradation at a slower rate compared to Condition 1. While the presence of MNB would enhance mass transfer and surface contact, their absence has resulted in a less significant decrease.

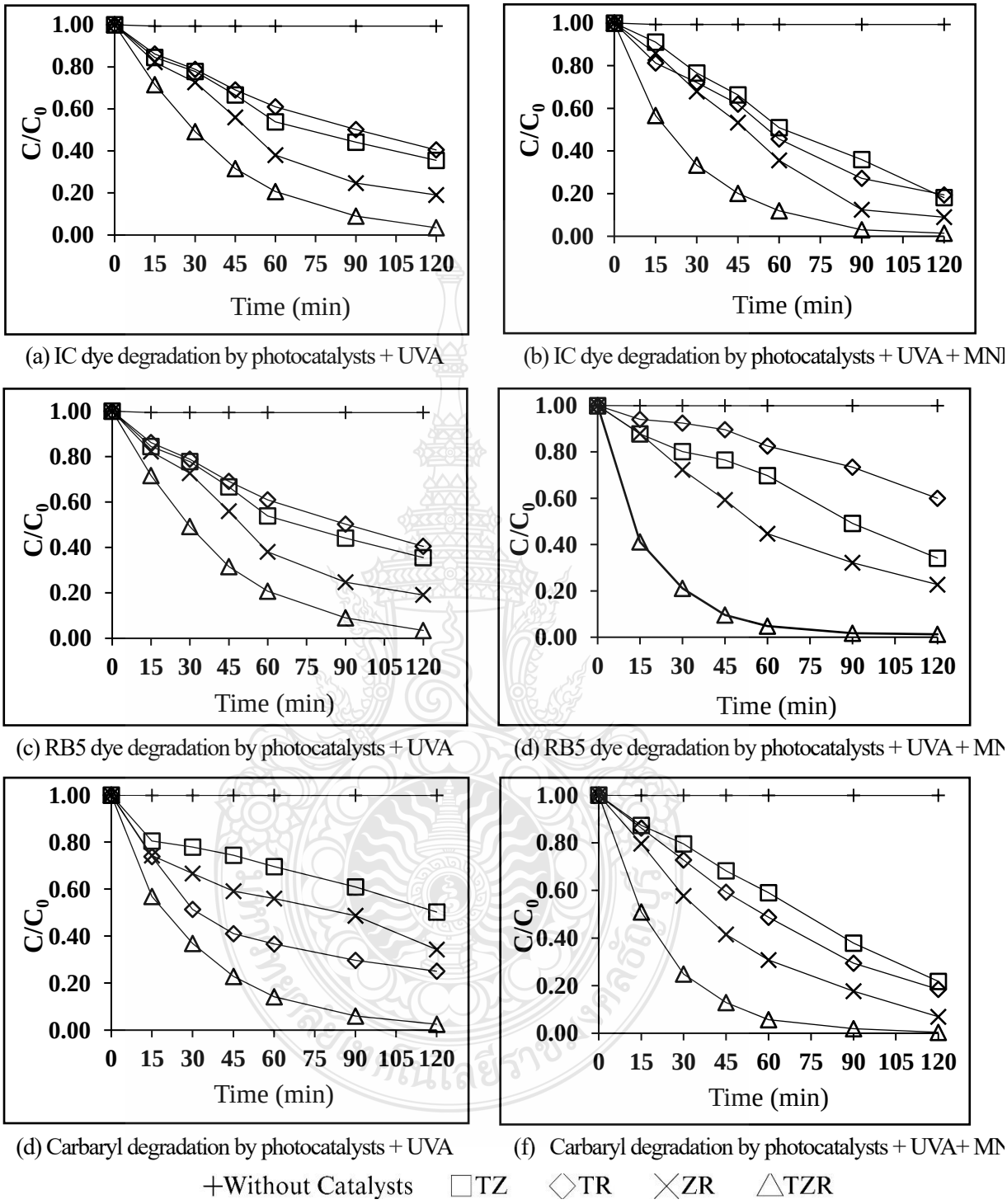

Figure 4.11 Photocatalytic degradation of dyes with MNB and without MNB.

This study focused on the photocatalytic degradation of dyes using a combination of TZR photocatalysts, UVA, and MNB, with particular attention to the crucial role MNB plays in the process. The research underscored that the continuous production and stability of smaller MNB were vital to sustaining high oxygen levels, significantly boosting the generation of the reactive oxygen species (ROS). These ROS are essential for efficiently degrading dyes, especially in wastewater treatment applications.

The findings of the dye treatment efficiency of IC and RB5 are presented in Figures 4.12 - 4.13. It was reported that the efficiency of the dye treatment effectiveness catalyst was assessed at different concentration levels and compared to the industrial drainage standard of 300 ADMI. The results show that only test condition 1 (TZR+UVA+MNB) can be degraded by IC and RB5 dyes, with maximum dye intensity measured at 72 and 102 ADMI. Experiment condition 5 (TZR+UVA) can remove high color. According to the wastewater standard, the highest reported values are 131 and 172 ADMI at a concentration of 100 ppm. The 2017 Card issued by the Ministry of Industry establishes factory wastewater management guidelines stipulating that the maximum allowable dye intensity discharged into public water sources should not exceed 300 ADMI.

The study examined the photocatalytic degradation of IC, RB5, and carbaryl synthetic wastewater under experiment conditions 1 (TZR + UVA + MNB) and 5 (TZR + UVA). The degradation efficiency was evaluated through UV-Vis's absorbance spectra over a 120-minute duration, revealing characteristic peaks at 610 nm for IC, 598 nm for RB5, and 220 nm for carbaryl. In experiment condition 5, absorbance consistently declined over time, signifying progressive degradation. After 120 minutes, the absorbance values remained significant, indicating incomplete degradation. Experiment condition 1, which included MNB, showed a more rapid decline in absorbance, especially after 60 minutes, indicating faster degradation due to the increased interaction between the pollutants and the catalyst surface, as shown in the Figure. 4.14.

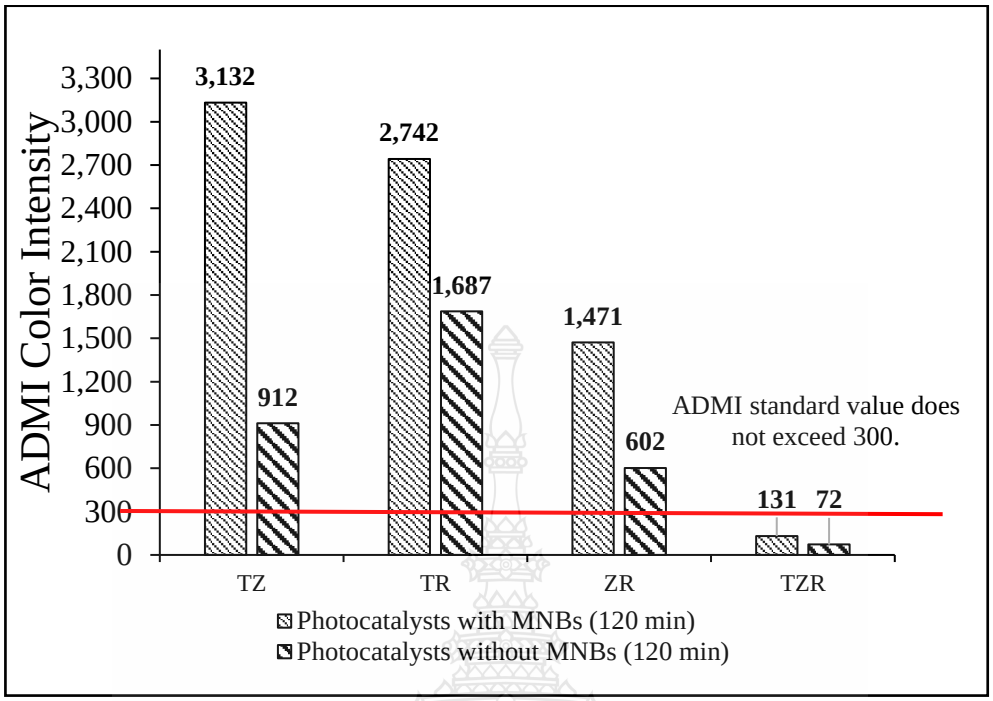

Figure 4.12 Comparison of IC dye concentration treated with photocatalytic process.

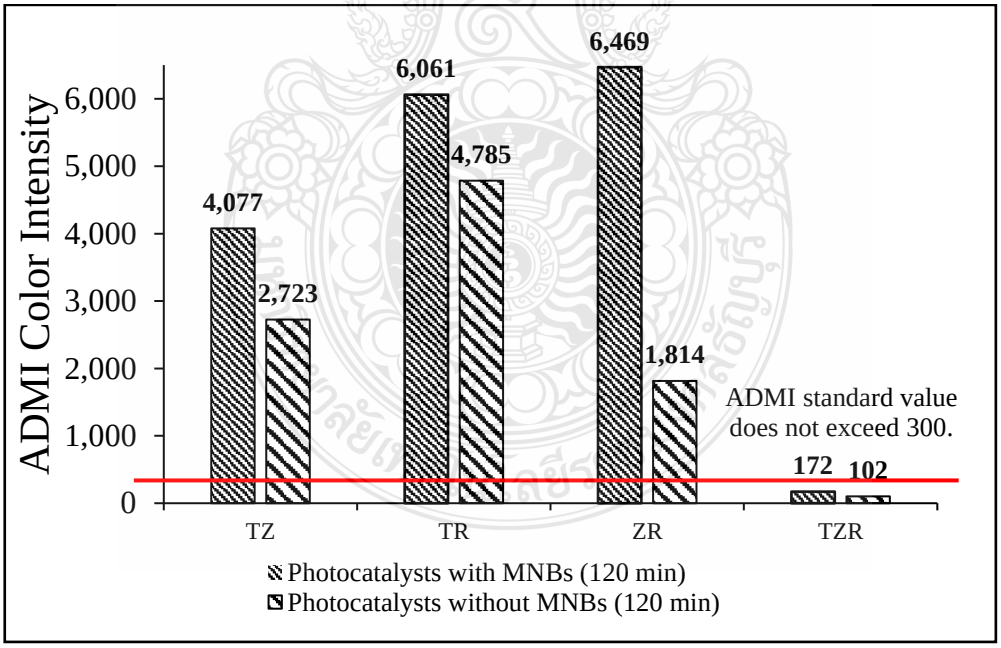

Figure 4.13 Comparison of RB5 dye concentration treated with photocatalytic process.

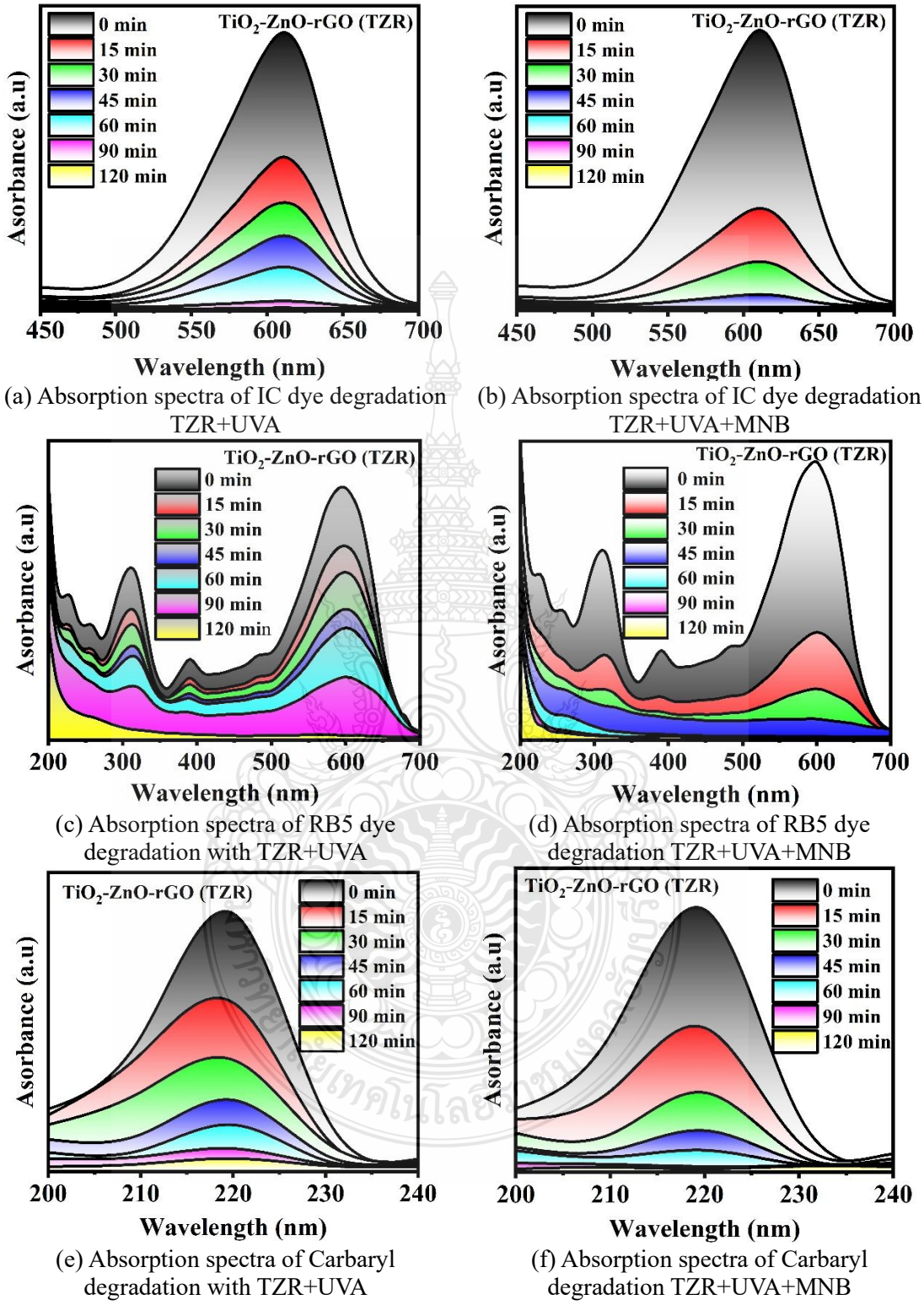

(a) Absorption spectra of IC dye degradation TZR+UVA

(b) Absorption spectra of IC dye degradation TZR+UVA+MNB

(c) Absorption spectra of RB5 dye degradation with TZR+UVA

(d) Absorption spectra of RB5 dye degradation TZR+UVA+MNB

(e) Absorption spectra of Carbaryl degradation with TZR+UVA

(f) Absorption spectra of Carbaryl degradation TZR+UVA+MNB

Figure 4.14 Absorption spectra of dyes and pesticides in TZR photocatalyst under UVA radiation with and without MNB

- **Dye structure transformation analysis**

GC-MS analysis of experiment condition 1 (TZR+UVA+MNB) demonstrated steady dye degradation of the IC dye over 120 min; the experiment demonstrated a gradual decomposition of the IC dye, resulting in various intermediates and degradation products. At 0 minutes, the complete Indigo Carmine structure is visible, showcasing its chromophore. As degradation advances, notable intermediates emerge at different retention times. For instance,3-carbomethoxy-2-methyl-5-oxo-4(3,5-trimethoxyphenyl)-1,4,5,6,7,8-hexahydropyrido[4,3-b] pyrimidine is observed at 15 minutes (m/z 396), likely arising from ring-opening and rearrangement processes. The complicated compound 33-methyl-2-propyl-3,4-dihydropyrido[4,3-b] quinoxalin-1-one that was seen at 30 min (m/z 285) suggests that there may be room for more changes to the structure. As the breakdown progresses, smaller degradation products such as 2-n-butyltetralin (m/z 216, at 45 min) and 1H-Indole, 4-methyl- (m/z 131, at 90 min) begin to appear. At 120 minutes, observe the intermediate degradation product, methylamine (m/z 31), which signifies the dye's complete breakdown. This steady degradation pattern draws attention to the intermediate complexity and eventual simplification of molecular fragments over time. It explains how the IC dye breaks down under these experimental conditions. As shown in Figure 4.15.

The GC-MS analysis of Reactive Black 5 (RB5) dye degradation in Experiment condition 1 (TZR + UVA + MNB) illustrates a progressive dye breakdown over 120 minutes. Initially, at 15 minutes, the degradation pathway reveals the presence of 2-(3-carbomethoxy-5-methoxy-7-methyl-2H-1,4-benzothiazin-2-yl)-5-methoxy-7-methyl-2H-1,4-benzothiazine-3-carboxylic acid methyl ester (m/z 500), indicating the initial fragmentation of RB5's azo bond and benzothiazine moieties. By 45 minutes, a simpler aromatic compound, 4-Methoxy-1,5-naphthylene Diacetate (m/z 274), is detected, reflecting the progressive breakdown of the dye's aromatic rings and the cleavage of sulfonate groups. This transition from complex heterocyclic structures to smaller aromatic esters highlights the oxidative process initiated by the TiO_2-ZnO-RGO photocatalyst, enhanced by MNB, which generates reactive oxygen species (ROS) under UVA light. as the degradation continues, between 60 to 120 minutes, smaller aliphatic compounds such as Hexanamine (m/z 101), 2-Methylbicyclo [4.4.0] decan-1-ol (m/z 168), and (2R)-2-

Isopropyl-5-methyl-hexan-1-ol (m/z 158) emerge, indicating the further oxidation and cleavage of the dye into simpler alcohols and amines. By the 120-minute mark, detecting low-molecular-weight products like formic acid (m/z 74) and 1,2-ethanediol (m/z 62) suggests the near-complete breakdown of RB5 into essential organic acids and diols. These results demonstrate that the TZR photocatalyst, combined with UVA and MNB, efficiently degrades RB5 into more minor, more oxidized compounds, leading toward partial mineralization. As shown in Figure 4.16.

In Experiment Condition 5 (TZR + UVA), the photodegradation of IC dye over 120 min demonstrates the effectiveness of the TZR photocatalyst, although the absence of MNB slows down the process. Early degradation products such as Ethyl 5-cyclohexyl-1-thia-4-thioxo-(4H)-3,5,6-triazaacanthylene-2-carboxylate (m/z 411) and 9,10-Dimethoxy-5,8,13,13a-tetrahydro-6H - [1,3] dioxolo[4,5-g] isoquino [3,2-a] isoquinoline 7-oxide (m/z 355) appear within 15–30 minutes, signaling the early oxidation of the dye's chromophore. Between 60 and 90 minutes, smaller intermediates like 7-Methyl-5,6-dihydrobenzo[c]acridine (m/z 245) and 4-Methoxy-N-methylbenzenamine (m/z 137) reflect further oxidation of aromatic rings and the formation of amine-based compounds. By 120 minutes, ethane (m/z 28) is detected, indicating partial mineralization, though the incomplete conversion to CO_2 and H_2O highlights that the degradation halts at intermediate stages. As shown in Figure 4.17.

For RB5 dyes, the degradation in Experiment Condition 5 also proceeds gradually over 120 minutes. Initially (0–15 minutes), large compounds like 1,2-Bis(2'-hydroxy-1,1'-binaphthyl-2-ylthio) ethane (m/z 630) suggest early fragmentation of RB5's azo bonds and aromatic rings. As the reaction progresses (30–120 minutes), smaller intermediates such as N-tert-Butyl-3-isopropyl-2-phenyl-3,4-dihydroquinazoline-4-carboxamide (m/z 349) and 5-Phenyl-2,4-hexadienal (m/z 172) emerge, indicating ongoing oxidation and breakdown into simpler nitrogenous and aldehyde compounds. By 120 minutes, compounds like 2(3H)-Furanone, 5-ethyl-dihydro- (m/z 114) point to advanced oxidation, though the absence of smaller organic acids like formic acid indicates incomplete mineralization.

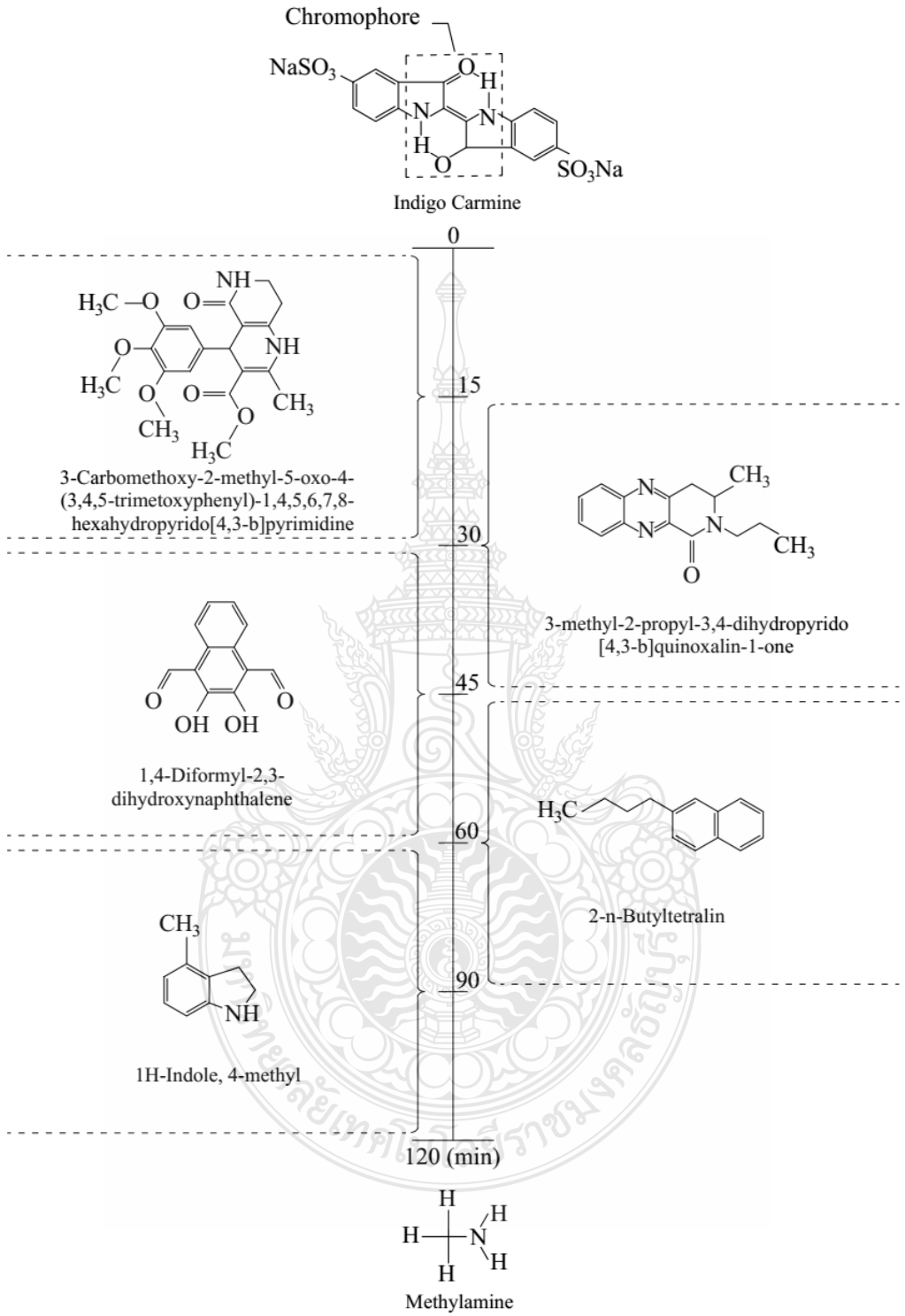

Figure 4.15 IC dye structure transformation for condition 1 (TZR+ UVA+MNB)

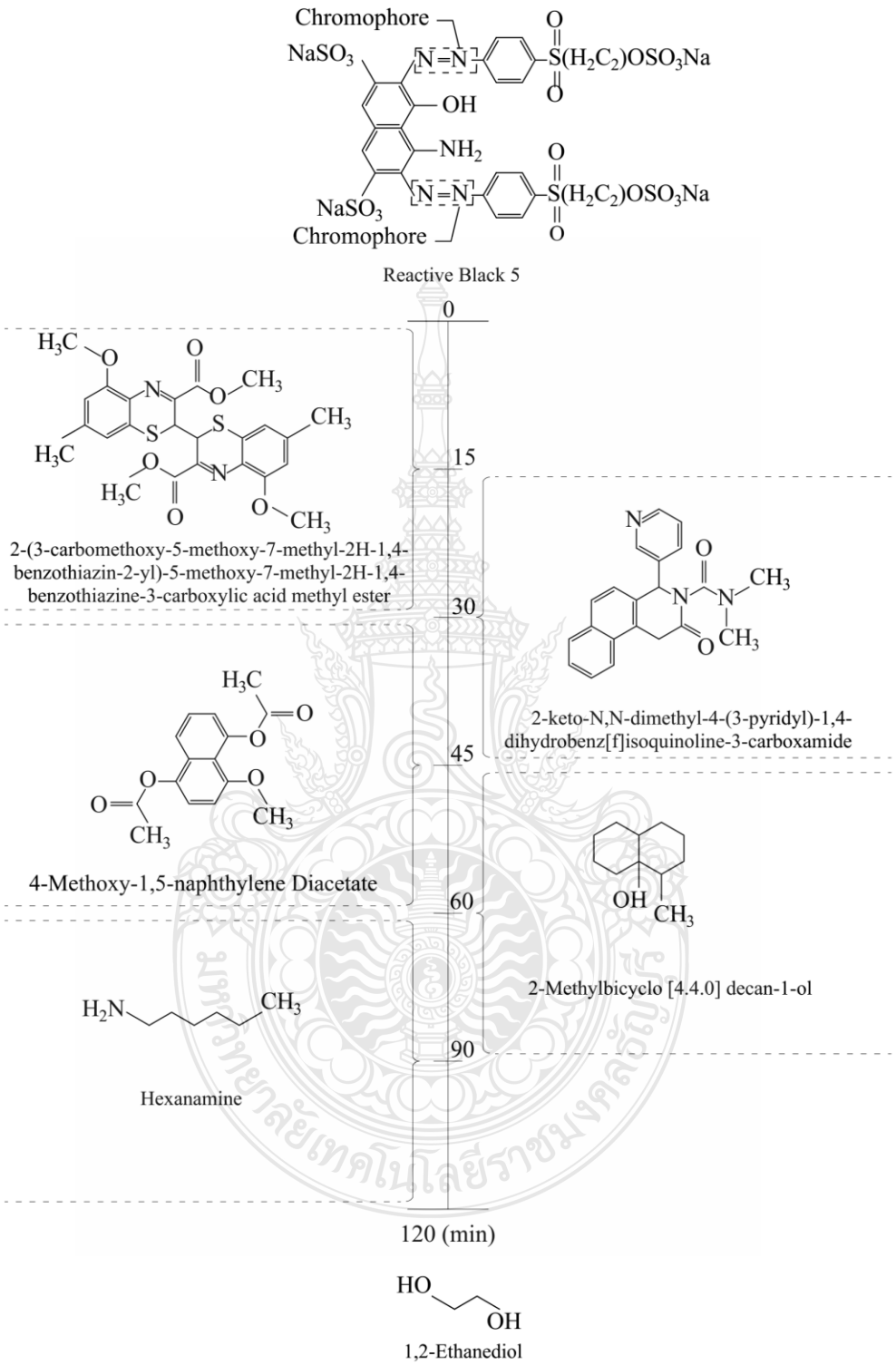

Figure 4.16 RB5 dye structure transformation for condition 1 (TZR+ UVA+MNB)

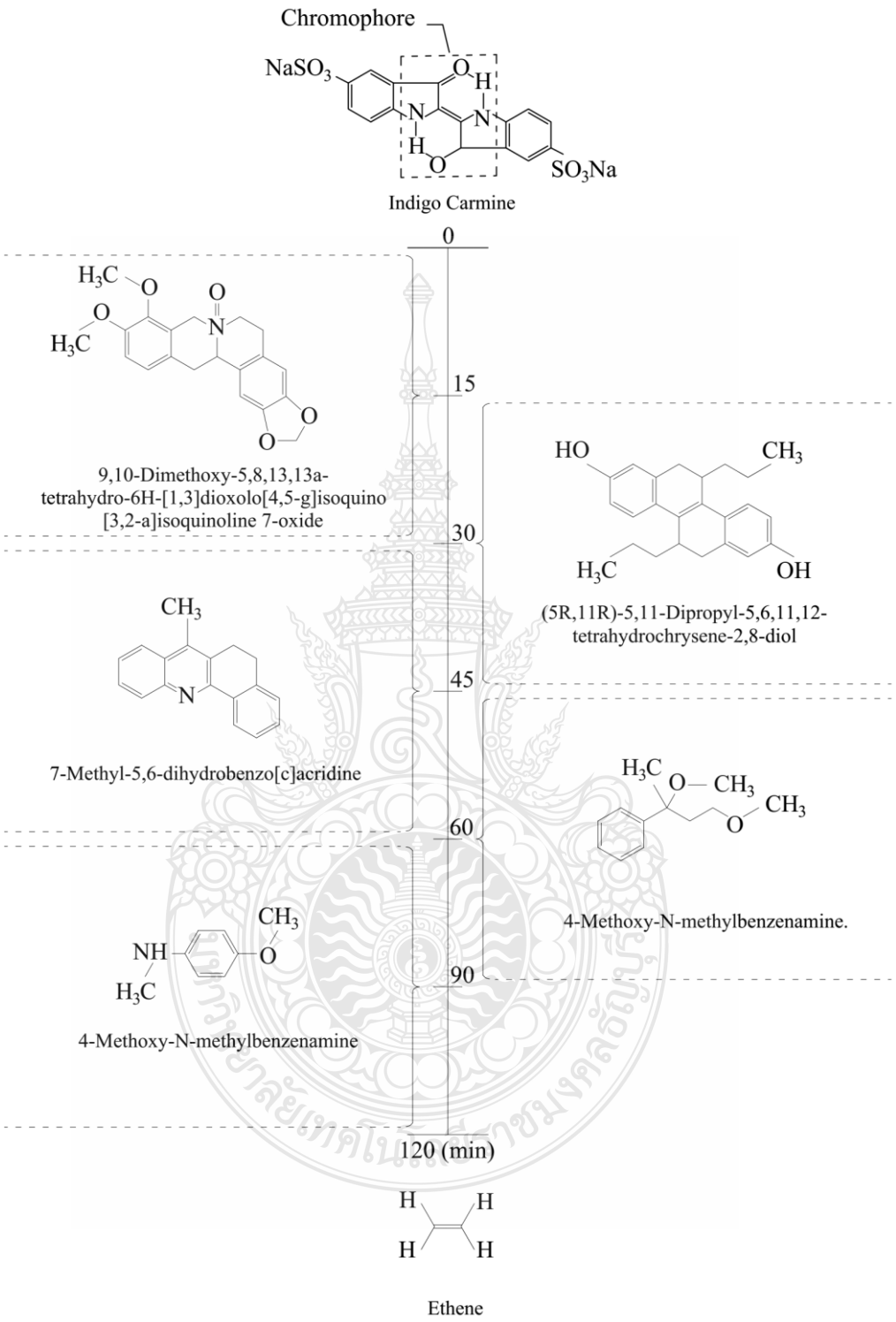

Figure 4.17 IC dye structure transformation for condition 5 (TZR+ UVA)

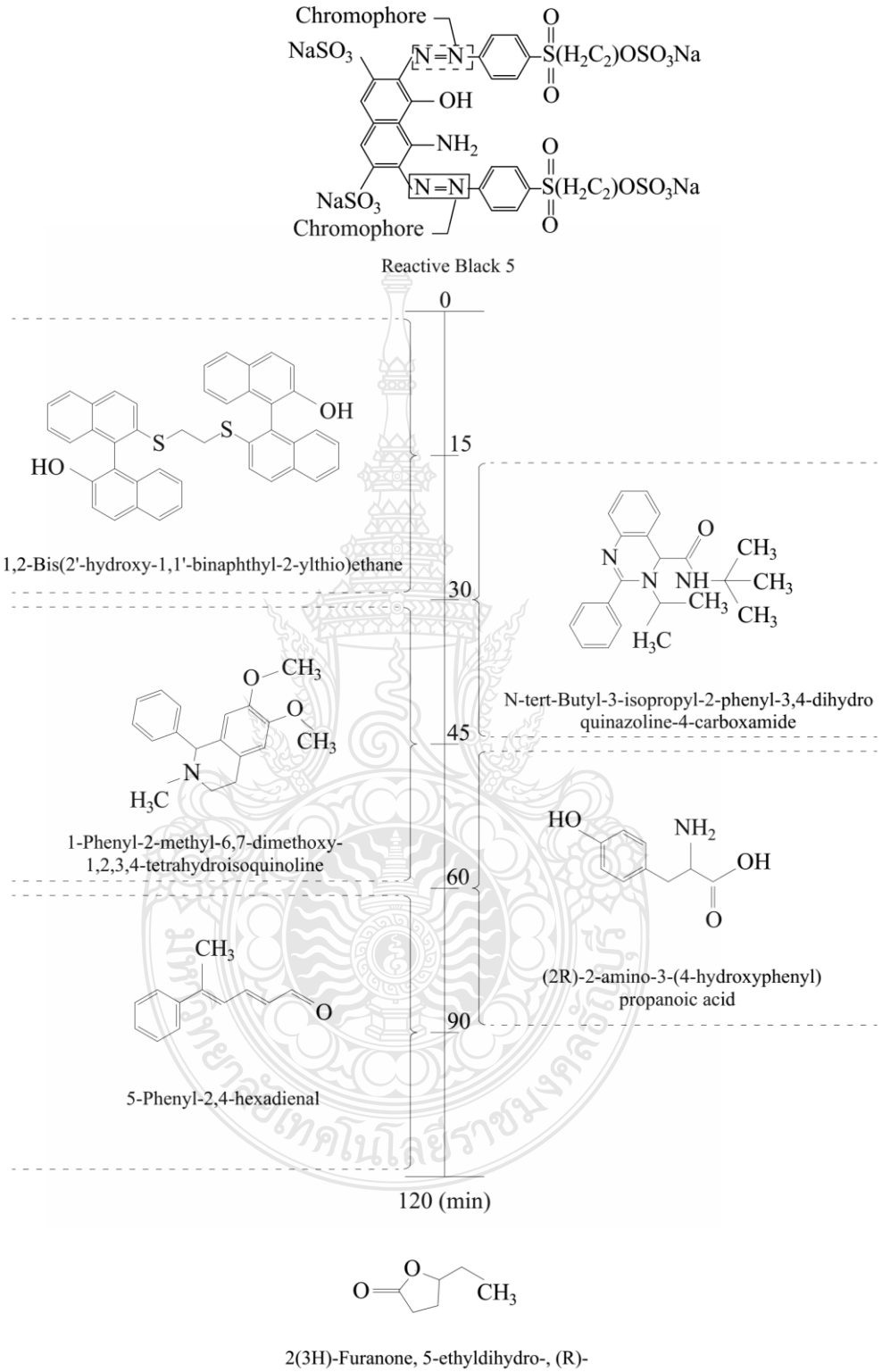

Figure 4.18 RB5 dye structure transformation for condition 5 (TZR+ UVA)

- **Photocatalytic mechanisms**

The results indicate that the proposed photocatalytic mechanism for TZR NCs is illustrated in Figure 4.19. Grasping the essential elements that enhance the photocatalytic efficiency of these NCs is vital. In the Calculation of the Conduction Band E_{CB}, and Valence Band E_{VB} The band edge positions of TiO_2 and ZnO were determined by applying the Mulliken-Jaffe equations (4.2) – (4.3), providing important insights into their contributions to improving overall photocatalytic performance.

$$E_{CB} = \chi - E_e - 0.5E_g \quad (4.2)$$

$$E_{VB} = E_{CB} + E_g \quad (4.3)$$

Where:

χ	=	Is the absolute electronegativity (eV)
E_e	=	Is the free electron energy on the hydrogen scale (4.5 eV)
E_{CB}	=	Is the conduction band (CB) potential
E_{VB}	=	Is the valence band (VB) potential
E_g	=	Is the bandgap by the UV-visible diffuse reflectance measurement

Detailed calculation procedure for E_{CB} and E_{VB} energy levels of TiO_2 and ZnO:

- Absolute electronegativity (χ) for TiO_2 = 5.81 eV [69], and E_g = 3.10 eV

E_{CB}= 5.81 eV − 4.5 eV − (0.5 × 3.10 eV)

E_{CB}= 5.81 eV − 4.5 eV − 1.55 eV

E_{CB}= − 0.24 eV

E_{VB} = − 0.24 eV + 3.10 eV

E_{VB} = + 2.86 eV

- Absolute eelectronegativity (χ) for ZnO = 5.79 eV [70], and E_g = 3.03 eV

E_{CB}= 5.79 eV − 4.5 eV − (0.5 × 3.03 eV)

E_{CB}= 5.79 eV − 4.5 eV − 1.51 eV

E_{CB}= − 0.22 eV

E_{VB} = − 0.22 eV + 3.03 eV

E_{VB} = + 2.81 eV

When the TZR NCs composite produces electron-hole pairs on light exposure, electrons (e^-) occupy the conduction band (CB), and holes (h^+) reside in valence bands (VB). Photogenerated electrons in the conduction band of ZnO (−0.24 eV vs. NHE) efficiently transfer to reduced graphene oxide, recombining with holes in the valence band of TiO_2 (+2.86 eV vs. NHE). This mechanism generates electrons and holes in ZnO and TiO_2, which participate in reduction and oxidation reactions. The electrons in the conduction band of TiO_2 (-0.22 eV vs. NHE) possess significant reducing capability and can produce superoxide radical anions ($•O^-_2$) by reducing adsorbed O_2 molecules. Concurrently, holes (h^+) in the valence band (VB) of ZnO (+2.81 eV vs. NHE) exhibit a high oxidation potential, resulting in the generation of hydroxyl radicals •OH, which are crucial for the degradation of pollutant compounds, characterized by its elevated conductivity and extended conjugation structure, functions as an electron acceptor, therefore diminishing charge-carrier recombination. the photocatalytic reaction mechanism illustrated in Figure 4.19 demonstrated a synergistic interplay between ZnO and TiO_2 under UVA light irradiation. Initially, photoexcitation generated electron-hole pairs in both semiconductors ZnO and TiO_2, (e^-) from ZnO (CB) migrated to TiO_2 (VB), while holes transferred inversely, suggesting a Z-scheme charge transfer mechanism. This spatial separation reduced recombination, enhancing redox efficiency.

The TiO_2 (CB) electrons reacted with adsorbed O_2, forming superoxide radicals, while holes in ZnO (VB) oxidized H_2O to hydroxyl radicals and protons. Subsequent reactions yielded secondary reactive species, including hydrogen peroxide (H_2O_2), and superoxide radicals ($•O^-_2$) mediated pathways. These oxidative species degraded organic pollutants into innocuous products through hydroxylation and cleavage reactions.

The cascade highlighted the critical role of heterojunction design in optimizing charge carrier dynamics. The interfacial electron transfer between ZnO and TiO_2 preserved the strong redox potentials of both components, enabling simultaneous oxidation and reduction. Furthermore, the generation of multiple reactive oxygen species (ROS) underscored the system's versatility in addressing complex pollutant matrices. This mechanistic insight aligned with prior studies on binary semiconductor systems, emphasizing interfacial engineering as a key strategy for advancing photocatalytic efficiency. The findings reinforced the environmental applicability of such systems for sustainable water treatment technologies.

resulting in the generation of (•OH), which is crucial for the degradation of pollutant compounds, characterized by its elevated conductivity and extended conjugation structure, functions as an electron acceptor, therefore diminishing charge-carrier recombination. The photogenerated electrons from the conduction band of TiO_2-ZnO are transferred to molecular (O_2), which is adsorbed on the surface of the photocatalyst, reducing it to ($\bullet O^-_2$) These superoxide radicals, along with (•OH) formed by the oxidation of water or hydroxyl ions, play a crucial role in the degradation of organic pollutants. The (ROS) attacks the molecular structures of organic pollutants, breaking them down into smaller, non-toxic compounds such as CO_2 and H_2O, which are the final products of the photocatalytic reactions, shown in Equations (4.4) - (4.13) and as shown in Figure 4.19.

$$ZnO + h\nu \longrightarrow ZnO\,(e^-_{CB} + h^+_{VB}) \quad (4.4)$$

$$TiO_2 + h\nu \longrightarrow TiO_2\,(e^-_{CB} + h^+_{VB}) \quad (4.5)$$

$$ZnO\,(e^-_{CB}) \longrightarrow TiO_2\,(e^-_{VB}) \quad (4.6)$$

$$TiO_2\,(h^+_{VB}) \longrightarrow ZnO\,(h^+_{VB}) \quad (4.7)$$

$$TiO_2\,(e^-_{CB}) + O_2 \longrightarrow \bullet O_2^- \quad (4.8)$$

$$ZnO\,(h^+_{VB}) + H_2O \longrightarrow \bullet OH + H^+ \quad (4.9)$$

$$\bullet O_2^- + H^+ \longrightarrow H_2O_2 \quad (4.10)$$

$$H_2O_2 + \bullet O_2^- \longrightarrow OH^- + \bullet OH + O_2 \quad (4.11)$$

$$\bullet OH + \text{Organic pollutants} \longrightarrow \text{Degraded products} \quad (4.12)$$

$$\bullet O_2^- + \text{Organic pollutants} \longrightarrow \text{Degraded products} \quad (4.13)$$

Moreover, added RGO to TiO_2-ZnO can enhance photocatalytic performance through improved light absorption, charge carrier separation, synergistic effect from heterojunction formation, and increased surface area for reaction. These improvements make the RGO-modified composites an attractive candidate for efficient photocatalytic applications. The presence of RGO can accelerate the degradation process and improve the overall performance of the photocatalytic system, demonstrating its potential for environmental remediation applications.

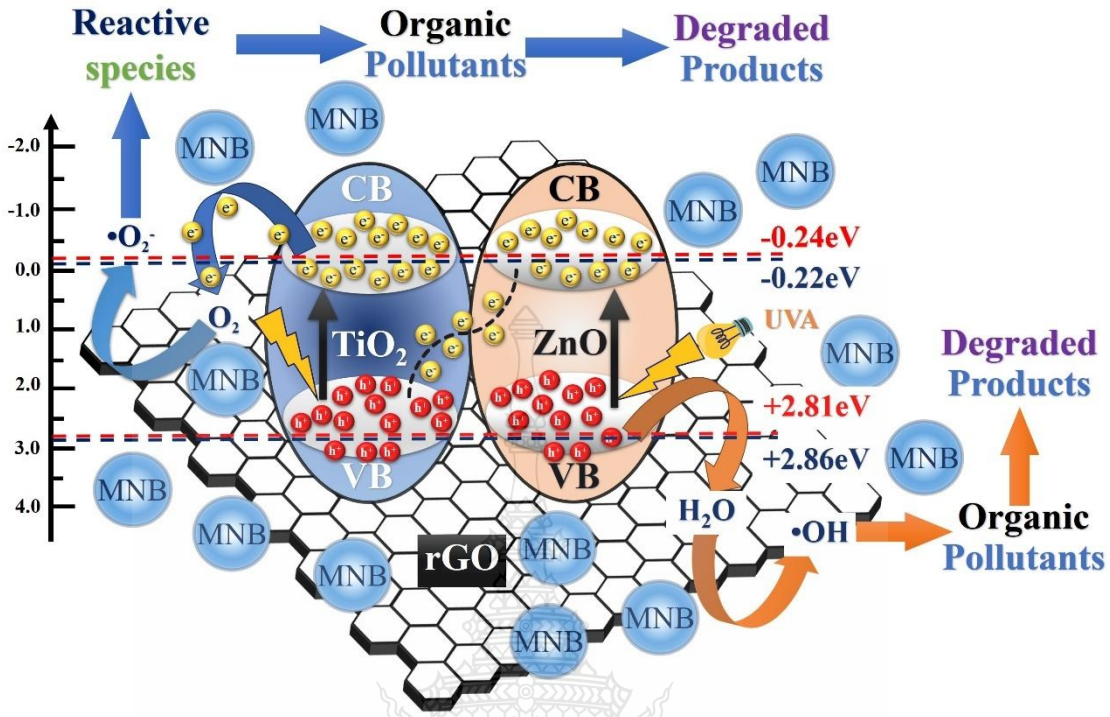

Figure 4.19 Reaction mechanism diagram of TiO_2, ZnO, and RGO.

4.3 Kinetic study

The study tested synthetic wastewater treatment agents' photocatalytic removal of carbaryl, RB5 dyes, and IC dyes utilizing four photocatalysts: TZR, ZR, TR, and TZ. This technique was done using UV light at 1,250 μW.cm^{-2}. By studying and computing first-order kinetics and reaction rates, we got an equation for a first-order reaction with several equivalent forms. This showed that the removal was very effective. These forms can be altered to obtain the same result. The optical reduction test kinetics assessed synthetic effluent treatment with IC dye, RB5, and carbaryl insecticide at their original concentrations. The first-order kinetic model is used in optical reduction simulations. This suggests that time and chemical concentration are linked. Using the first-order kinetic model, this study estimated changes in synthetic dye IC, RB5, and carbaryl pesticide wastewater treatment rates. It depends on your initial concentration. Equation 4.14 shows the first-order linear optical reduction:

$$ln\left(\frac{C_0}{C}\right)=k.t \qquad (4.14)$$

Where:

C_0 = The initial concentration of the reactant (mg. L^{-1})

C = The concentration of the reactant at time t

k = Pseudo-first-order kinetics the rate constant (min^{-1})

t = the time

The pseudo-first-order model $ln(C_0/C) = k.t$ was utilized to analyze the experimental data collected to ascertain the kinetics of IC, RB5 dyes, and carbaryl pesticides with the synthesized photocatalysts shown in Figure 4.20. In this model, C_0 denotes the initial concentration, C signifies the concentration, t indicates time, and k represents the first-order rate constant. Moreover, the slope of the regression line is equal to the apparent first-order rate constant (k). The degradation efficiency and R^2 values are shown in Table 4.4.

Table 4.4 Rate Constant (k) and correlation coefficient (R^2) for different photocatalysts

Experiment condition	IC		RB5		Carbaryl	
	k (min^{-1})	R^2	k (min^{-1})	R^2	k (min^{-1})	R^2
TZR+ UVA+MNB	3.25×10^{-2}	0.999	5.01×10^{-2}	0.998	4.73×10^{-2}	0.998
TZ+ UVA+MNB	1.70×10^{-2}	0.969	1.25×10^{-2}	0.957	2.01×10^{-2}	0.996
TR+ UVA+MNB	1.23×10^{-2}	0.972	5.30×10^{-3}	0.965	1.21×10^{-2}	0.996
ZR+ UVA+MNB	1.11×10^{-2}	0.972	1.70×10^{-3}	0.946	8.70×10^{-3}	0.994
TZR+UVA	2.61×10^{-2}	0.997	2.46×10^{-2}	0.997	3.21×10^{-2}	0.998
TZ+UVA	1.55×10^{-2}	0.957	1.34×10^{-2}	0.982	1.73×10^{-2}	0.967
TR+UVA	9.80×10^{-3}	0.980	5.70×10^{-3}	0.974	9.30×10^{-3}	0.912
ZR+UVA	8.10×10^{-3}	0.995	2.90×10^{-3}	0.942	5.40×10^{-3}	0.857

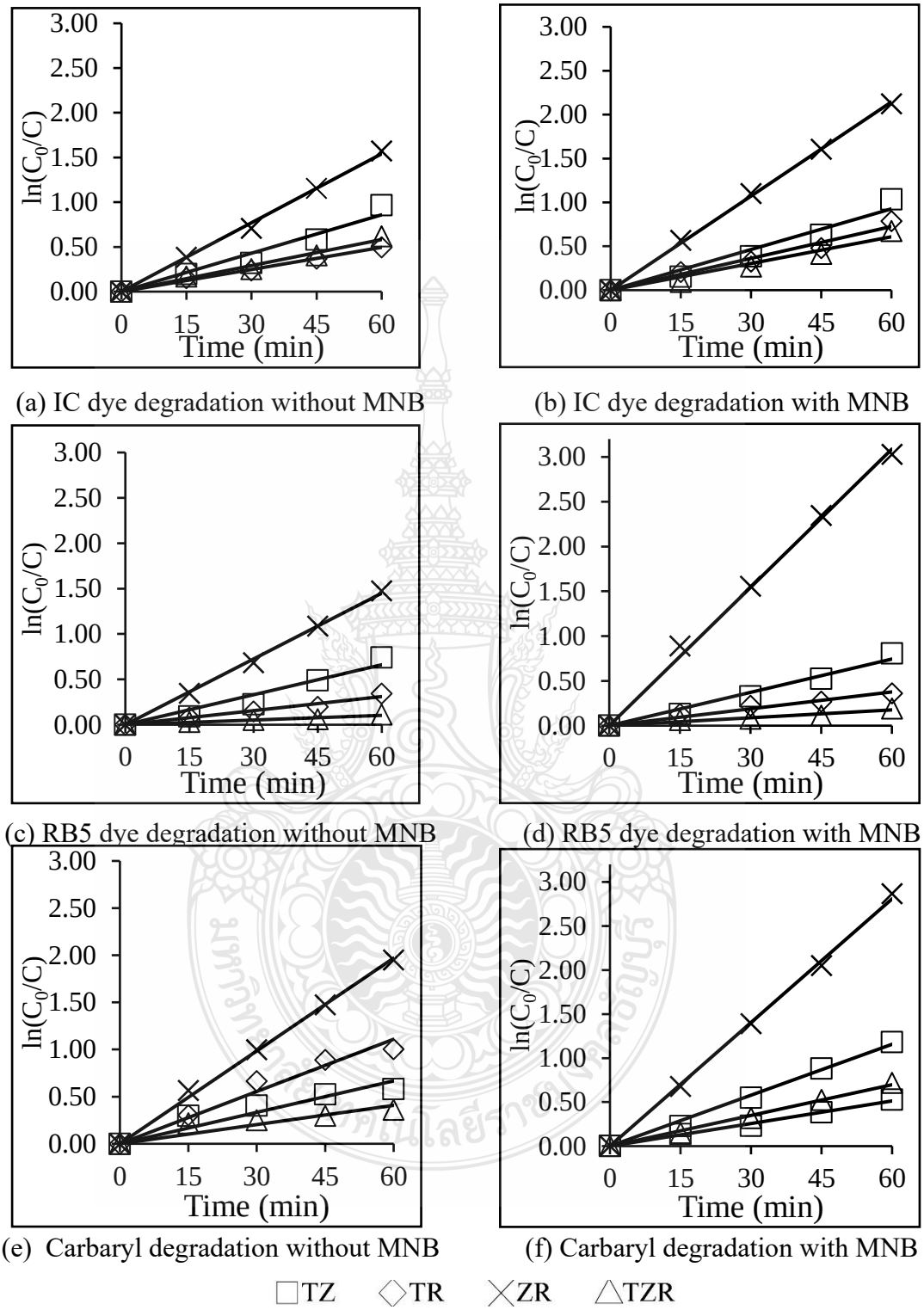

Figure 4.20 Pseudo-first-order kinetics plots for the degradation of various IC, RB5 dyes, and Carbaryl pesticides using all synthesized photocatalysts.

Table 4.5 Comparison of the photocatalytic degradation

Contaminants	Photocatalysts		Photocatalyst dose (g)	Intensity ($\mu W.cm^{-2}$)	Time (min)	k (min^{-1})	Specific rates ($min^{-1}.g^{-1}.\mu W^{-1}.cm^{-2}$)	Ref.
	Type	Form						
IC	TZR+MNB	Powder	0.1	1.25×10^{3}	120	3.25×10^{-2}	2.17×10^{-06}	This study
	TZR+MNB					2.61×10^{-2}	1.74×10^{-06}	
RB5	TZR+MNB					2.46×10^{-2}	1.64×10^{-06}	
	TZR					5.01×10^{-2}	3.34×10^{-06}	
Carbaryl	TZR					4.73×10^{-2}	3.15×10^{-06}	
	TZR					3.21×10^{-2}	2.14×10^{-06}	
IC	AC/1.0%Ag–TiO_2	Activated Carbon	2	1.25×10^{3}	180	2.54×10^{-2}	5.64×10^{-08}	[71]
RB5	AC/0.5%Ag–TiO_3					1.79×10^{-2}	3.98×10^{-08}	
Carbaryl	AC/0.5%Ag–TiO_3					2.40×10^{-2}	5.33×10^{-08}	
IC	$BiVO_4/gC_3N_4$/rGO	Powder	0.5	1.25×10^{3}	150	3.37×10^{-4}	3.59×10^{-09}	[72]
MB						9.85×10^{-5}	1.05×10^{-09}	
Congo red	ZnO/RGO	Powder	2	3.97×10^{3}	60	2.85×10^{-2}	5.98×10^{-08}	[73]
MB	ZnO/TiO_2 1:25	Powder	0.04	1.15×10^{5}	120	6.64×10^{-3}	2.96×10^{-05}	[74]
RR 198	ZnO	Powder	0.12	4.19×10^{4}	180	1.88×10^{-2}	4.26×10^{-05}	[75]
IC	g-C_3N_4/Bi_2S_3	Powder	0.5	1.25×10^{3}	120	6.74×10^{-3}	8.99×10^{-08}	[76]
RB5						6.90×10^{-3}	9.20×10^{-08}	
RhB	CdSe-ZnO	Powder	1.5	1.00×10^{7}	240	1.39×10^{-2}	3.86×10^{-12}	[77]

Remark: TZR+MNB rates compete with the literature's photocatalytic efficiency. Between the higher performance metrics of ZnO/TiO_2 1:25 and the lower rates of g-C_3N_4/Bi_2S_3. Experimental photocatalytic process upgrades enhanced reaction kinetics in this medium range. The findings balanced activity and reducing limitations of less efficient older technologies, representing modern material innovation trends while remaining practical.

CHAPTER 5
DISCUSSION OF RESULTS AND RECOMMENDATIONS

5.1 Discussion of results

The study of the photocatalytic degradation of IC, RB5 dyes, and carbaryl pesticides in synthetic wastewater through a photocatalytic process utilizing TZR photocatalysts under UVA light and MNB aeration can encapsulate the physical properties and effectiveness of the photocatalytic process on IC, RB5 dyes, and carbaryl pesticides as follows

5.1.1 Discussion of physical properties of photocatalysts

This research uses the TZR nanocomposite. By integrating anatase-phase TiO_2, ZnO, and reduced graphene oxide (rGO), the composite improves photocatalytic activity, as demonstrated by structural investigations. For effective charge transfer and reduced electron-hole recombination, XRD peaks at 25.3°, 37.8°, 48.0°, and 55.1° suggest strong crystallinity; chemical characterization by FT-IR and XPS confirmed O-H, Ti-O, and Zn-O bonds, which gave the catalyst stability and reactivity. After C=C stretching, rGO increased the composite's electronic conductivity and structural stability, enabling efficient degradation in various environmental conditions. BET surface area analysis revealed a significant 69.522 $m^2.g^{-1}$, enabling pollutant interaction and degradation analysis with SEM and TEM revealed a nanoscale distribution of TiO_2 and ZnO in the rGO matrix, enhancing light absorption. The composite's lowered bandgap of 2.93 eV extends its activity into the visible spectrum, outperforming standard TiO_2 and ZnO photocatalysts. The broad-spectrum photocatalytic potential of TZR makes it a sustainable choice for large-scale solar-assisted wastewater treatment. These findings show that TZR can reduce water pollution in a scalable, cost-effective manner in environmental nanotechnology.

5.1.2 Results of MNB aeration

The results of MNB aeration indicate a significant enhancement in dissolved oxygen (DO) levels in synthetic wastewater, with DO values increasing from 8.10 mg. L^{-1} before aeration to 15.14 mg. L^{-1} following the aeration process. The most frequently observed bubble size was 102.1±1.0 nm. Furthermore, combining MNB

aeration with a TZR photocatalyst resulted in the synthetic wastewater's highest oxidation-reduction potential (ORP), thereby boosting the system's oxidative capacity and playing a crucial role in effectively breaking contaminants. The results highlight the success of integrating MNB aeration with the TZR photocatalyst, utilizing the improved oxygen availability and elevated redox potential to enhance the breakdown of wastewater contaminants.

5.1.3 Evaluation of treatment efficacy

This study shows that photocatalysts and MNB break down organic contaminants such as IC, RB5 dye, and carbaryl. Condition 1 (TZR + UVA + MNB) degraded synthetic wastewater best, with 99.08% IC, 98.73% RB5, and 98.98% carbaryl. IC, RB5, and carbaryl achieved 98.30%, 97.83%, and 97.17% in Condition 5 (TZR + UVA). TZR is more effective in absorbing UVA radiation, separating electrons and holes, and producing reactive oxygen species. UVA light activates TiO_2 and ZnO composites. This produces holes in the valence band and transports electrons to the conduction band. ROS such as •OH and superoxide anions ($•O_2^-$) break down organic contaminants when electrons and holes interact with H_2O and CO_2 in the medium. (RGO) improves the TZR system and ROS availability by increasing electron transit and preventing charge recombination. MNB increases mass transfer and dissolved oxygen, making them ideal for photocatalytic processes. Metal nanoparticles increase pollutant-catalyst interaction by increasing oxygen availability and reactive oxygen species. This helps pollutants degrade at the catalyst contact. This study supports prior findings that MNB improves O_2 transfer and photocatalytic efficiency. MNB improves breakdown, but photocatalysts' UVA absorption and ROS production restrict them. The static dye concentrations weaken this work. This indicates further study on dye concentrations, MNB levels, and photocatalysts is needed to optimize wastewater degradation.

5.1.4 Results of kinetic

The kinetic investigation of the photocatalytic degradation of IC, RB5 dye, and carbaryl in synthetic wastewater, utilizing different photocatalysts under UVA light with MNB aeration, revealed that a pseudo-first-order kinetic model most accurately represents the reaction mechanism. The results showed that adding MNB aeration greatly enhanced

the ability of IC, RB5 dye, and carbaryl to treat synthetic wastewater, with reaction rates going up by 3.25×10^{-2}, 2.46×10^{-2}, and 4.73×10^{-2}, respectively.

5.2 Recommendation

5.2.1 Investigate the impact of efficiency and longevity of photocatalysts on their reusability and material durability

5.2.2 Investigate the effectiveness of wastewater treatment by altering the aeration conditions of MNB in different configurations, either continuously or intermittently, throughout the experiment (Step-feed of MNB aeration).

List of Bibliography

[1] Su, R., et al. 2020. "Oxygen Reduction Reaction in the Field of Water Environment for Application of Nanomaterials. **Nanomaterials,** 10, (9): pp.1719.

[2] Altowayti, W.A.H., et al. 2022. "The Role of Conventional Methods and Artificial Intelligence in the Wastewater Treatment: A Comprehensive Review. **Processes**, 10, (9): pp.1832.

[3] Mu, X., S. Lu, and Q. Li. 2023. "How to Promote the Development of Industrial Wastewater Treatment Technological Innovation in China: A Tripartite Evolutionary Game Analysis. **Sustainability**, 15, (21): pp.15359.

[4] Kato, S. and Y. Kansha. 2024. "Comprehensive review of industrial wastewater treatment techniques. **Environmental Science and Pollution Research,** 31, 39: pp.51064-51097.

[5] Khan, S., M. Chowdhury, and U. Nandy. 2023. "Solar-wind-power Hybrid Power Generation System. **Journal of Engineering Research and Reports**, 25, pp.145-152.

[6] Vargas-Estrada, L., et al. 2021. "Energy and Nutrients Recovery From Wastewater Cultivated Microalgae: Assessment of the Impact of Wastewater Dilution on Biogas Yield. **Bioresource Technology**, 341, pp.125755.

[7] Khaksar, M.R., H. Ganjidoust, and B. Ayati. 2021. "Photocatalytic oxidation of waste activated sludge using a backlight photocatalytic reactor. **Desalination and Water Treatment,** 235, pp.117-126.

[8] Gopinath, K.P., et al. 2020. "Present Applications of Titanium Dioxide for the Photocatalytic Removal of Pollutants From Water: A Review. **Journal of Environmental Management,** 270, pp.110906.

[9] Liu, Z., et al. 2021. "Making Waves: Improving Removal Performance of Conventional Wastewater Treatment Plants on Endocrine Disrupting Compounds (EDCs): Their Conjugates Matter. **Water Research**, 188, pp.116469.

List of Bibliography (Continued)

[10] Ekblad, M., et al. 2021. "Influence of Operational Conditions and Wastewater Properties on the Removal of Organic Micropollutants Through Ozonation. **Journal of Environmental Management**, 286, pp.112205.

[11] Chen, C.-X., et al. 2024. "Anthraquinones-Based Photocatalysis: A Comprehensive Review. **Environmental Science and Ecotechnology,** 22, pp.100449.

[12] Gabet, A., et al. 2021. "Hydrogen peroxide and persulfate activation using UVA-UVB radiation: Degradation of estrogenic compounds and application in sewage treatment plant waters. **Journal of Hazardous Materials,** 405, pp.124693.

[13] Mukhopadhyay, R., et al. 2021. "Nanomaterials for Sustainable Remediation of Chemical Contaminants in Water and Soil. **Critical Reviews in Environmental Science and Technology,** 52, (15): pp.2611-2660.

[14] Waso, M., et al. 2020. "Predatory Bacteria in Combination With Solar Disinfection and Solar Photocatalysis for the Treatment of Rainwater. **Water Research,** 169, pp.115281.

[15] Hermosilla, D., et al. 2020. "Environmentally friendly synthesized and magnetically recoverable designed ferrite photo-catalysts for wastewater treatment applications. **Journal of Hazardous Materials,** 381, pp.121200.

[16] Wang, F., et al. 2021. "Bactericidal Efficiency and Photochemical Mechanisms of Micro/Nano Bubble–enhanced Visible Light Photocatalytic Water Disinfection. **Water Research,** 203, pp.117531.

[17] Rojviroon, O. and T. Rojviroon. 2022. "Photocatalytic process augmented with micro/nano bubble aeration for enhanced degradation of synthetic dyes in wastewater. **Water Resources and Industry,** 27, pp.100169.

[18] Jamal, S., et al. 2023. "The Impact of Organochlorine Pesticides (OCPs) on Environment Health. **Poltekita Jurnal Ilmu Kesehatan,** 17, 2: pp.295-301.

[19] Pelosi, C., et al. 2021. "Residues of Currently Used Pesticides in Soils and Earthworms: **A Silent Threat Agriculture Ecosystems & Environment**, 305, pp.107167.

List of Bibliography (Continued)

[20] Jepson, P.C., et al. 2020. "Selection of Pesticides to Reduce Human and Environmental Health Risks: A Global Guideline and Minimum Pesticides List. **The Lancet Planetary Health**, 4, (2): pp.e56-e63.

[21] Xu, S.B., et al. 2022. "Analysis of Serum Levels of Organochlorine Pesticides and Related Factors in Parkinson's Disease. **Neurotoxicology,** 88, pp.216-223.

[22] Rubio-Palis, Y., et al. 2023. "Insecticide Resistance Levels and Associated Mechanisms in Three Aedes Aegypti Populations From Venezuela. **Memórias Do Instituto Oswaldo Cruz**, 118, pp.e220210.

[23] None, N., et al. 2022. "An Overview of Insecticide Usage and Resistance of Insect Vector to Insecticide: An Implication to Public Health. **Journal of Public Health and Diseases**, 5, 2: pp.16-20.

[24] Salinas, W.S., T.P. Feria-Arroyo, and C.J. Vitek. 2021. "Temperatures Influence Susceptibility to Insecticides in Aedes Aegypti and Aedes Albopictus (Diptera: Culicidae) Mosquitoes. **Pathogens**, 10, (8): pp.992.

[25] Zoh, M.G., et al. 2021. "Experimental Evolution Supports the Potential of Neonicotinoid-Pyrethroid Combination for Managing Insecticide Resistance in Malaria Vectors. **Scientific Reports**, 11, (1): pp.19501.

[26] Ćwieląg-Piasecka, I., M. Dębicka, and A. Medyńska-Juraszek. 2021. "Effectiveness of Carbaryl, Carbofuran and Metolachlor Retention in Soils Under the Influence of Different Colloid. **Minerals,** 11, (9): pp.924.

[27] Siriruttanapruk, S., et al. 2022. "Identification and Priority Setting for Occupational Carcinogens (OCs) in Industries in Thailand. **Outbreak Surveillance Investigation & Response (Osir) Journal,** 15, 4: pp.123-130.

[28] Jadaa, W., A. Prakash, and A.K. Ray. 2021. "Recent Advances in the Photocatalytic Degradation of Direct Blue Dyes: A Critical Minireview and Analysis Study. **Biomedical Journal of Scientific & Technical Research,** 33, (3): pp.2574.

[29] Benkhaya, S., S. M'rabet, and A.E. Harfi. 2020. "Classifications, Properties, Recent Synthesis and Applications of Azo Dyes. **Heliyon,** 6, (1): pp.e03271.

List of Bibliography (Continued)

[30] Koenig, K., et al. 2020. "Biobased Dyes as Conductive Additives to Reduce the Diameter of Polylactic Acid Fibers During Melt Electrospinning. **Materials,** 13, (5): pp.1055.

[31] Mallick, A. and T. Majumdar. 2021. "True-Photonic Strategy for Chemically Encrypted Two-Factor Authentication With Unlimited Chemical Passwords Based on Cascade Energy Transfer Under a Single Wavelength Excitation. **Acs Applied Electronic Materials, 3**, (8): pp.3588-3598.

[32] Dassanayake, R.S., S. Acharya, and N. Abidi. 2021. "Recent Advances in Biopolymer-Based Dye Removal Technologies. **Molecules,** 26, (15): pp.4697.

[33] Kamble, G.S. and Y.C. Ling. 2020. "Solvothermal Synthesis of Facet-Dependent $BiVO_4$ Photocatalyst With Enhanced Visible-Light-Driven Photocatalytic Degradation of Organic Pollutant: Assessment of Toxicity by Zebrafish Embryo. **Scientific Reports,** 10, (1): pp.12993.

[34] Pagnacco, M.C., et al. 2022. "Indigo Carmine in a Food Dye: Spectroscopic Characterization and Determining Its Micro-Concentration Through the Clock Reaction. **Molecules,** 27, 15: pp.4853.

[35] Wayan, I., et al. 2021. "Textile Dye Reactive Black 5 (RB5) Bio-Sorption with Moving Bed Biofilm Reactor and Activated Sludge. I**JEEM - Indonesian Journal of Environmental Education and Management**, 5, pp.67-71.

[36] Zhao, Y., et al. 2020. "Two-Dimensional Photocatalyst Design: A Critical Review of Recent Experimental and Computational Advances. **Materials Today,** 34, pp.78-91.

[37] Fatimah, I., et al. 2019. "Physicochemical Characteristics and Photocatalytic Performance of TiO_2/SiO_2 Catalyst Synthesized Using Biogenic Silica From Bamboo Leaves. **Heliyon,** 5, 11: pp.e02766.

[38] Wang, N., et al. 2023. "Enhanced Visible-Photocatalytic Activities in Strong Acids and Strong Alkalis of Flexible Iron–$SrTiO_3$ Nanofibrous Membranes. **Langmuir,** 39, 19: pp.6885-6894.

List of Bibliography (Continued)

[39] Prucnal, S., et al. 2023. "TiO_2 Phase Engineering by Millisecond Range Annealing for Highly Efficient Photocatalysis. **The Journal of Physical Chemistry C**, 127, 26: pp.12686-12694.

[40] Kim, J.K., et al. 2021. "A Study on TiO_2 Surface Texturing Effect for the Enhancement of Photocatalytic Reaction in a Total Phosphorous Concentration Measurement System. **Micromachines,** 12, (10): pp.1163.

[41] Khabir, Z., et al. 2021. "Human Epidermal Zinc Concentrations After Topical Application of ZnO Nanoparticles in Sunscreens. **International Journal of Molecular Sciences**, 22, (22): pp.12372.

[42] Nizami, M.Z.I., et al. 2022. "In Vitro Studies of Graphene for Management of Dental Caries and Periodontal Disease: A Concise Review. **Pharmaceutics,** 14, 10: pp.1997.

[43] Mandal, S., et al. 2020. "An Overview on Graphene-Metal Oxide Semiconductor Nanocomposite: A Promising Platform for Visible Light Photocatalytic Activity for the Treatment of Various Pollutants in Aqueous Medium. **Molecules**, 25, (22): pp.5380.

[44] Akbar, F. 2023. "The Potential Energy Saving in Lighting Systems on Campuses in Tropical Areas: A Combination of Natural and Artificial Light. **Gjeset,** 1, 1: pp.48-57.

[45] Oh, S.-T. 2023. "CRI-Based Smart Lighting System That Provides Characteristics of Natural Light. **Information,** 14, 12: pp.628.

[46] Wang, B., et al. 2022. "Prediction Model and Influencing Factors of CO_2 Micro/Nanobubble Release Based on ARIMA-BPNN. Agriculture, 12, 4: pp.445.

[47] Döbelin, N. 2020. "Validation of XRD Phase Quantification Using Semi-Synthetic Data. **Powder Diffraction,** 35, (4): pp.262-275.

[48] Khan, M.A., et al. 2021. "Advanced Nanoscale Surface Characterization of CuO Nanoflowers for Significant Enhancement of Catalytic Properties. **Molecules**, 26, (9): pp.2700.

List of Bibliography (Continued)

[49] Fadlelmoula, A., et al. 2022. "Fourier Transform Infrared (FTIR) Spectroscopy to Analyse Human Blood over the Last 20 Years: A Review towards Lab-on-a-Chip Devices. **Micromachines,** 13, (2): pp.187.

[50] Nawa, K., et al. 2021. "Modification of the van der Waals interaction at the Bi_2Te_3 and Ge(111) interface. **Physical Review Materials,** 5, pp.024203.

[51] Venkatadri, B., et al. 2020. "Green Synthesis of Silver Nanoparticles Using Aqueous Rhizome Extract of Zingiber Officinale and Curcuma Longa: In-Vitro Anti-Cancer Potential on Human Colon Carcinoma HT-29 Cells. **Saudi Journal of Biological Sciences,** 27, (11): pp.2980-2986.

[52] Zhang, Y., et al. 2022. "Comparison of Different Volatile Extraction Methods for the Identification of Fishy Off-Odor in Fish by-Products. **Molecules,** 27, 19: pp.6177.

[53] Alsheheri, S. 2021. "Nanocomposites containing titanium dioxide for environmental remediation. **Designed Monomers and Polymer**s, 24, pp.22-45.

[54] Berberidou, C., et al. 2019. "Photocatalytic disinfection and purification of water employing reduced graphene oxide/TiO_2 composites. **Journal of Chemical Technology & Biotechnology,** 94, (12): pp.3905-3914.

[55] Khurshid, F., et al. 2019. "Ag-doped ZnO nanorods embedded reduced graphene oxide nanocomposite for photo-electrochemical applications. **Royal Society Open Science,** 6, pp.181764.

[56 Lu, H., et al. 2022. "One-step electrodeposition of ZnO/graphene composites with enhanced capability for photocatalytic degradation of organic dyes. **Frontiers in Chemistry,** 10, pp.1061129.

[57] Kocijan, M., et al. 2021. "Enhanced Photocatalytic Activity of Hybrid rGO@TiO_2/CN Nanocomposite for Organic Pollutant Degradation under Solar Light Irradiation. **Catalysts, 1**1, (9): pp.1023.

[58] Waghmode, M.S., et al. 2019. "Studies on the titanium dioxide nanoparticles: biosynthesis, applications and remediation. **SN Applied Sciences**, 1, (4): pp.310.

List of Bibliography (Continued)

[59] Wu, K. and J. Chen. 2019. "Study of ZnO Nanoparticles-Decorated TiO_2/Facets Heterostructures and Their Photocatalytic Activity. **Solid State Phenomena,** 298, pp.175-180.

[60] Pant, B., et al. 2020. "Synthesis and Characterization of ZnO-TiO_2/Carbon Fiber Composite With Enhanced Photocatalytic Properties. **Nanomaterials**, 10, (10): pp.1960.

[61] Xu, K., et al. 2020. "Construction of Ag-modified TiO_2/ZnO heterojunction nanotree arrays with superior photocatalytic and photoelectrochemical properties. **RSC Advances**, 10, (57): pp.34702-34711.

[62] Wang, Q., et al. 2021. "Gliadin-mediated green preparation of hybrid zinc oxide nanospheres with antibacterial activity and low toxicity. **Scientific Reports,** 11, pp.10373.

[63] Ruidíaz-Martínez, M., et al. 2020. "Hydrothermal Synthesis of rGO-TiO_2 Composites as High-Performance UV Photocatalysts for Ethylparaben Degradation. **Catalysts,** 10, (5): pp.520.

[64] Siwińska-Stefańska, K., et al. 2018. "TiO_2-ZnO Binary Oxide Systems: Comprehensive Characterization and Tests of Photocatalytic Activity. **Materials,** 11, 5: pp.841.[

65] Alaizeri, Z.M., et al. 2024. "Green synthesis of ZnO-TiO_2/RGO nanocomposites using *Senna surattensis* extract: a novel approach for enhanced anticancer efficacy and biocompatibility. **RSC Advances,** 14, 24: pp.16685-16695.

[66] Qin, G., et al. 2017. "Novel graphene nanosheet-wrapped polyaniline rectangular-like nanotubes for flexible all-solid-state supercapacitors. J**ournal of Materials Science,** 52, 18: pp.10981-10992.

[67] Heng, J.Z.X., et al. 2021. "Solar-Powered Photodegradation of Pollutant Dyes Using Silver-Embedded Porous TiO_2 Nanofibers. **Nanomaterials,** 11, (4): pp.856.

[68] Xu, J.-J., et al. 2023. "ZnO Nanoparticles Modified by Carbon Quantum Dots for the Photocatalytic Removal of Synthetic Pigment Pollutants. **ACS Omega,** 8, (8): pp.7845-7857.

List of Bibliography (Continued)

[69] Girish, Y.R., et al. 2022. "Facile and rapid synthesis of solar-driven TiO_2/g-C_3N_4 heterostructure photocatalysts for enhanced photocatalytic activity. **Journal of Science: Advanced Materials and Devices**, 7, (2): pp.100419.

[70] Ullah, H., et al. 2020. "Effect of vegetable waste extract on microstructure, morphology, and photocatalytic efficiency of ZnO–CuO nanocomposites. **Inorganic and Nano-Metal Chemistry,** 51, pp.1-13.

[71] Leelert, Y., et al. 2024. "Synergistic effects of micronanobubbles and AC/Ag–TiO_2 nanocomposites in photocatalytic process. **Biocatalysis and Agricultural Biotechnology,** 57, pp.103096.

[72] Akechatree, N., et al. 2025. "Development of Z-scheme $BiVO_4$/g-C_3N_4/rGO heterojunction nanocomposite for enhanced photocatalytic degradation and antibacterial activity. **Materials Research Bulletin,** 181, pp.113119.

[73] Pang, Y.L., et al. 2018. "Enhancement of Photocatalytic Degradation of Organic Dyes Using ZnO Decorated on Reduced Graphene Oxide (rGO). Desalination and **Water Treatment,** 108, pp.311-321.

[74] Haghighatzadeh, A., et al. 2019. "Improved Photocatalytic Activity of ZnO-TiO_2 Nanocomposite Catalysts by Modulating TiO_2 Thickness. **Materials Research Express,** 6, (11): pp.115060.

[75] Biglar, F., et al. 2021. "Application of ZnO-Nd Nano-Photocatalyst for the Reactive Red 198 Dye Decolorization in the Falling-Film Photocatalytic Reactor. **Toxics,** 9, (10): pp.254.

[76] Rajendran, R., et al. 2024. "Design and fabrication of g-C_3N_4/Bi_2S_3 heterojunction photocatalysts for efficient organic pollutant degradation and antibacterial activity. **Journal of Alloys and Compounds**, 976, pp.173116.

[77] Alshamsi, H.A., M.A.A. Bedairy, and S.H. Alwan. 2021. "Visible Light Assisted Photocatalytic Degradation of Rhodamine B Dye on CdSe-ZnO Nanocomposite: Characterization and Kinetic Studies. **Iop Conference Series Earth and Environmental Science**, 722, (1): pp.012005.

APPENDICES

APPENDIX A

Experimental results

Table A1 Treatment of IC dye in synthetic wastewater by the photocatalytic process at an initial concentration of 100 ppm of Experiment condition 1.

Time (min)	(ADMI)			(Abs)			Conc. (mg/L)			C/C_0
	1	2	Average	1	2	Average	1	2	Average	
0	7780	7831	7806	3.22	3.25	3.23	101.27	101.93	101.60	1.00
15	4225	3963	4094	1.78	1.89	1.83	55.76	59.40	57.58	0.57
30	1361	3837	2599	0.56	1.59	1.08	17.72	49.95	33.83	0.33
45	449	683	566	0.19	1.11	0.65	5.84	34.93	20.39	0.20
60	101	275	188	0.04	0.73	0.39	1.32	22.96	12.14	0.12
90	99	174	137	0.04	0.15	0.10	1.29	4.84	3.06	0.03
120	52	92	72	0.04	0.05	0.05	1.26	1.63	1.44	0.01
ADMI eff (%)	99.33	98.82	99.08							

Table A2 Treatment of IC dye in synthetic wastewater by the photocatalytic process at an initial concentration of 100 ppm of Experiment condition 2.

Time (min)	(ADMI)			(Abs)			Conc. (mg/L)			C/C_0
	1	2	Average	1	2	Average	1	2	Average	
0	7756	7831	7793	3.22	3.25	3.23	101.27	101.93	101.60	1.00
15	6598	6672	6635	2.79	2.77	2.78	87.48	86.85	87.17	0.86
30	4976	5051	5013	2.30	2.09	2.20	72.31	65.75	69.03	0.68
45	3340	3415	3377	2.03	1.42	1.72	63.83	44.45	54.14	0.53
60	1959	2034	1997	1.26	1.04	1.15	39.52	32.76	36.14	0.36
90	1030	1105	1068	0.34	0.46	0.40	10.81	14.39	12.60	0.12
120	565	639	602	0.31	0.27	0.29	9.83	8.32	9.08	0.09
ADMI eff (%)	92.75	91.80	92.28							

Table A3 Treatment of IC dye in synthetic wastewater by the photocatalytic process at an initial concentration of 100 ppm of Experiment condition 3.

Time (min)	(ADMI)			(Abs)			Conc. (mg/L)			C/C_0
	1	2	Average	1	2	Average	1	2	Average	
0	7756	7831	7793	3.22	3.25	3.23	101.27	101.93	101.60	1.00
15	7186	7288	7237	2.87	3.02	2.95	90.22	94.86	92.54	0.91
30	6771	5519	6145	2.66	2.29	2.48	83.65	71.84	77.74	0.77
45	6513	4534	5524	2.41	1.88	2.14	75.58	59.02	67.30	0.66
60	6127	3041	4584	2.03	1.26	1.65	63.89	39.58	51.74	0.51
90	5726	1810	3768	1.58	0.75	1.16	49.47	23.56	36.52	0.36
120	1651	1724	1687	0.65	0.45	0.55	20.54	14.04	17.29	0.17
ADMI eff (%)	78.70	77.76	78.23							

Table A4 Treatment of IC dye in synthetic wastewater by the photocatalytic process at an initial concentration of 100 ppm of Experiment condition 4.

Time (min)	(ADMI)			(Abs)			Conc. (mg/L)			C/C_0
	1	2	Average	1	2	Average	1	2	Average	
0	7756	7831	7793	3.22	3.25	3.23	101.27	101.93	101.60	1.00
15	5992	6050	6021	2.75	2.51	2.63	86.38	78.75	82.57	0.81
30	5022	5080	5051	2.56	2.11	2.33	80.41	66.12	73.27	0.72
45	4040	4098	4069	2.31	1.70	2.00	72.56	53.34	62.95	0.62
60	2481	2539	2510	1.90	1.05	1.47	59.59	33.05	46.32	0.46
90	1141	1195	1168	1.06	0.70	0.88	33.20	21.89	27.55	0.27
120	883	941	912	0.86	0.40	0.63	27.05	12.41	19.73	0.19
ADMI eff (%)	88.53	87.79	88.16							

Table A5 Treatment of IC dye in synthetic wastewater by the photocatalytic process at an initial concentration of 100 ppm of Experiment condition 5.

Time (min)	(ADMI)			(Abs)			Conc. (mg/L)			C/C_0
	1	2	Average	1	2	Average	1	2	Average	
0	7725	7708	7717	3.20	3.19	3.20	100.55	100.33	100.44	1.00
15	5170	5117	5144	2.14	2.44	2.29	67.28	76.49	71.89	0.72
30	4211	4113	4162	1.49	1.66	1.57	46.77	52.08	49.43	0.49
45	3014	2963	2989	0.97	1.05	1.01	30.47	32.92	31.69	0.32
60	2071	2047	2059	0.80	0.53	0.66	25.07	16.59	20.83	0.21
90	1209	1068	1139	0.35	0.23	0.29	11.03	7.07	9.05	0.09
120	135	127	131	0.11	0.11	0.11	3.46	3.52	3.49	0.03
ADMI eff (%)	98.25	98.10	98.30							

Table A6 Treatment of IC dye in synthetic wastewater by the photocatalytic process at an initial concentration of 100 ppm of Experiment condition 6.

Time (min)	(ADMI)			(Abs)			Conc. (mg/L)			C/C_0
	1	2	Average	1	2	Average	1	2	Average	
0	7725	7708	7717	3.20	3.19	3.20	100.55	100.33	100.44	1.00
15	6248	6436	6342	2.59	2.67	2.63	81.33	83.78	82.55	0.82
30	5471	5746	5609	2.27	2.38	2.32	71.21	74.79	73.00	0.73
45	4445	4187	4316	1.84	1.74	1.79	57.86	54.50	56.18	0.56
60	3036	2835	2936	1.26	1.18	1.22	39.52	36.91	38.21	0.38
90	1827	1986	1907	0.76	0.82	0.79	23.78	25.85	24.82	0.25
120	1414	1528	1471	0.59	0.63	0.61	18.41	19.88	19.15	0.19
ADMI eff (%)	81.86	80.20	80.94							

Table A7 Treatment of IC dye in synthetic wastewater by the photocatalytic process at an initial concentration of 100 ppm of Experiment condition 7.

Time (min)	(ADMI)			(Abs)			Conc. (mg/L)			C/C_0
	1	2	Average	1	2	Average	1	2	Average	
0	7725	7708	7717	3.20	3.19	3.20	100.55	100.33	100.44	1.00
15	6532	6469	6501	2.71	2.69	2.70	85.03	84.56	84.80	0.84
30	5936	6072	6004	2.46	2.52	2.49	77.27	79.03	78.15	0.78
45	4993	5292	5143	2.07	2.19	2.13	64.99	68.89	66.94	0.67
60	3895	4414	4155	1.61	1.83	1.72	50.70	57.45	54.08	0.54
90	3214	3596	3405	1.33	1.49	1.41	41.84	46.80	44.32	0.44
120	2430	3053	2742	1.01	1.27	1.14	31.63	39.74	35.68	0.36
ADMI eff (%)	68.51	60.44	64.47							

Table A8 Treatment of IC dye in synthetic wastewater by the photocatalytic process at an initial concentration of 100 ppm of Experiment condition 8.

Time (min)	(ADMI)			(Abs)			Conc. (mg/L)			C/C_0
	1	2	Average	1	2	Average	1	2	Average	
0	7724	7708	7716	3.20	3.19	3.20	100.55	100.33	100.44	1.00
15	6600	6692	6646	2.74	2.77	2.75	85.91	87.11	86.51	0.86
30	5931	6228	6080	2.46	2.58	2.52	77.21	81.07	79.14	0.79
45	5277	5381	5329	2.19	2.23	2.21	68.70	70.05	69.37	0.69
60	4654	4756	4705	1.93	1.97	1.95	60.59	61.91	61.25	0.61
90	3774	3974	3874	1.56	1.65	1.61	49.13	51.74	50.43	0.50
120	3094	3171	3123	1.27	1.31	1.29	40.02	41.28	40.65	0.40
ADMI eff (%)	59.90	58.90	59.53							

Table A9 Treatment of IC dye in synthetic wastewater by the photocatalytic process at an initial concentration of 100 ppm of Experiment condition 9.

Time (min)	(ADMI)			(Abs)			Conc. (mg/L)			C/C_0
	1	2	Average	1	2	Average	1	2	Average	
0	7766	7831	7799	3.21	3.25	3.23	100.96	102.07	100.96	1.00
15	7766	7831	7799	3.17	3.25	3.21	99.68	102.07	99.68	0.99
30	7766	7831	7799	3.17	3.25	3.21	99.68	102.07	99.68	0.99
45	7766	7831	7799	3.17	3.25	3.21	99.68	102.07	99.68	0.99
60	7766	7831	7799	3.17	3.25	3.21	99.68	102.07	99.68	0.99
90	7766	7831	7799	3.17	3.25	3.21	99.68	102.07	99.68	0.99
120	7766	7831	7799	3.17	3.25	3.21	99.68	102.07	99.68	0.99
ADMI eff (%)	-	-	-							

Table A10 Treatment of IC dye in synthetic wastewater by the photocatalytic process at an initial concentration of 100 ppm of Experiment condition 10.

Time (min)	(ADMI)			(Abs)			Conc. (mg/L)			C/C_0
	1	2	Average	1	2	Average	1	2	Average	
0	7725	7718	7722	3.20	3.19	3.20	100.68	100.46	100.68	1.00
15	7725	7718	7722	3.16	3.19	3.18	99.49	100.37	99.49	0.99
30	7725	7718	7722	3.16	3.19	3.18	99.49	100.37	99.49	0.99
45	7725	7718	7722	3.16	3.19	3.18	99.49	100.37	99.49	0.99
60	7725	7718	7722	3.16	3.19	3.18	99.49	100.37	99.49	0.99
90	7725	7718	7722	3.16	3.19	3.18	99.49	100.37	99.49	0.99
120	7725	7718	7722	3.16	3.19	3.18	99.49	100.37	99.49	0.99
ADMI eff (%)	-	-	-							

Table A11 Treatment of RB5 dye in synthetic wastewater by the photocatalytic process at an initial concentration of 100 ppm of Experiment condition 1.

Time (min)	(ADMI)			(Abs)			Conc. (mg/L)			C/C_0
	1	2	Average	1	2	Average	1	2	Average	
0	7882	8083	7983	3.26	3.34	3.30	99.91	102.46	101.18	1.00
15	3053	3508	3281	1.26	1.45	1.36	38.70	44.47	41.58	0.41
30	1454	1911	1683	0.60	0.79	0.70	18.43	24.23	21.33	0.21
45	600	929	765	0.25	0.38	0.32	7.61	11.78	9.69	0.10
60	351	421	386	0.15	0.17	0.16	4.45	5.34	4.89	0.05
90	109	160	135	0.05	0.07	0.06	1.38	2.02	1.70	0.02
120	92	111	102	0.04	0.05	0.04	1.17	1.41	1.29	0.01
ADMI eff (%)	98.85	98.61	98.73							

Table A12 Treatment of RB5 dye in synthetic wastewater by the photocatalytic process at an initial concentration of 100 ppm of Experiment condition 2.

Time (min)	(ADMI)			(Abs)			Conc. (mg/L)			C/C_0
	1	2	Average	1	2	Average	1	2	Average	
0	7882	8083	7983	3.26	3.34	3.30	99.91	102.46	101.18	1.00
15	7178	6854	7016	2.97	2.83	2.90	90.99	86.88	88.93	0.88
30	6073	5456	5765	2.51	2.26	2.38	76.97	69.15	73.06	0.72
45	4984	4478	4731	2.06	1.85	1.96	63.17	56.76	59.97	0.59
60	3767	3358	3563	1.56	1.39	1.47	47.75	42.56	45.16	0.45
90	2845	2279	2562	1.18	0.94	1.06	36.06	28.89	32.48	0.32
120	2260	1967	1814	0.93	0.57	0.75	28.64	17.33	22.98	0.23
ADMI eff (%)	71.69	75.36	77.28							

Table A13 Treatment of RB5 dye in synthetic wastewater by the photocatalytic process at an initial concentration of 100 ppm of Experiment condition 3.

Time (min)	(ADMI)			(Abs)			Conc. (mg/L)			C/C_0
	1	2	Average	1	2	Average	1	2	Average	
0	7882	8083	7983	3.26	3.34	3.30	99.91	102.46	101.18	1.00
15	7556	7447	7502	3.12	3.08	3.10	95.77	94.39	95.08	0.94
30	7442	7307	7375	3.08	3.02	3.05	94.33	92.61	93.47	0.92
45	7323	7065	7194	2.99	2.92	2.95	91.66	89.54	90.60	0.90
60	6259	6910	6585	2.59	2.86	2.72	79.33	87.58	83.46	0.82
90	5211	6503	5857	2.15	2.69	2.42	66.05	82.43	74.24	0.73
120	4106	5463	4785	1.70	2.26	1.98	52.04	69.24	60.64	0.60
ADMI eff (%)	48.56	31.56	40.06							

Table A14 Treatment of RB5 dye in synthetic wastewater by the photocatalytic process at an initial concentration of 100 ppm of Experiment condition 4.

Time (min)	(ADMI)			(Abs)			Conc. (mg/L)			C/C_0
	1	2	Average	1	2	Average	1	2	Average	
0	7882	8083	7983	3.26	3.34	3.30	99.91	102.46	101.18	1.00
15	7002	7004	7003	2.89	2.90	2.89	88.75	88.78	88.76	0.88
30	6552	6235	6394	2.71	2.58	2.64	83.04	79.03	81.03	0.80
45	6254	5947	6101	2.59	2.46	2.52	79.27	75.38	77.32	0.76
60	5690	5442	5566	2.35	2.25	2.30	72.13	69.00	70.56	0.70
90	3886	3951	3919	1.61	1.63	1.62	49.25	50.08	49.66	0.49
120	2809	2637	2723	1.16	1.09	1.13	35.60	33.43	34.51	0.34
ADMI eff (%)	64.81	66.97	65.89							

Table A15 Treatment of RB5 dye in synthetic wastewater by the photocatalytic process at an initial concentration of 100 ppm of Experiment condition 5.

Time (min)	(ADMI)			(Abs)			Conc. (mg/L)			C/C_0
	1	2	Average	1	2	Average	1	2	Average	
0	7904	7957	7931	3.27	3.29	3.28	100.19	100.86	100.52	1.00
15	6278	6073	6176	2.29	2.35	2.32	70.16	72.07	71.11	0.71
30	5419	5103	5261	1.35	1.95	1.65	41.52	59.92	50.72	0.50
45	4232	3961	4097	1.11	1.10	1.11	34.16	33.67	33.92	0.34
60	3624	3000	3312	0.72	0.79	0.75	21.93	24.07	23.00	0.23
90	2037	1558	1798	0.25	0.44	0.34	7.51	13.34	10.43	0.10
120	150	194	172	0.16	0.14	0.15	4.97	4.26	4.62	0.05
ADMI eff (%)	98.11	97.55	97.83							

Table A16 Treatment of RB5 dye in synthetic wastewater by the photocatalytic process at an initial concentration of 100 ppm of Experiment condition 6.

Time (min)	(ADMI)			(Abs)			Conc. (mg/L)			C/C_0
	1	2	Average	1	2	Average	1	2	Average	
0	7904	7957	7931	3.27	3.29	3.28	100.19	100.86	100.52	1.00
15	7304	7198	7251	3.02	2.98	3.00	92.58	91.23	91.91	0.91
30	6379	6288	6334	2.64	2.60	2.62	80.87	79.70	80.28	0.80
45	4908	4827	4868	2.03	2.00	2.01	62.22	61.18	61.70	0.61
60	4083	3494	3789	1.69	1.44	1.57	51.76	44.28	48.02	0.48
90	2441	2064	2253	1.01	0.85	0.93	30.94	26.16	28.55	0.28
120	1923	1357	1640	0.80	0.56	0.68	24.38	17.20	20.79	0.21
ADMI eff (%)	75.75	82.89	79.32							

Table A17 Treatment of RB5 dye in synthetic wastewater by the photocatalytic process at an initial concentration of 100 ppm of Experiment condition 7.

Time (min)	(ADMI)			(Abs)			Conc. (mg/L)			C/C_0
	1	2	Average	1	2	Average	1	2	Average	
0	7904	7957	7931	3.27	3.29	3.28	100.19	100.86	100.52	1.00
15	7691	7676	7684	3.18	3.17	3.18	97.49	97.30	97.40	0.97
30	7550	7509	7530	3.12	3.10	3.11	95.71	95.19	95.45	0.95
45	7536	7371	7454	3.12	3.05	3.08	95.52	93.44	94.48	0.94
60	7113	7052	7083	2.94	2.92	2.93	90.16	89.39	89.77	0.89
90	6242	6883	6563	2.58	2.85	2.71	79.12	87.24	83.18	0.83
120	5625	6496	6061	2.33	2.69	2.51	71.30	82.34	76.82	0.76
ADMI eff (%)	29.07	18.09	23.58							

Table A18 Treatment of RB5 dye in synthetic wastewater by the photocatalytic process at an initial concentration of 100 ppm of Experiment condition 8.

Time (min)	(ADMI)			(Abs)			Conc. (mg/L)			C/C_0
	1	2	Average	1	2	Average	1	2	Average	
0	7904	7957	7931	3.27	3.29	3.28	100.19	100.86	100.52	1.00
15	7388	7265	7327	3.05	3.00	3.03	93.65	92.09	92.87	0.92
30	6909	6793	6851	2.86	2.81	2.83	87.58	86.11	86.85	0.86
45	6532	6503	6518	2.70	2.69	2.69	82.80	82.43	82.61	0.82
60	5673	5593	5633	2.35	2.31	2.33	71.91	70.90	71.41	0.71
90	5124	5046	5085	2.12	2.09	2.10	64.95	63.97	64.46	0.64
120	4800	4077	4439	1.98	1.69	1.83	60.84	51.67	56.26	0.56
ADMI eff (%)	39.47	48.59	44.03							

Table A19 Treatment of RB5 dye in synthetic wastewater by the photocatalytic process at an initial concentration of 100 ppm of Experiment condition 9.

Time (min)	(ADMI)			(Abs)			Conc. (mg/L)			C/C_0
	1	2	Average	1	2	Average	1	2	Average	
0	7882	8083	7983	3.26	3.34	3.30	99.91	102.46	99.91	1.00
15	7865	8083	7974	3.25	3.34	3.30	99.70	102.46	99.70	1.00
30	7865	8083	7974	3.25	3.34	3.30	99.70	102.46	99.70	1.00
45	7865	8083	7974	3.25	3.34	3.30	99.70	102.46	99.70	1.00
60	7865	8083	7974	3.25	3.34	3.30	99.70	102.46	99.70	1.00
90	7865	8083	7974	3.25	3.34	3.30	99.70	102.46	99.70	1.00
120	7865	8083	7974	3.25	3.34	3.30	99.70	102.46	99.70	1.00
ADMI eff (%)	-	-	-							

Table A20 Treatment of RB5 dye in synthetic wastewater by the photocatalytic process at an initial concentration of 100 ppm of Experiment condition 10.

Time (min)	(ADMI)			(Abs)			Conc. (mg/L)			C/C_0
	1	2	Average	1	2	Average	1	2	Average	
0	7407	7957	7682.00	3.39	3.29	3.34	103.80	100.86	103.80	1.00
15	7400	7957	7678.50	3.31	3.29	3.30	101.35	100.86	101.35	0.99
30	7398	7957	7677.50	3.26	3.29	3.27	99.91	100.86	99.91	0.98
45	7396	7957	7676.50	3.26	3.29	3.27	99.91	100.86	99.91	0.98
60	7393	7957	7675.00	3.26	3.29	3.27	99.91	100.86	99.91	0.98
90	7391	7957	7674.00	3.26	3.29	3.27	99.91	100.86	99.91	0.98
120	7391	7957	7674.00	3.26	3.29	3.27	99.91	100.86	99.91	0.98
ADMI eff (%)	-	-	-							

Table A21 Treatment of carbaryl pesticides in synthetic wastewater by the photocatalytic process at an initial concentration of 10 ppm of Experiment condition 1.

Time (min)	(Abs)			Conc. (mg/L)			C/C_0	Removal %
	1	2	Average	1	2	Average		
0	2.93	2.95	2.94	9.51	9.55	9.51	1.00	
15	1.43	1.57	1.50	4.62	5.08	4.62	0.51	
30	0.79	0.68	0.73	2.55	2.20	2.55	0.25	
45	0.41	0.35	0.38	1.34	1.12	1.34	0.13	
60	0.22	0.12	0.17	0.70	0.38	0.70	0.06	
90	0.06	0.05	0.06	0.19	0.17	0.19	0.02	
120	0.01	0.01	0.01	0.11	0.07	0.11	0.01	

Table A22 Treatment of carbaryl pesticides in synthetic wastewater by the photocatalytic process at an initial concentration of 10 ppm of Experiment condition 2.

Time (min)	(Abs)			Conc. (mg/L)			C/C_0	Removal %
	1	2	Average	1	2	Average		
0	2.93	2.95	2.94	9.51	9.55	9.51	1.00	0.00
15	2.70	1.98	2.34	8.75	6.43	8.75	0.80	20.36
30	1.83	1.56	1.70	5.92	5.07	5.92	0.58	42.30
45	1.36	1.09	1.22	4.40	3.52	4.40	0.42	58.45
60	0.95	0.86	0.90	3.07	2.79	3.07	0.31	69.24
90	0.62	0.42	0.52	2.01	1.37	2.01	0.18	82.30
120	0.28	0.13	0.20	0.91	0.41	0.91	0.07	93.06

Table A23 Treatment of carbaryl pesticides in synthetic wastewater by the photocatalytic process at an initial concentration of 10 ppm of Experiment condition 3.

Time (min)	(Abs)			Conc. (mg/L)			C/C_0	Removal %
	1	2	Average	1	2	Average		
0	2.93	2.95	2.94	9.51	9.55	9.53	1.00	0.00
15	2.62	2.51	2.56	8.48	8.15	8.32	0.87	12.71
30	2.48	2.19	2.34	8.04	7.11	7.58	0.80	20.49
45	2.15	1.86	2.00	6.97	6.04	6.50	0.68	31.76
60	1.88	1.59	1.73	6.09	5.16	5.62	0.59	40.99
90	1.25	0.97	1.11	4.07	3.14	3.61	0.38	62.16
120	0.78	0.50	0.64	2.54	1.62	2.08	0.22	78.20

Table A24 Treatment of carbaryl pesticides in synthetic wastewater by the photocatalytic process at an initial concentration of 10 ppm of Experiment condition 4.

Time (min)	(Abs)			Conc. (mg/L)			C/C_0	Removal %
	1	2	Average	1	2	Average		
0	2.93	2.95	2.94	9.51	9.55	9.53	1.00	0.00
15	2.48	2.58	2.53	8.05	8.38	8.21	0.86	13.80
30	1.99	2.29	2.14	6.45	7.42	6.93	0.73	27.25
45	1.74	1.74	1.74	5.64	5.64	5.64	0.59	40.80
60	1.43	1.43	1.43	4.65	4.65	4.65	0.49	51.25
90	0.91	0.81	0.86	2.97	2.64	2.80	0.29	70.59
120	0.54	0.54	0.54	1.76	1.76	1.76	0.18	81.58

Table A25 Treatment of carbaryl pesticides in synthetic wastewater by the photocatalytic process at an initial concentration of 10 ppm of Experiment condition 5.

Time (min)	(Abs)			Conc. (mg/L)			C/C_0	Removal %
	1	2	Average	1	2	Average		
0	3.20	3.01	3.10	10.37	9.77	10.07	1.00	3.20
15	1.84	1.70	1.77	5.95	5.50	5.73	0.57	1.84
30	1.17	1.12	1.15	3.79	3.64	3.71	0.37	1.17
45	0.70	0.72	0.71	2.28	2.33	2.31	0.23	0.70
60	0.41	0.47	0.44	1.34	1.52	1.43	0.14	0.41
90	0.14	0.23	0.19	0.45	0.76	0.60	0.06	0.14
120	0.02	0.13	0.08	0.07	0.43	0.25	0.03	0.02

Table A26 Treatment of carbaryl pesticides in synthetic wastewater by the photocatalytic process at an initial concentration of 10 ppm of Experiment condition 6.

Time (min)	(Abs)			Conc. (mg/L)			C/C_0	Removal %
	1	2	Average	1	2	Average		
0	3.20	3.01	3.10	10.37	9.77	10.07	1.00	0.00
15	2.32	2.30	2.31	7.52	7.45	7.49	0.74	25.66
30	2.15	1.99	2.07	6.99	6.45	6.72	0.67	33.32
45	1.96	1.72	1.84	6.36	5.56	5.96	0.59	40.83
60	1.78	1.70	1.74	5.78	5.50	5.64	0.56	44.02
90	1.55	1.47	1.51	5.03	4.78	4.91	0.49	51.30
120	1.18	0.95	1.06	3.83	3.08	3.45	0.34	65.71

Table A27 Treatment of carbaryl pesticides in synthetic wastewater by the photocatalytic process at an initial concentration of 10 ppm of Experiment condition 7.

Time (min)	(Abs)			Conc. (mg/L)			C/C_0	Removal %
	1	2	Average	1	2	Average		
0	3.197	3.012	3.105	10.37	9.77	10.07	1.000	0.00
15	2.622	2.373	2.498	8.51	7.70	8.10	0.804	19.55
30	2.537	2.300	2.419	8.23	7.46	7.85	0.779	22.10
45	2.42	2.199	2.310	7.85	7.13	7.49	0.744	25.61
60	2.26	2.061	2.161	7.33	6.69	7.01	0.696	30.41
90	1.97	1.811	1.891	6.39	5.88	6.13	0.609	39.10
120	1.615	1.505	1.560	5.24	4.88	5.06	0.502	49.75

Table A28 Treatment of carbaryl pesticides in synthetic wastewater by the photocatalytic process at an initial concentration of 10 ppm of Experiment condition 8.

Time (min)	(Abs)			Conc. (mg/L)			C/C_0	Removal %
	1	2	Average	1	2	Average		
0	3.20	3.01	3.10	10.37	9.77	10.07	1.00	0.00
15	2.33	2.26	2.29	7.56	7.33	7.44	0.74	26.11
30	1.58	1.61	1.59	5.12	5.23	5.17	0.51	48.66
45	1.24	1.32	1.28	4.01	4.27	4.14	0.41	58.91
60	1.09	1.19	1.14	3.53	3.86	3.69	0.37	63.33
90	0.94	0.91	0.92	3.03	2.96	2.99	0.30	70.27
120	0.74	0.82	0.78	2.39	2.66	2.52	0.25	74.94

Table A29 Treatment of carbaryl pesticides in synthetic wastewater by the photocatalytic process at an initial concentration of 10 ppm of Experiment condition 9.

Time (min)	(Abs)			Conc. (mg/L)			C/C_0	Removal %
	1	2	Average	1	2	Average		
0	2.93	2.95	2.94	9.51	9.55	9.51	1.00	0.00
15	2.92	2.95	2.93	9.48	9.55	9.48	1.00	0.12
30	2.92	2.95	2.93	9.48	9.55	9.48	1.00	0.12
45	2.92	2.95	2.93	9.48	9.55	9.48	1.00	0.12
60	2.92	2.95	2.93	9.48	9.55	9.48	1.00	0.12
90	2.92	2.95	2.93	9.48	9.55	9.48	1.00	0.12
120	2.92	2.95	2.93	9.48	9.55	9.48	1.00	0.12

Table A30 Treatment of carbaryl pesticides in synthetic wastewater by the photocatalytic process at an initial concentration of 10 ppm of Experiment condition 10.

Time (min)	(Abs)			Conc. (mg/L)			C/C_0	Removal %
	1	2	Average	1	2	Average		
0	3.20	3.01	3.10	10.37	9.77	10.07	1.00	0.00
15	2.98	2.91	2.93	9.68	9.42	9.55	0.95	0.10
30	2.98	2.91	2.93	9.68	9.42	9.55	0.95	0.10
45	2.98	2.91	2.93	9.68	9.42	9.55	0.95	0.10
60	2.98	2.91	2.93	9.68	9.42	9.55	0.95	0.10
90	2.98	2.91	2.93	9.68	9.42	9.55	0.95	0.10
120	2.98	2.91	2.93	9.68	9.42	9.55	0.95	0.10

APPENDIX B

Dye degradations through experimental

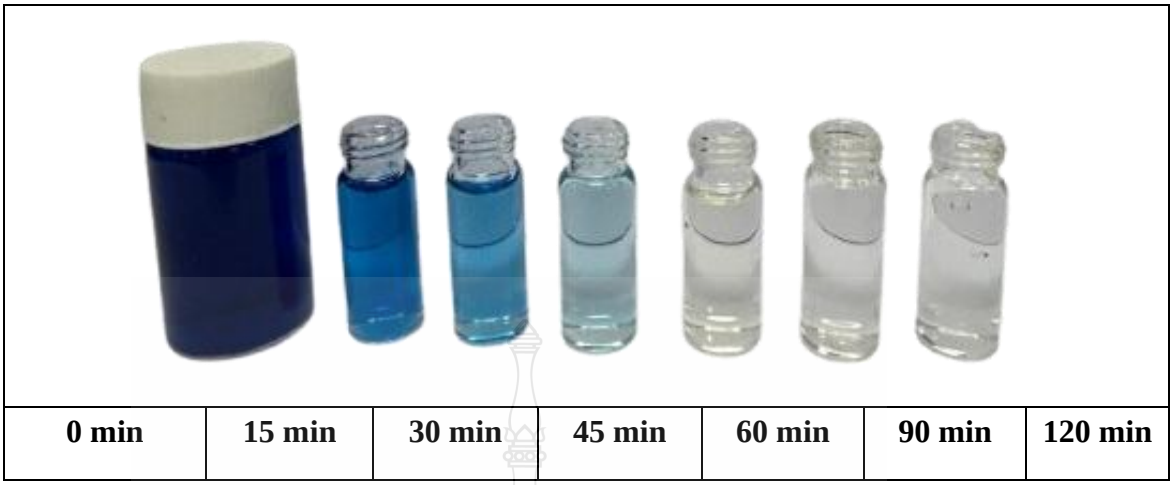

0 min	15 min	30 min	45 min	60 min	90 min	120 min

Figure B1 Experimental condition 1 Treatment with IC dye at a concentration of 100 ppm for 120 minutes.

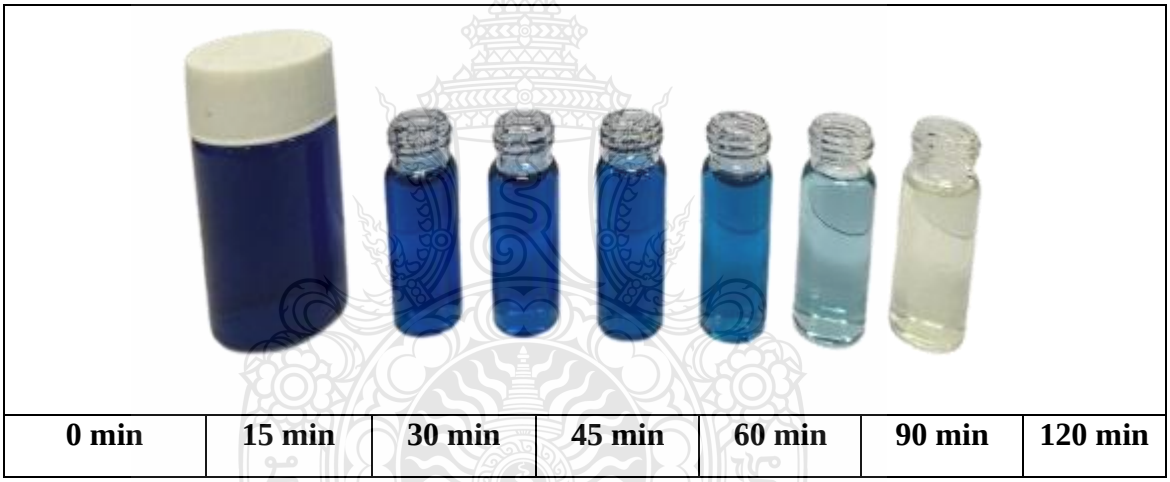

0 min	15 min	30 min	45 min	60 min	90 min	120 min

Figure B2 Experimental condition 2 Treatment with IC dye at a concentration of 100 ppm for 120 minutes.

0 min	15 min	30 min	45 min	60 min	90 min	120 min

Figure B3 Experimental condition 3 Treatment with IC dye at a concentration of 100 ppm for 120 minutes.

0 min	15 min	30 min	45 min	60 min	90 min	120 min

Figure B4 Experimental condition 4 Treatment with IC dye at a concentration of 100 ppm for 120 minutes.

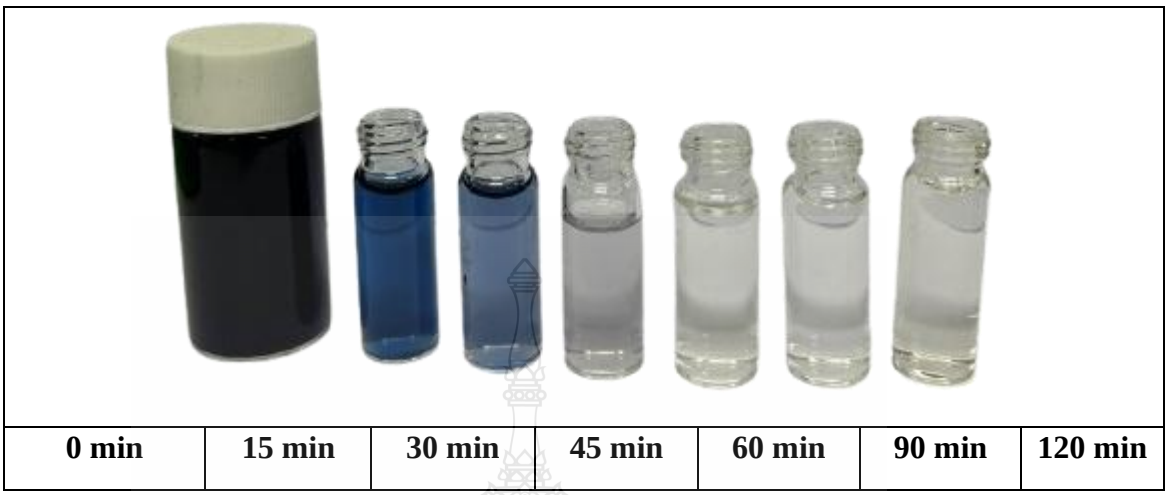

0 min	15 min	30 min	45 min	60 min	90 min	120 min

Figure B5 Experimental condition 1 Treatment with RB5 dye at a concentration of 100 ppm for 120 minutes.

0 min	15 min	30 min	45 min	60 min	90 min	120 min

Figure B6 Experimental condition 2 Treatment with RB5 dye at a concentration of 100 ppm for 120 minutes.

0 min	15 min	30 min	45 min	60 min	90 min	120 min

Figure B7 Experimental condition 3 Treatment with RB5 dye at a concentration of 100 ppm for 120 minutes.

0 min	15 min	30 min	45 min	60 min	90 min	120 min

Figure B8 Experimental condition 4 Treatment with RB5 dye at a concentration of 100 ppm for 120 minutes.

APPENDIX C

Equipment and tools used in the experimental

Figure C1 Elma Elmasonic E30H 2.75 Liter Heated Ultrasonic Cleaner

Figure C2 Hydrothermal Synthesis Autoclave Reactor Model w/PTFE Lined 250 mL

Figure C3 UV-Spectrophotometer Single Monochrome Type U-3900

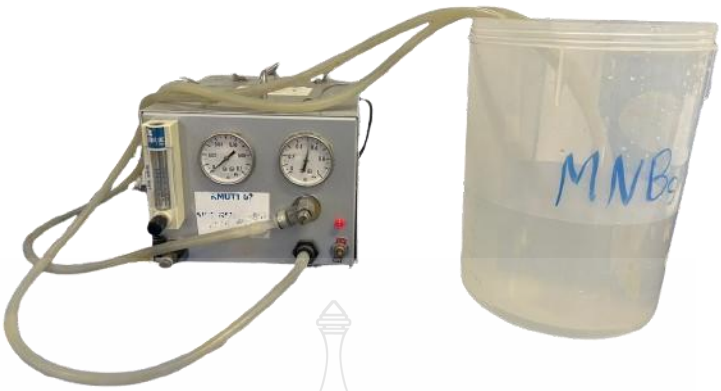

Figure C4 Micro-nano bubble aerator Model RMUTT-MNB

Figure C5 Color measurement device MERCK Prove 100 ADMI spectrometer

Biography

Name-Surname	Phoutthideth Phouheuanghong
Date of Birth	22 September 2000
Address	025, Tha-duea Road, Vatnak Village, Sisattanark District, Vientiane Captain, Lao PDR
Education	Bachelor's degree with Honours (First Class), Department of Environmental Planning and Development, Faculty of Environmental Sciences. National University of Laos PDR
Experiences Work	.....
Telephone Number	+66-098-22834214, +856 20 99191159
Email Address	leephoudthideth19@gmail.com